FIBER OPTIC SENSORS FOR ENERGY APPLICATIONS UNDER HARSH ENVIRONMENTAL CONDITIONS

by

Aidong Yan

B. S., Nankai University, 2008

M. S., Nankai University, 2011

Submitted to the Graduate Faculty of

The Swanson School of Engineering in partial fulfillment

of the requirements for the degree of

Doctor of Philosophy

University of Pittsburgh

2017

UNIVERSITY OF PITTSBURGH

SWANSON SCHOOL OF ENGINEERING

This dissertation was presented

by

Aidong Yan

It was defended on

October 6, 2017

and approved by

Kevin P. Chen, Ph. D., Professor, Department of Electrical and Computer Engineering

William Stanchina, Ph. D., Professor, Department of Electrical and Computer Engineering

Guanyong Li, Ph. D., Associate Professor, Department of Electrical and Computer Engineering

Zhi-Hong Mao, Ph. D., Associate Professor, Department of Electrical and Computer Engineering

Paul Ohodnicki, Ph. D., Material Scientist, National Energy Technology Laboratory

Dissertation Director: Kevin P. Chen, Ph. D., Professor, Department of Electrical and Computer Engineering

FIBER OPTIC SENSORS FOR ENERGY APPLICATIONS UNDER HARSH ENVIRONMENTAL CONDITIONS

Aidong Yan, PhD

University of Pittsburgh, 2017

Real-time monitoring physical and chemical parameters in next generation energy-production system is of significant importance to improve the efficiency and reduce the emission for a wide range of applications. Traditional electrical point sensors have limited utilities for direct measurements at high temperature or in highly reactive and corrosive environment. Given the resilience at high temperatures, immunity to electromagnetic interference and intrinsic explosion proof in combustion gas, fiber optic sensors open up opportunity to perform various measurements in energy applications under harsh environments.

In this thesis, both chemical and physical sensors were demonstrated to explore the potential of fiber optic sensors in energy industry. The first scheme is fiber optic chemical gas sensing enabled by nanostructured functional metal oxides. A scalable manufacturing approach was developed to produce nano-porous metal oxides with the refractive index tailored to match the optical fiber material. Combined with this functional semiconducting metal oxides, fiber optic chemical sensors with high selectivity and sensitivity was developed using both D-shaped fiber and single crystal sapphire fiber. The sensors performed accurate hydrogen measurement at a record-high temperature of 800^{o}C. The second scheme covers a high temperature distributed sensing using Rayleigh backscatter based optical frequency domain reflectometry. Ultrafast laser direct writing method was used to enhance the in-fiber scattering signal and high-temperature stability. Due to the high signal-to-noise ratio and thermal stability of the inscribed nanogratings

in the fiber, real-time monitoring of temperature distribution in the operational solid oxide fuel cell was achieved with 5-mm spatial resolution at 800^{o}C. In the third scheme, a multi-point sensing system for thermal dynamics monitoring of lithium-ion battery assembly was demonstrated using multimode random air hole fibers infiltrated with quantum dots. The photoluminescence intensity dependence on the ambient temperatures were used to gauge the local operational temperature of lithium-ion batteries. Multi-point temperature sensing systems were developed by bundling quantum dots infiltrated random air hole fibers together. The temperature of the batteries can be real-time monitored using a low-cost UV diode laser as light source and a cellular phone CCD camera as detector.

TABLE OF CONTENTS

LIST OF TABLES

LIST OF FIGURES

PREFACE

First and foremost, I would like to express my sincere thanks and gratitude to my advisor Dr. Kevin P. Chen for his guidance and support during my entire work. He has always been there to give me insightful advice and point me in the right directions for my research. I also thank him for maintaining a very friendly and open lab community.

I would like to thank our collaborators from National Energy Technology Laboratory, Dr. Paul Ohodnicki and Dr. Michael Buric, for their support and suggestions in all my projects.

Many thanks to Dr. William Stanchina, Dr. Guangyong Li, Dr. Zhi-Hong Mao of our department and Dr. Paul Ohodnicki for agreeing to join my program committee.

I would also acknowledge my colleagues in our group, Dr. Rongzhang Chen, Dr. Qingqing Wang, Sheng Huang, Shuo Li, Mohamed Zaghloul, Ran Zou, Mohan Wang, Zhaoqiang Peng and Rongtao Cao, for the great help and inspiring discussions in our collaborations.

Last, and most significantly, I want to sincerely thank my family. My studies could not have been possible without the love, care, understanding, support and encouragement from them.

1.0 INTRODUCTION

Development of fast, reliable, and sensitive physical and chemical sensors which can operate under harsh environments is an increasingly important research for a wide range of applications in the energy, automobile, and aerospace industries. There have been developed many electronic sensors that could meet the needs under normal operation conditions. However, most of the electronic sensors are highly susceptible in these applications when associated with harsh environments such as high temperature, corrosive chemicals, explosive materials, or strong electromagnetic interference. They are also uneconomical when a large number of sensor units are required for distributed measurement.

On the other hand, fiber optic sensors present advantages to all of these issues comparing to the traditional electronic sensors. The optical fibers made of silica glass are resilient in high temperature environments and inert to many chemicals materials. They also don't need insulation package when working in conductive environments. The working principles of the optic fiber sensors is detecting the change of the light properties including intensity, wavelength, phase or polarization. So, they are also immune to electromagnetic interference. More importantly, silica-based fibers, which has low transmission loss, low cost and miniature size, allows feasible distributed and multi-parameter measurements, leading to more information than point sensors.

Fiber optical sensors have been developed to perform various physical measurements such as temperature, strain, and pressures sensing for energy applications. At the same time, a lot of optical fiber chemical sensor have been also under development to perform high-temperature chemical sensing for their excellent high-temperature stabilities. Considering the measurement of chemical spices and the inert natures of silica or sapphire materials, incorporating sensory materials with optical fiber is a practical way to extend functionalities of optical fibers for detections of chemical species at high temperatures. One of the most widely used groups of gas sensors material is semiconducting metal oxides with specific dopants or nanostructures, of which conductivity can be selectively influenced by surface adsorption of chemical species [1-3]. Most of the semiconducting metal oxides chemical gas sensors are electrical sensors based on resistance measurement, their usability at high-temperature harsh environments are limited up to 400^{o}C due to their heterogeneous device structures consisting of different materials. Further they may not be safe to be used at high temperature in explosive gas atmosphere such as hydrogen and methane. However, optical properties of the metal oxides may also change under the detection gas atmosphere. The optical properties rely on the electrical conductance as well as the localized surface effects and electronic transitions between bound states of the electronic structure [4, 5]. By integrating fiber with functional metal oxides, all optical fiber gas sensors such as Bragg grating [6], surface plasmon resonance sensor [7] and evanescent sensor [8] are investigated in the past years.

However, the typical refractive indices of metal oxides ($n>2.2$) are significantly higher than that of commercial silica fiber cores ($n\sim1.46$) or sapphire fibers ($n\sim1.73$), so most demonstrated metal oxide integrated optical fiber sensors have been limited to the thin film regime (on the order of 100nm) [9, 10] to avoid guided wave coupling and loss in high-index

metal oxide film. These thin coatings do not take full advantage of the interacting evanescent fields. In chapter 3, we developed a scalable nanotechnology method to engineer refractive indices of a wide array functional transition-metal oxide materials and their dopant variants such as TiO_2, ZnO, SnO_2, in the range of 1.25 to 2.2. By integration of these nanostructured metal oxides with controlled refractive index, the sensitivity of fiber optic sensors can be improved due to the increase of interaction length between the metal-oxide coatings and the guided light. D-shaped fiber chemical gas sensors based on functional metal oxide sensory materials with proper refractive indices and chemical sensitivities are demonstrated. Both fiber Bragg gratings and direct transmission loss measurement were used in this work, gas sensing tests for fuel gases including hydrogen and methane was studied from 400^{o}C -750^{o}C.

Another interesting advantage of optic fiber sensors is its capability of distributed measurement by using various schemes such as OFDR based on Rayleigh scattering. Combined with Rayleigh OFDR technique, distributed measurement of the gas was also demonstrated on D-shaped fiber. However, the detection distance and spatial resolution was compromised due to the weak intrinsic Rayleigh scattering signal of the standard fiber. The fiber with enhanced scattering signal can benefit the chemical gas sensing due to larger dynamic range and resulting longer detection length. In order to further enhance the capability of the distributed fiber optic chemical gas sensor that can provide long-term stability and better sensitivity for fuel gas concentration gradient measurement. The distributed chemical gas sensor combined both nanostructured metal oxide with controlled refractive index and fiber with enhanced scattering signal was also present in chapter 3. Preliminary results show that, the enhancement of the scattering will be improved in ambient hydrogen at high temperature. The distributed scattering signal of hydrogen gas sensing is much smoother than that without scattering enhancement, which will give better spatial resolution of chemical gas sensing.

To further expand the operation temperature of the fiber optic hydrogen sensors, a single-crystal sapphire fiber was used as the sensor platform in chapter 4. The sapphire fiber has a very high melting point (above 2000^{o}C) and superior resistance to corrosive chemicals, which made itself a good candidate for high temperature applications. By coating the fiber with hydrogen-sensitive Pd nanoparticles incorporated TiO_2 nano-porous thin film, the sensor can perform accurate hydrogen measurements with high sensitivity at a record-high temperature of 800^{o}C. The sensitivity of the sensor was evaluated by monitoring both intensity and time response at different temperature from 600^{o}C to 800^{o}C.

High temperature solid oxide fuel cells (SOFC) offer a promising and versatile energy generation scheme, which are widely used in many applications ranging from clean automobiles to power generation systems. The interconnect of the SOFC is continuously exposed to reforming or oxidation reactions at high temperatures. In order to improve the long-term stability of the SOFCs, the capability to measure and engineer the thermal distribution inside the fuel cell assembly is highly desirable. Distributed sensing schemes based on Rayleigh-scattering OFDR provides a potentially powerful technique to probe the temperature distribution of an operating SOFC system. However, the intrinsic low scattering signal of the silica glass limits the measurement of the temperature range and sensitivity. A reliable distributed sensing for high temperature operation based on enhanced Rayleigh scattering in fiber is presented in chapter 5. By directly ultrafast laser irradiation in the core of fiber, the in-fiber Rayleigh scattering signal was improved by 40~45 dB due to the formation of nanograting. The morphology of the nanograting was studied at different laser scanning speed. Optimum irradiation conditions were used to process the fiber with lower insertion loss. Study of the thermal stability of the inscribed nanogratings shows decrease slightly in the polarization at high temperature and the

enhancement of the scattering is rendered truly thermal stable by annealing. Temperature measurement was performed from room temperature to 800^{o}C with good repeatability. Field test in SOFC was demonstrated using the optical fiber with enhanced Rayleigh scattering profiles. The gathered information can be used to improve the operational efficiency and longevity of SOFC-based energy generation systems.

The lithium-ion battery is one of the most used power supplies in electric vehicles due to their large energy density and simple functional characteristics. In chapter 6, we present a versatile and low cost multipoint fiber optic sensing system to monitoring the thermal dynamics of batteries in a pack assembly. Based on the temperature-dependent photoluminescence property of the quantum dots (QDs), fiber optic temperature sensors were fabricated by infiltrating multimode random air hole fibers with QDs. The sensors exhibit good reversibility within the test temperature range. Using a low-cost UV diode laser as light source and a cellular phone CCD camera as detector, multi-point temperature sensing systems were developed by bundling quantum dots infiltrated random air hole fibers together. This multi-point fiber sensor system was used to monitor the temperature evolution of the battery assembly with better than 1^{o}C accuracy during the rapid charging and discharging process.

2.0 SENSOR DESIGN

As the fiber optic sensors deliver the sensing capability by detect the change of the properties in transmitted light, complex design of the fiber and interrogation method are necessary to improve the performance. The concepts of the sensors are introduced in this chapter, including the synthesis of nanostructured metal oxides thin film for chemical gas sensing, the distributed sensing scheme enabled by Rayleigh backscatter based optical frequency domain reflectometry (OFDR), and enhancement of in-fiber scattering using ultrafast laser irradiation method to endure high-temperature environments.

2.1 FABRICATION OF METAL OXIDES WITH NANOSTUCTURE

Most of the fiber optic chemical sensor is based on the fiber coated with functional materials. The high temperature stability of both the fiber and the coating materials are significantly important to the sensor working in high temperature. The hydrogen sensors in this work is based on optic fibers coated with Pd-TiO_2 nanostructured thin film. The hydrogen concentration can be measured by the absorption coefficient change and evanescent field interaction in sensitive cladding. To better understand the sensing principles, the synthesis of nano-structure metal oxide with dopants and the concepts of evanescent wave will be briefly introduced.

One of the important material parameters for metal oxide films are their refractive indices. The functionality of these metal oxide materials depends on the tuning ranges of their refractive indices. For example, high-performance anti-reflection coatings on photovoltaic solar cells need multi-layer coating of metal oxide with refractive indices n from ~1.05 to 2.2. These metal oxide optical films have been produced using conventional semiconductor processing techniques such as sputtering coating. Controls of refractive indices of optical films are typically achieved by switching different metal oxide materials and through highly specialized vacuum deposition schemes. However, these traditional manufacturing schemes are either limited by the availability of useful materials or lack of scalability due to its high manufacturing cost and low throughput.

In the last decade, a number of nano-engineering schemes have been developed to continuously tune the optical properties of metal oxide materials. These new manufacturing schemes provide a scalable way to explore possibilities to improve throughput and yield of existing products and to develop exciting new applications. For example, the continuous and wide range of tuning of refractive indices of optical materials can be extremely useful in transformation optics. Due to its tensorial origin [11], most of the transformation optics designs require strong refractive index gradients for the realization of devices, which are very difficult to manufacture by conventional means[12].

In other applications, refractive index control enables new classes of applications that were not previously possible. The integration of these metal oxide functional materials with optical fiber for optical sensing is such an example. Recent advance in nanomaterial synthesis has provided effective techniques to structure metal oxide materials in ordered three dimensions at the sub-wavelength (<20-nm) scales[13]. Block-copolymer template combined with sol-gel

solution processing approach allows the synthesis of nano-porous structured thin films of metal oxides or silica [13]. And this synthesis process can be performed in presence of dopants such as Pd and Pt. According to Maxwell-Garnet effective medium theory [14], the effective dielectric permittivity can be modified when geometrical features of nanostructures are much smaller than the wavelength of the light. Thus, these new manufacturing schemes provide a feasible way to overcome the problems when integration optical fiber with metal oxides. The continuous and wide range of tuning of refractive indices of optical materials can be extremely useful in transformation optics. Despite of the intrinsic properties of the material, the sensitivity to gases is also related to the structure of the sensing material, especially on the porosity and grain size [15]. Nanostructured material is believed to be more sensitive to chemicals due to the increased surface-to-volume ratios and reduced cross sections [16].

To engineer refractive index or dielectric permittivity of metal oxides using nano-engineering scheme is a relatively old idea [14]. Based on Maxwell-Garnet effective medium theory [14], the modification of dielectric permittivity requires that the geometrical features of nanostructures are much smaller than the wavelength of the light. Recent advance in nanomaterial synthesis has provided effective techniques to structure metal oxide materials in three dimensions at the sub-wavelength (< 20 nm) scales. The present work employed a template based sol-gel chemistry manufacturing approach to produce nano-porous metal oxides such as SnO_2, TiO_2, ZnO, SiO_2 and their doped variants. Using block copolymer 3D sub-wavelength nano-engineering, the refractive indices of functional metal oxides can be engineered from n~1.2 to 2.2 through the control of porosity of metal oxide with the nanostructure in sub-wavelength regime (10~15 nm). The block copolymer as structure directing agents induces the formation of the nano-porous structure upon thermal removal. Nano-structured metal oxides on this scale

ensure the full modulation of the material providing enhancements in sensitivity and response times.

Block copolymers are an interesting type of polymers widely used for nanostructure synthesis [17]. A rich group of nanostructures can be obtained by templating with block copolymers, where in most cases polymers form interconnected structures, and functional materials infiltrate voids. From the available block copolymers Pluronic F-127, a triblock copolymer, was chosen since it has higher temperature stability and it is known to form 3D interconnected structures in most cases [13]. Block-copolymer template combined with sol-gel solution processing approach allows the synthesis of nanoporous structured thin film of metal oxides or silica [13]. The polymer template will be removed after pre-heat treatment and the crystalline nanoporous structure will be directly developed around the template. The porosity of the film can be tuned by controlling the mole fraction of the copolymer with respect to the metal source, which will allow us to tune the effective index of the film.

In this work, metal chlorides or alkoxides were used as the precursor of the sol-gel solution in our experiment. HCl was used as a stabilizer. Pluronic F-127 was used as the structure template. First, a certain amount of HCl (37%) and ethanol were mixed together with precursor. And different amount of Pluronic F-127 was added into the solution to obtain different porosity. Then the solution was stirring for 1 hour at 60^{o}C on the hot plate to obtain a homogeneous solution. Afterwards the solution was cooled to room temperature and aged for 24 hours. The whole process can also be performed in the presence of dopants, such as Pd. The thin films were produced by spin coating the solutions on silicon wafer in order to characterize the refractive index of nanoporous SiO_2 and TiO_2 with different porosity. Each solution was spin-coated at 2500 rpm for 30 seconds on silicon wafer. The freshly coated wafers were placed in an

oven and preheated to 60°C, followed by a heating treatment at 130 °C for 1 hour. Then the temperature slowly increased (1 °C/minute) to 600 °C and held there for 1 hour. Afterwards, the samples were cooled to room temperature at 3 °C/minute. Transmission electron microscopy (TEM) was used to observe the structure of synthesized thin film, and spectroscopic ellipsometer was used to measure the refractive index and the porosity of the film.

Figure 1(a) presents a TEM image of refractive index controlled TiO_2. The interconnected 3D structure with features about 20 nm regimes, which are formed by the use of block copolymer Pluronic F-127, is clearly visible. The pores keep almost circular shape and are distributed uniformly. According to effective medium theory, the refractive index of a material can be lowered by introduction of no scattering porosity [18]. This deep sub-wavelength feature formed by block copolymers template combined with the solution processing provides a way to tailor the index of the SiO_2 and TiO_2 as we expect. Figure 1(b) and (c) summarize refractive indices of nano-porous TiO_2 and SiO_2 coated on silicon wafer with different porosity. The refractive indices were obtained by a Jobin-Yvon UVISEL spectroscopic ellipsometer. The measurement data were fit using minimization algorithms. Results presented in figure 1(b)-(c) show that the index of SiO_2 and TiO_2 can be modified in a large range as desired. The refractive indices of the nanoporous SiO_2 can be modified down to about n~1.2 at 800 nm. For nano-porous TiO_2 film, the measured refractive index can be much lower than fully dense TiO_2 and the index can be modified to compatible with silica based optical components. At 1550 nm, the index of TiO_2 with porosity 50% is about 1.43. This value is slightly lower than the D-shaped fiber intrinsic core index of 1.46, which will ensure that the light will be confined in the core of the fiber and minimize the unwanted transmission loss after coating.

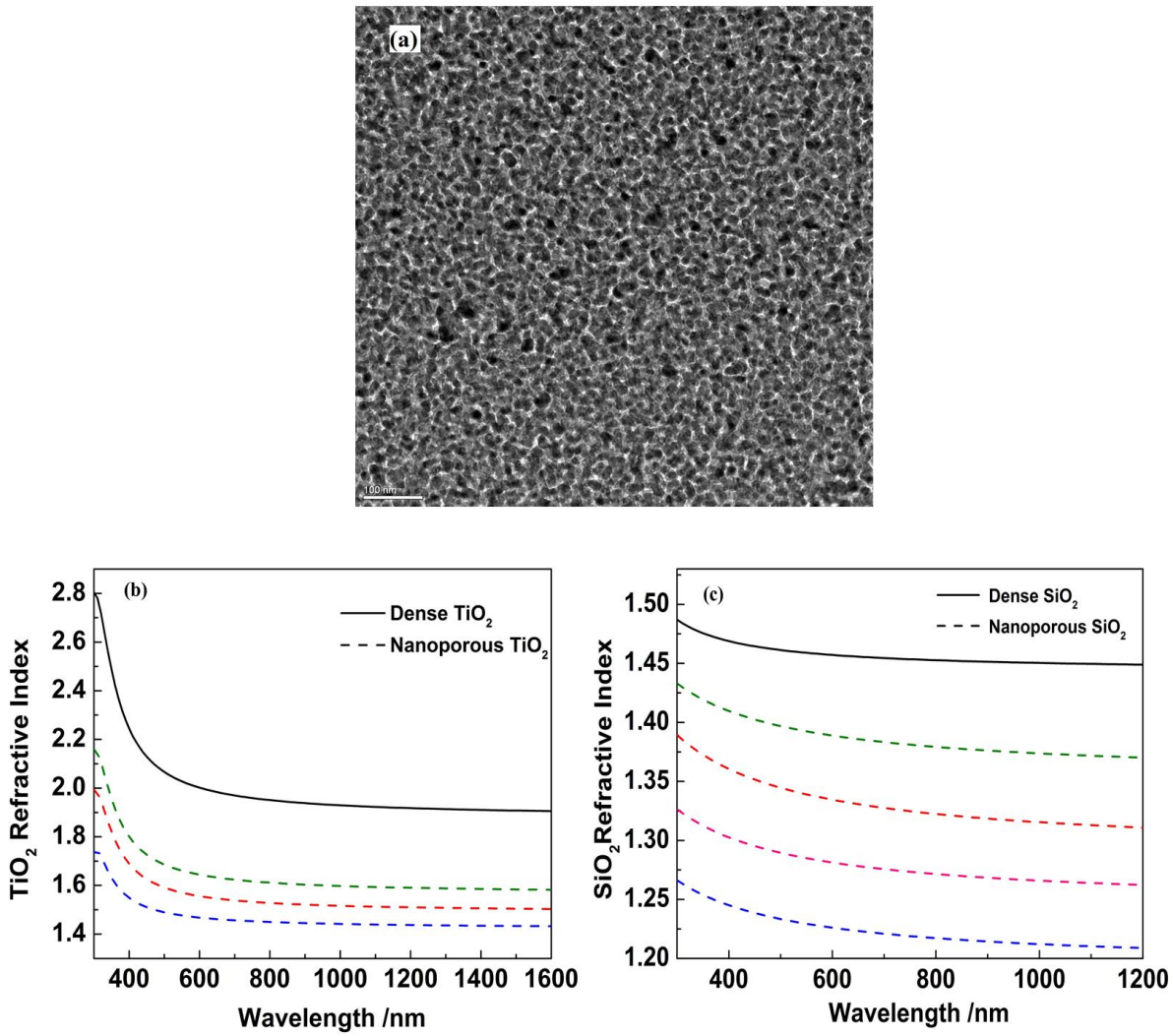

Figure 1. Refractive index engineering of metal oxide films with nanostructure. (a) TEM picture of the TiO_2 film synthesized by using block-copolymer template combined with sol-gel solution processing; Refractive indices of the (b) nanoporous TiO_2 and (c) nanoporous SiO_2 film with different porosity.

2.2 PALLADIUM DOPED TITANIUM OXIDE

Semiconducting metal oxides are widely used in gas sensors. The sensitivity is determined by the reaction efficiency between the gas and sensing material at the surface. Thus, the sensitivity of the sensor can be enhanced by improving the catalytic activity of sensing material. However, the pure metal oxide shows slow response to participation gas, poor sensitivity or weak selectivity at high temperatures [1, 19, 20]. Several methods such as changing the chemical composition, modification by noble metal nanoparticles and microstructures are used to enhance the performance of the metal oxides based sensors.

Noble metals, including Au, Ag, Pt and Pd, are highly effective oxidation catalysts with high activity, selectivity and stability under various reaction conditions. The hydrogen or oxygen is very active due to its dissociative adsorption through d-electron of out of shell of noble metal atoms. Thus, the sensitivity of the metal oxides gas sensor can be enhanced by decorated with noble metals nanoparticles at the surface. Noble metals have be reported to improve the sensor performance by a wide diversity of methods, such as sol-gel, sputtering and thermal evaporation [1, 21-24]. In this work, sol-gel solution based co-polymer templating low-cost and scalable manufacturing scheme are used to develop metal nano-particles embedded nano-materials. We have carried out preliminary works to incorporate metal nano-particles in mesoporous metal oxide with pore size between 15 and 20 nm using co-polymer templating scheme.

Palladium (Pd) incorporating has been theoretically and experimentally confirmed as a feasible way to improve selectivity and sensitivity of the sensor for hydrogen measurement [25, 26]. To develop metal oxide sensitive to hydrogen, Pd dopants were incorporated into the TiO_2. The Pd

incorporated TiO_2 for sensor use was synthesized using the alkoxide route of sol-gel method. Titanium isopropoxide ($Ti(OCH(CH_3)_2)_4$) was used as precursor. Palladium chloride ($PdCl_2$) was utilized as dopant. The molar ratio of Pd and Ti was 0.03. Room-temperature 0.5 g ($Ti(OCH(CH_3)_2)_4$) was added into a mixture of 2.5 g ethanol and 0.25 g HCl during stirring. Pd solution was prepared by adding 0.02 g $PdCl_2$ (corresponding to 3 at.% of Ti atoms) into 1.85 g ethanol, and 0.15 g HCl was added to enhance the solubility of $PdCl_2$. The mixture was stirred 3 hours to completely dissolve the $PdCl_2$. Then two solutions were mixed together with 0.5 g Pluronic F-127, followed by stirring for 12 hours at 60 ^oC. Then the solution was cooled to room temperature and aged for 24 hours and ready for coating. To ensure metallic state of Pd, the spun-on sol-gel films were annealed at reducing atmosphere (H_2) at 600^oC. This process successfully yielded Pd nanoparticle uniformly distributed in TiO_2 matrices.

Figure 2(a) presents a cross-sectional TEM image of porosity controlled Pd-TiO_2. The interconnected 3D structure with features about 20 nm regime, which are formed by the use of block copolymer Pluronic F-127. The Pd nanoparticles are clearly visible in TiO_2. Figure 2(b) illustrates a HRTEM image obtained from single Pd nanoparticle. The size of the Pd nanoparticle is about 5 -15 nm and could be indexed to the FCC Pd phase according to the HRTEM diffraction patterns in figure 2(c). The size and distribution of Pd nano-particles can be controlled via $PdCl_2$ concentration, annealing temperature, and other factors. Using a similar synthesis route, other nano-particles such as Ag and Au with various size and concentrations can be incorporated into mesoporous TiO_2. The current co-polymer templating approach can also easily incorporate pre-fabricated metal nano-particles that are commercially available or be synthesized from other chemical approaches. Thus, it will allow us to also incorporate core-shell structures into the mesoporous TiO_2.

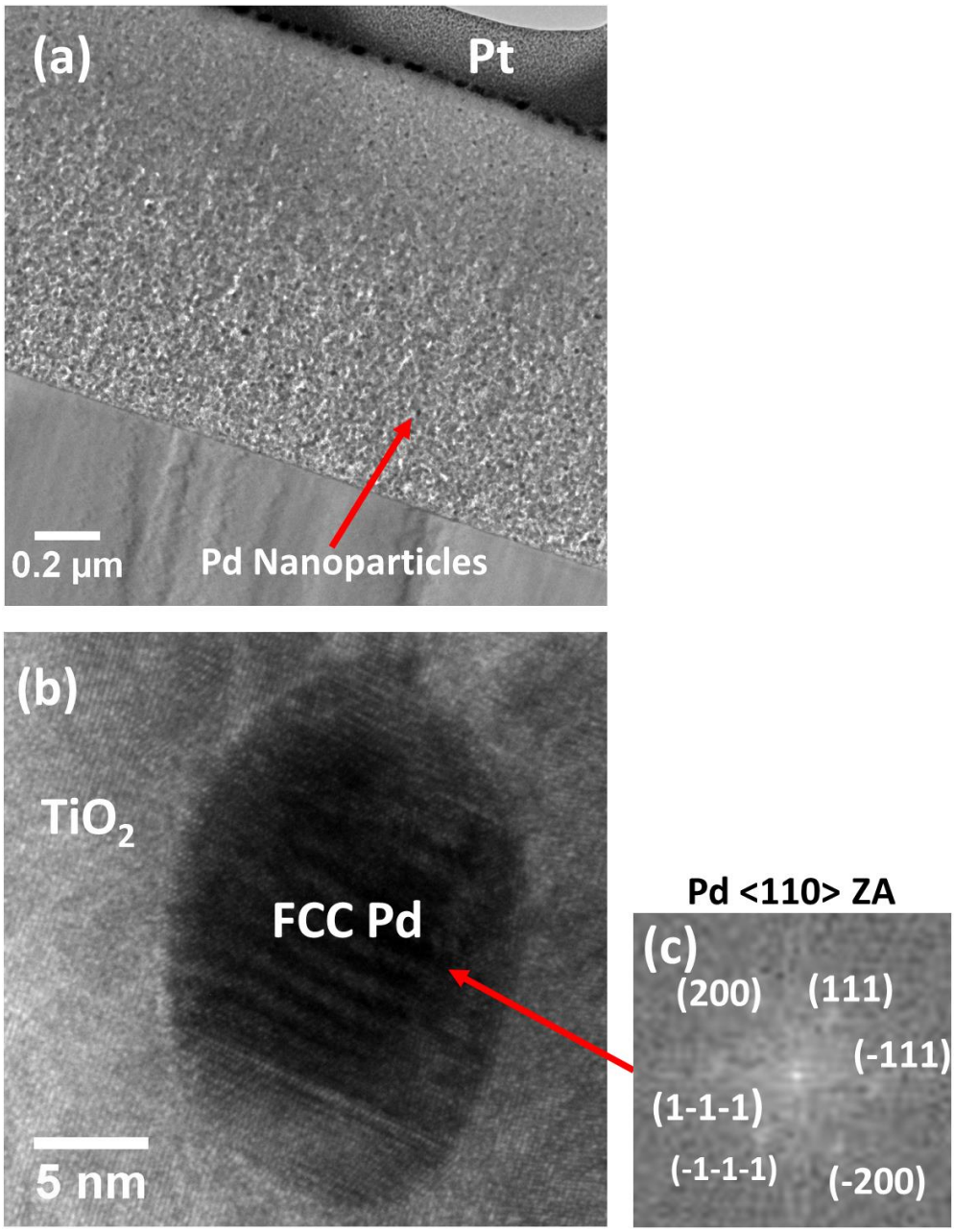

Figure 2. Metal oxide thin films with dopants coated on optical fiber. (a) Cross-sectional TEM image of the nanostructured Pd-TiO_2 prepared by focused ion beam (FIB) lift-off procedure (protective Pt overlayer is deposited before and during FIB sample preparation), (b) HRTEM image obtained for the Pd nanoparticles incorporated with TiO_2, (c) HRTEM diffraction patterns of the Pd nanoparticles.

2.3 FIBER-OPTIC EVANESCENT-WAVE AND SENSORS

Fiber optic sensors based on evanescent wave interactions have been widely used in physical parameter measurement[27-29], chemical detection[30, 31] and biological applications[32, 33] due to their fast and reliable measurements, immunity to electromagnetic noise, intrinsic safety, and possibility for remote and real-time monitoring. These sensors are approached in terms of measuring the optical loss or absorption spectra of chemicals after the interaction between the evanescent wave and analyte. The evanescent field will exponentially decay with the distance from the interface and therefore define a very short sensing range. Thus, the evanescent wave based fiber sensors usually require immobilization of the functional materials on or near an optical interface with appropriate configurations. In order to enhance the sensitivity, a large variety of configurations were used to take full advantage of the interacting evanescent fields [27, 29, 34-36]. Among these techniques, the porous coatings approach offers many advantages including feasible fabrication process, large surface area for chemical absorption and enhancement of evanescent field.

The evanescent waves are formed when light is totally internal reflected at the interface of two media with different refractive index. The intensity of the evanescent waves decays exponentially with distance from the interface, which is characterized by penetration depth, d_p. The penetration depth d_p is define as the perpendicular distance from the interface to where the electrical field amplitude has fallen to 1/e of the amplitude at interface. The penetration depth of the evanescent waves is given by

$$d_p = \frac{\lambda}{2\pi n_1 \left[\sin^2 \theta - \left(n_2 / n_1 \right)^2 \right]^{1/2}} \tag{2.1}$$

where θ is the angle of incidence to the normal at the interface, and n_1, n_2 are the refractive index of the media. As in fiber, n_1 and n_2 are the refractive index of core and cladding, respectively. The penetration depth of the evanescent wave in fiber is usually less than the λ, so it's very important to control the penetration of the evanescent wave into the low index medium in some applications.

When using fiber as a sensing platform, the functional materials or analyte will be immobilized on the fiber, on which it can be considered as fiber cladding. As equation (2.1) shows, the penetration depth will increase when refractive index of the cladding increase. Mode analysis simulations were performed with COMSOL to examine how the different refractive indices of the coating influence the distribution of the fundamental mode of the D-shaped fiber sensor. D-shaped fiber is an optimized platform for sensing applications since half of the cladding material removed to better incorporate with sensing materials. The coating thickness is 2 μm**.** The fiber core and cladding refractive index was set to 1.4535 and 1.45 at wavelength of 1550 nm. The light was almost totally confined in the fiber itself without coat on the bare side as figure 3(a) shows. When the refractive index of the coating is set to 1.45, the evanescent wave will penetrate into the whole coating, as figure 3(b) shows. If we keep increasing the refractive index of the coating to exceed the fiber core, the light will couple into the coating layer, which means the output power will fall dramatically considering the absorption of the coating material. So, in order to get better enhancement of evanescent wave as well as sensing performance, the refractive index of the coating should be tuned to slightly lower than the core.

Fiber based gas sensor is fabricated by locally replacing the cladding with the sensing material. When considering the absorption of the evanescent wave in sensing medium, the power transmitted by the optical fiber can be described by[37]

$$P(z) = P_0 \exp(-\gamma z) \tag{2.2}$$

Where z is the distance along the fiber, P_0 is the transmitted power without absorbing medium, and γ is the absorption coefficient of evanescent wave. For a specific mode transmitted in the fiber, the γ absorption coefficient of evanescent wave can be written as

$$\gamma = NT \tag{2.3}$$

Where N is the reflection number on unit length and T is the fraction of loss per reflection. Obviously, γ is also determined by bulk absorption coefficient α of the sensing medium. The relationship between the γ and α in multimode fiber can be given by[37, 38]

$$\frac{\gamma}{\alpha} = \frac{1}{V}\left(\frac{\theta_z}{\theta_{c0}}\right)^2 \frac{1}{\sqrt{1-\left(\theta_z/\theta_{c0}\right)^2 \sin^2\theta_\varphi}} \tag{2.4}$$

where θ_z and θ_φ are the angle the ray makes with the core axis, θ_{c0} is the complementary angle of the critical angle, and V is the normalized frequency parameter of the fiber given by

$$V = \frac{2\pi a}{\lambda}\sqrt{n_{co}^2 - n_{cl}^2} \tag{2.5}$$

For the fiber coated with engineered refractive index of nanoporous metal oxide, weakly guiding approximation can be used here. Combining with eliminating the skew rays the absorption coefficient of evanescent wave can be simplified to

$$\gamma = \frac{\alpha\lambda\theta_z^2}{2\pi a n_{c0}\theta_{c0}^3} \tag{2.6}$$

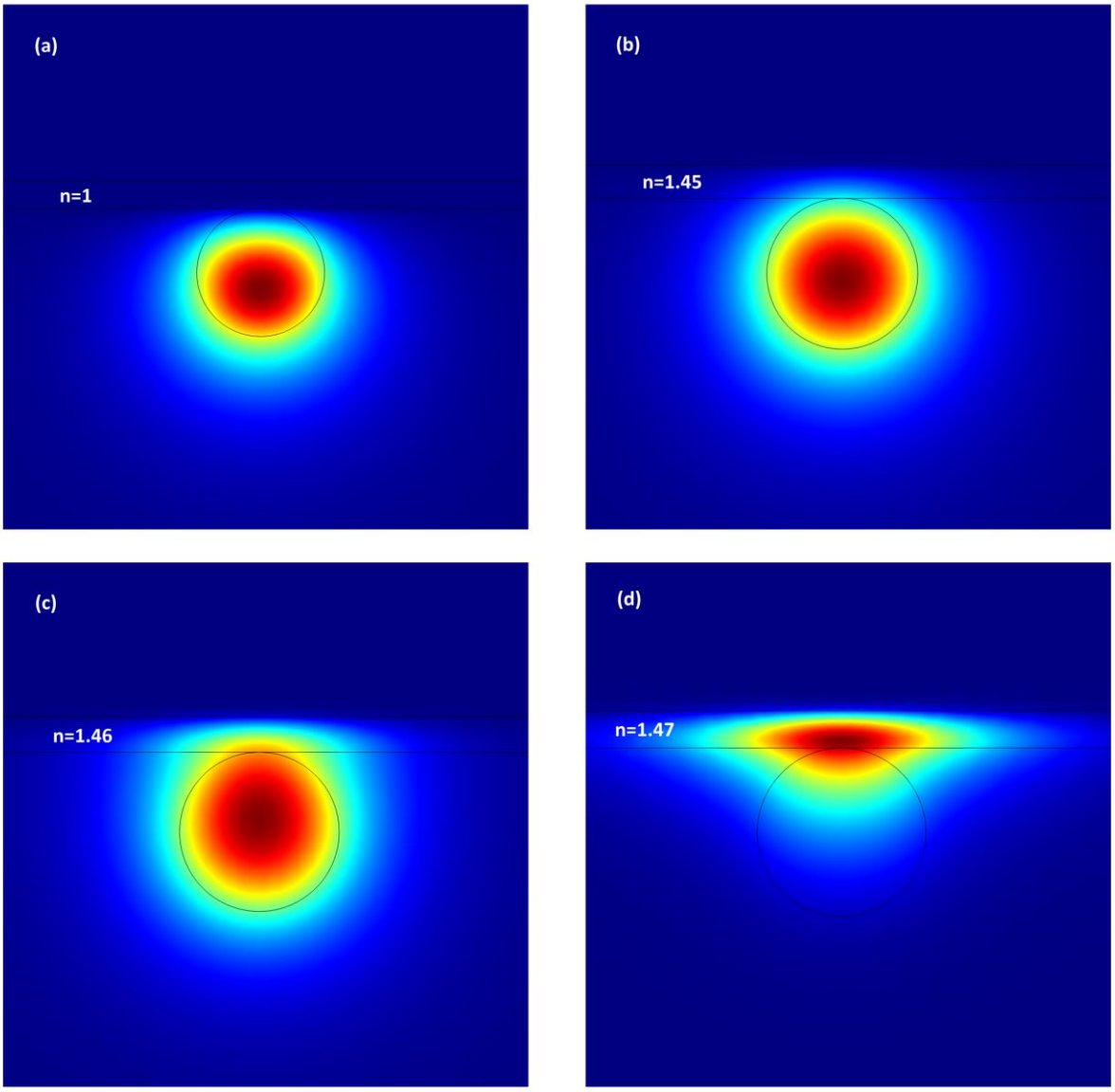

Figure 3. Simulation light intensity distribution in D-shaped fiber with bared side coated with 2 μm thick sensing material of different refractive index: (a) n=1(without coating); (b) n=1.45; (c) n=1.46; (d) n=1.47. The refractive index of the core and cladding is 1.4535 and 1.45 respectively.

2.4 OPTICAL FREQUENCY-DOMAIN REFLECTOMETRY BASED ON RAYLEIGH SCATTER IN FIBER

2.4.1 Overview

Optical fiber based sensors have been attracting a great research and widely used in many applications for several decades. They offer superior advantages over conventional electrical competitors, which attributes to their low manufacture cost, flexible structure, small size, immunity to electromagnetic fields, the capability of distributed sensing and the capability of operation in harsh environment. The most widely used optical fiber-based sensor should be fiber Bragg Gratings (FBG) due to its ability to significantly enhance sensitivity and reliable sensing performance in static and dynamic measurement [39]. At the same time, the low transmission loss and wide optical bandwidth of the optical fiber enable the potentials in remote and distributed measurement. A single FBG on fiber is usually used as the smallest sensing unit, which can only detect a single point along the fiber. Distributed sensing capability can be achieved by multiplexing different FBGs with non-overlapping spectral reflections [40, 41], or weak FBGs with same spectral reflection [42]. However, the spatial resolution and sensing range are still limited by the size and integration density of the FBGs, and the number of gratings that can be multiplexed. A truly distributed optical sensor is expected to be capable to obtain the information along the fiber at any location with longer detecting range. With the adequate spatial resolution and coverage, it can map out the 2-D or 3-D distribution of the temperature, strain, or other quantities. On the other hand, when light transmit in the fiber, the photons will interact

with the fiber material by Rayleigh, Brillouin and Raman scatterings, which rely on the local features such as temperature and strain [43, 44]. Dynamic density variation in fiber itself or generate by acoustic wave may be affected by the local temperature or strain which will leads to intensity, phase, polarization, frequency or delay time of light scattered along the fiber. Thus, distributed sensing interrogation can be realized by detecting the scattering light in the fiber combing with time domain or frequency domain method to resolve the location information.

Using the Brillouin scattering in fiber for sensing, which proposed in 1989, was the first truly functional distributed fiber optical sensing by utilizing the structural property of fiber itself [45]. Brillouin scattering in optical fiber is arisen from the interaction between the propagating light and the density variation of the fiber, which is caused by the mechanical acoustic wave. And the frequency of the mechanical acoustic wave can be affected by the local temperature, strain or other changes which can cause effective refractive index changes [44]. Thus, we can get temperature or strain information by measuring the Brillouin frequency change and the location can be resolved by the time domain or frequency domain measurement. For Brillouin scattering sensing scheme, most distributed measurement is implemented in time domain measurement, which including Optical Time Domain Reflectometry (OTDR) and Optical Time Domain Analysis (OTDA) [46]. Due to the limitation of the electronic photon detector performance and the pulse duration, the spatial resolution of the Brillouin OTDR or ODTA system can only go down to ~ 1m. In order to further improve to spatial resolution, one alternative solution is using Optical Frequency Domain Reflectometry (OFDR). The OFDR system can retrieve the time or spatial domain information by converting the frequency response along the fiber by Fourier transform. So the spatial resolution is depending on the spectral bandwidth of the tunable laser source rather than the detector speed and pulse width. Theoretically, the spatial resolution of the

scattering signal can go down to 22 μm with a 40 nm bandwidth laser [47]. Considering the environmental noise, insufficiently linear laser tuning and excess of unbalanced dispersion in the measurement arm in practice, the temperature or strain sensing spatial resolution is about 1 cm [48]. Also, due to the weak signal from Brillouin scattering and the resulting low SNR, the temperature accuracy of sensing is only around 1^{o}C and around 20με of strain accuracy. On the other hand, the Rayleigh scattering signal is 15-20 dB stronger, which can give much higher SNR, therefore improve the temperature and strain sensitivity. Rayleigh scattering is an elastic scattering of light by subwavelength-size particles during light propagation. In optical fibers, the random nature density fluctuations of silica material give rise to the Rayleigh scattering loss. Such randomly varied density distribution can be interrogated by OFDR method and with cross referencing between the Rayleigh scattering signatures of the original optical fiber and the same one under perturbation, the ambient perturbation can be quantified. The OFDR method based on in-fiber Rayleigh scatter can provide distributed strain, temperature and loss detection with centimeter resolution. Recently, distributed sensing using OFDR in-fiber Rayleigh scattering measurements was reported with sub-centimeter spatial resolution and1 με and 0.1 ^{o}C accuracy for strain and temperature measurement [48-51]. In this dissertation, further employ this technique, combined with ultrafast laser processing, functional nano-materials and specialty optical fibers to probe high temperature and chemical gradients with high spatial resolution in harsh high-temperature environments.

2.4.2 Operation Principle

Due to the random order of the molecules and the presence of dopants, inhomogeneous density and structure variations are frozen into the fused silica during the manufacture, resulting in

Rayleigh scattering in fiber. Rayleigh scattering in fiber is elastic scattering, which means there is no frequency change of the scattered light compared to the incident light. It's a linear scattering process in that the scattered power is simply proportional to the incident power with intensity proportional to $1/\lambda^4$. The Rayleigh scattering is a fundamental loss related to the intrinsic property of the material, and determines the loss limit of the optical fiber. Therefore, it can't be eliminated although the intensity may be reduced by improving the manufacturing process. However, the Rayleigh scattering in the fiber also contains the perturbation information along the fiber, which is to the benefit of the sensing applications instead of light transmission. Rayleigh scattering light in fiber emits towards all directions from the scattering centers, while part of the scattering light will be confined by the fiber and propagate in backward direction. This backward propagating scattering light has a time delay with the reference light, which can be used to trace the location by OFDR system. By comparing the Rayleigh scattering under detection ambient with the original Rayleigh scattering, the OFDR can provide distributed measurement of environmental parameters such as temperature and strain with sub-centimeter resolution [47, 52].

OFDR system has been widely used for its capability of providing shorter spatial resolution in millimeter scale and relatively lower cost at the same time. The operation mechanism of the Rayleigh scattering measurement based on OFDR has been studied in detail recently[47-52]. The schematic of the typical OFDR optical network for Rayleigh scattering measurement is shown in Figure 4. It includes a tunable laser source (TLS), a fiber Mach-Zender interferometer and photodetectors. This system uses swept-wavelength coherent interferometry technique, in which the frequency of the laser source is linearly tuned with time. If we define the laser sweep rate as γ, then the frequency of the light from the tunable laser can be described as

$$\omega(t) = \omega_0 + \gamma t \tag{2.7}$$

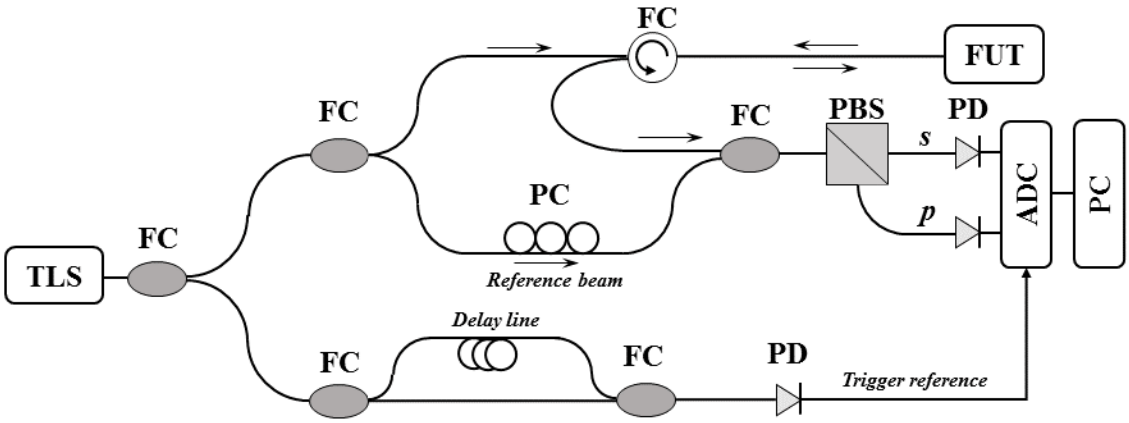

Figure 4. Schematic of the OFDR optical network for Rayleigh scattering measurement. TLS: tunable laser source; FC: fiber couple; PC: polarization controller; PBS: polarization beam splitter; PD: photodetector; FUT: fiber under test.

The light from the laser is then spit and coupled into an auxiliary interferometer and a measurement interferometer. The light in the upper Mach-Zender interferometer is further split into the measurement arm and reference arm using fiber coupler. The light in the measurement arm will finally be coupled into the fiber under test (FUT). The Rayleigh back-scattering light from the measurement arm will be recombine with reference beam and interference signal will be recorded by the detector. In order to briefly explain the principle, we can ignore the polarization diverse first. The electric field of the input light wave can be considered as

$$E_{in} = E_0(t)e^{-i\omega(t)t} \tag{2.8}$$

where, $\omega(t)$ is the instantaneous angular frequency of the tunable laser. Then the input field was split into reference arm and measurement arm and the filed E_r and E_s can be described as

$$E_r = E_0(t+\tau_1)e^{-i\omega(t+\tau_1)t} \tag{2.9}$$

$$E_s = E_0(t+\tau_2)e^{-i\omega(t+\tau_2)t} \tag{2.10}$$

whre τ_1 and τ_2 is delay from the reference arm and measurement arm respectively. If the Rayleigh scattering from the FUT has frequency response with amplitude gain $\rho(\omega)$ and phase change $\varphi(\omega)$, the field of the scattered light at the recombine coupler is

$$E_R = E_0(t+\tau_2)\rho(\omega)e^{-i\omega(t+\tau_2)t+i\varphi(\omega)} \tag{2.11}$$

Thus, the filed after recombined during the laser scanning at time t equals the sum of fields from the reference arm and back-scattering Rayleigh signal:

$$E_{out} = E_r + E_R = E_0(t+\tau_1)e^{-i\omega(t+\tau_1)t} + E_0(t+\tau_2)\rho(\omega)e^{-i\omega(t+\tau_2)t+i\varphi(\omega)} \tag{2.12}$$

The photodetector can only response to the intensity of the combined fields, which is given by

$$I_{out} = \left|E_0(t)\right|^2 + \left|E_0(t-\tau)\rho(\omega)\right|^2 + 2\rho(\omega)E_0(t)E_0(t-\tau)\cos\left[\omega(t)\tau - \varphi(\omega)\right] \tag{2.13}$$

where, $\tau = \tau_1 - \tau_2$, is the time delay difference between the reference arm and measurement arm paths. Apparently, we also have $\tau = 2nx/c$, which present the time delay at position x of the fiber under the test. So location information is encoded into the interference output in frequency domain. By Fourier transforming the intensity obtained in 2.13, the frequency response of the fiber can be converted into the time domain, from which the location information can be retrieved. Thus, the spatial resolution of measurement, which related to the time domain resolution in another word, is determined by the spectral bandwidth of the tunable laser scan range as[47, 48]

$$\Delta z = \frac{\lambda_s \lambda_f}{2n_g \Delta\lambda} \cong \frac{c}{2n_g \Delta f} \tag{2.14}$$

where λ_s and λ_f are the start and finish scanning wavelength, n_g is the refractive index of the fiber under test, and $\Delta f = c\Delta\lambda / \lambda^2$. The equation (2.14) indicated that the spatial resolution is not

depending on the sampling rate of the detector. Benefit from the large scanning range of the tunable laser source, the spatial resolution can be easily push down to millimeter or even lower. For example, a scanning range from 1535 nm to 1575 nm corresponds to 20 μm spatial resolution of Rayleigh scattering signal measurement. The maximum detection length $L_{\max}$ is determined by the sampling rate and tunable laser scanning rate as [48]

$$L_{\max} = \frac{c}{4n_g}\frac{R_s}{\gamma} \tag{2.15}$$

where R_s is the average sampling rate. In swept-wavelength OFDR system, the sampling rate R_s is triggered by an auxiliary interferometer to eliminate the nonlinearity of the tunable laser sweep. So the sampling rate is determined by the differential delay in the unbalanced auxiliary interferometer τ_g and laser sweep rate γ as $R_s = \gamma\tau_g$. Therefore, the equation (2.15) can be re-written as

$$L_{\max} = \frac{c\tau_g}{4n_g} \tag{2.16}$$

A maximum detection length of 40 m can be reached by using 800 ns differential delay [47]. Besides, the maximum detection length is also limited by the coherence length of the light source. By using a phase-reconstruction scheme, the range can be extended to 1km with lower resolution [43].

The polarization state of the Rayleigh scattering in the FUT continuously changes along the fiber, attributing to density fluctuation caused by the inhomogeneity of the fiber and the birefringence from temperature or strain change. By using a polarization beam splitter (PBS) right after the recombination, the reference field can be two orthogonal states and the change of the polarization state in ***s*** and ***p*** components can be tracked along the FUT.

A cross-correlation is performed for each segment to determine the spectral shift between the reference and perturbed profiles. The spectral difference between the shifted peak and un-shifted peak is directly proportional to the temperature or strain changes in each segment.

Rayleigh scattering itself is independent to the temperature and strain in optical fiber, which means its amplitude and phase keep stationary although they are random along the fiber. So the fiber under the test can be considered as a weak FBG with random period. The change of the sensing length in specific segment will equivalently change the period of the FBG, thus change the spectral response in this segment. For distributed strain or temperature sensing, a reference Rayleigh scattering signature of the FUT is taken first and then Rayleigh spectral shifts for each FUT interval is determined by cross-correlating with a pre-measured reference [48]. The strain or temperature change corresponding the spectral shift is similar to the fiber Bragg grating, and can be interrogated as

$$\frac{\Delta \nu}{\nu} = -\frac{\Delta \lambda}{\lambda} = -K_T \Delta T - K_\varepsilon \Delta \varepsilon \tag{2.17}$$

where K_T and K_ε are temperature response coefficient and strain response coefficient, respectively. The spatial resolution of the stain and temperature measurement is determined by the gauge length used for cross-correlating. The stain and temperature resolution is constrained by the relationship as [52]

$$\Delta L * \left(K_T \Delta T \right) = \Delta L * \left(K_\varepsilon \Delta \varepsilon \right) = \frac{\lambda}{4n} \tag{2.18}$$

So, the un-certainty of the stain or temperature measurement can be reduced by increasing the gauge length of the cross-correlation. However, the detector intensity noise will increase along with the increase of the gauge length [53]. So there is a trade-off between the gauge length and

detector intensity noise. For example, temperature resolution of 0.1°C or strain resolution of 1με can be achieved with a 1-cm gauge length for cross-correlation.

2.5 FORMATION OF NANOGRATINGS IN SILICA OPTICAL FIBERS BY ULTRAFAST LASER IRRADIATION

2.5.1 Overview

In the last decades, many investigations on photo-induced refractive index change has been performed since the first Bragg grating was inscribed on Ge-doped silica fiber with UV laser by K. O. Hill et al in 1978 [54]. Light induced structural change was achieved due to high photon energy of the UV light ($h\nu > E_g$). In contrast, the light from pulse laser systems vary in spectrum from visible to the mid-infrared is difficult to interact with silica glass material by one-photon process due to the insufficient photon energy. However, the development of femtosecond laser enables the potential of the non-linear multiphoton absorption in silica glass for the ultrahigh light intensity. Since the first demonstration of photon induced refractive index change in glass using tightly focused red visible femtosecond laser by Davis et al in 1996 [55], a lot of research effort has devoted to the field of various three-dimensional(3D) photonic device fabrication in different transparent materials by using ultrafast laser direct writing approach [56-58]. Soon after, nanovoids was created in silica by tightly focused high quality femtosecond laser beams using large NA objectives [59]. By combining the threshold effect and the formation of periodic nanogratings, a self-organized nanoscale periodic grating was formed in the fused silica glass by using linear polarized beam irradiation [60].

2.5.2 Nonlinear Interaction Process and Formation of Nano-gratings

The advanced ultrafast laser writing has opened up new avenues in material processing such as micro machining and optical device fabrication. The material processing with ultrafast laser generally has have spatial resolution owing to the ultrashort light-matter interaction time and the ultrahigh peak power. For the most processing materials, like fused silica glass, the energy bandgap is larger than the photon energy of the ultrafast laser (the spectrum ranges from red visible to mid-infrared), which means linear absorption of the laser radiation can't occur at this situation. However, during the ultrafast laser writing process, the laser beams are tightly focused in transparent media and light intensity is ultrahigh at the focusing point. Nonlinear absorption process including multiphoton ionization and tunneling ionization will occur in this case to stimulate the valence electrons to conduction band [61].

The illustration of multiphoton ionization is presented in figure 5(a). It is a process in which a single valence electron can absorb energy from multiple photons simultaneously to exceed the energy bandgap. This phenomenon can occur when the laser intensity is sufficiently high. Take fused silica as an example, it need at least 6 photons for an electron to be promoted from valence band to conduction band. The band structure can be distorted under the irradiation of high intensity laser. So, the bound electrons can tunnel out to become a free electron when the laser field is strong enough, which is called tunneling ionization and it's illustrated in figure 5(b). The electron in conduction band can also linearly absorb multiple photons as showed in figure 5(c). When this electron absorbs enough kinetic energy to exceed the energy bandgap, it may ionize another electron in valence band by collision as figure 5(d) shows. This process will continue as long as the laser keep irradiation and called avalanche ionization. According to these process, the energy from the laser pulse is transfer to the material lattice, resulting in structural

modification such as refractive index change and nanogratings, depending on the properties of the materials itself and the intensity of the laser pulse.

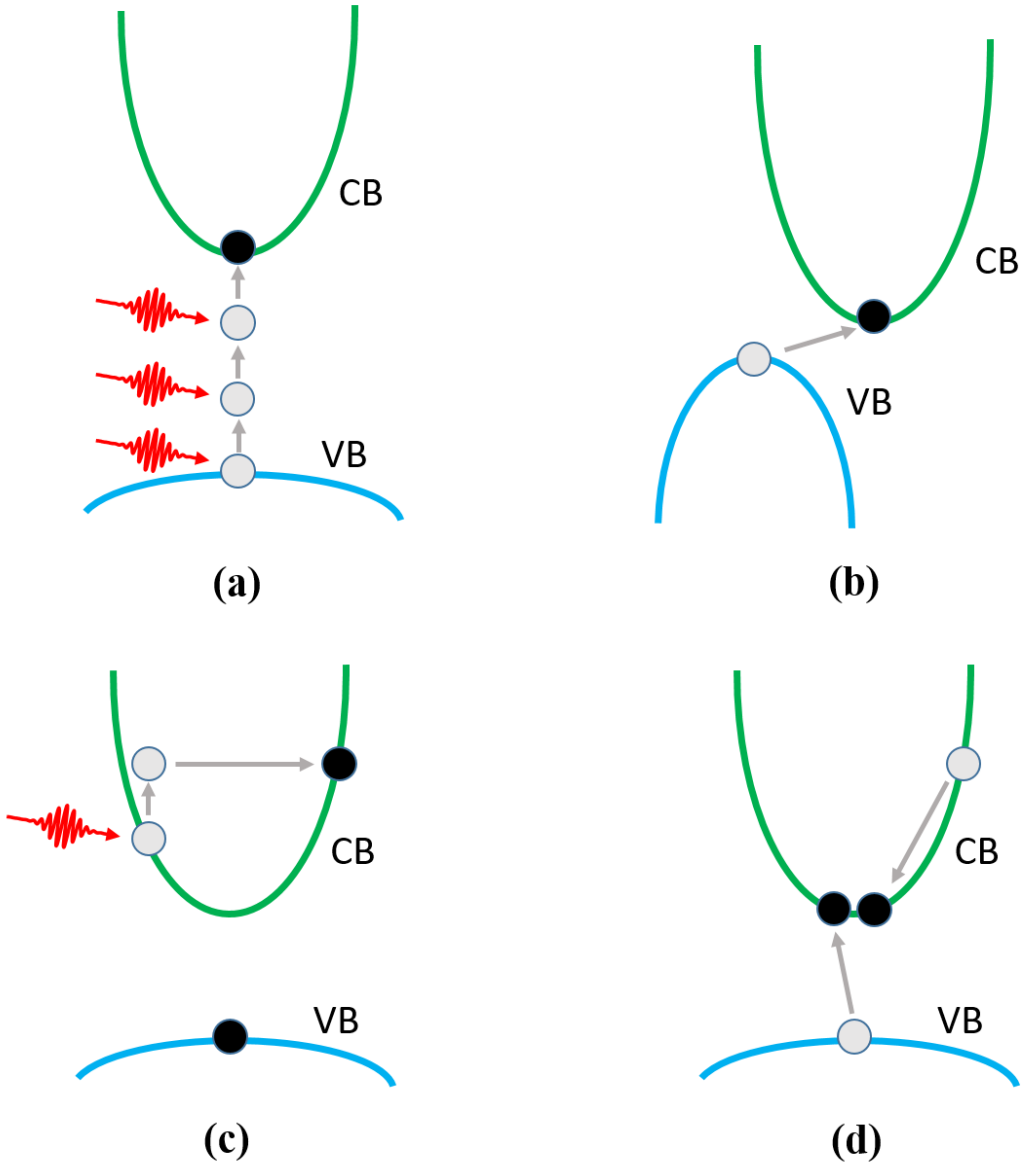

Figure 5. Illustration of nonlinear photoionization processes under ultrafast laser irradiation: (a) multiphoton ionization, (b)tunneling ionization, (c) free carrier absorption, and (d) impact ionization [61].

Structural modification in dielectric material after ultrafast laser irradiation origins from the relaxation of the photo-excited electrons. Depending on the energy density of the incident

laser pulse, there are three types of the material modification, including: smooth modification with positive refractive index change named regime 1, birefringent modification with periodic nanogratings emergence named regime 2 and disruptive modification associate with void formation named regime 3. Basically, at a fix pulse duration, the threshold energy to the next regime increases as the list order[62].

Among these three regimes, regime 2 corresponding to intermediate pulse energy has attracted a lot focus since it can be used to fabricate self-organized structure and the formed structures are stable at high temperature. Self-organized in-volume nanogratings has enabled fabrication of nanofluidic channels [63, 64] for bio-applications. The formation mechanism of the nanogratings is still under the intensive investigation and there are several explanations for the formation. Firstly when then nanograting was discovered, Shimotsuma et al claimed the periodicities were generated by an interference between the incident light field and the electric field of the induced plasma wave [65]. The material in the focusing region has high free electron density due to the multiphoton ionization. This plasma-like region will absorb light energy through one-photon process and excite plasma density waves with electric field parallel to the light propagation direction. The coupling between the plasma wave and the incident light result in the periodic modulation of the plasma concentration and therefore create nanogratings in the silica glass. The plasma wave can couple with the light wave only if they have same polarization, thus the formed nanograting is perpendicular to the polarization of the incident light.

Later Hnatovsky et al argued that the self-organized modification was formed by the evolution of nanoplasma hot-spots into disc-shaped structures and then further in to nanoplances in the presence of the high intensity polarized laser field [60]. In this theory, transient nanoplasmaonics model was proposed to describe the process from smaller structures to self-

ordered long-range scale nanoplane. Ionization hot-spots can be generated in material under high power ultrafast laser pulse irradiation. These hot-spots will evolve into spherical nanoplasmas if it's further exposed to several pulses due to the memory effect of the previous ionization [66]. The boundary effect results in electric field enhancement in the equatorial plane perpendicular to the electric field of light. So the spherical nanoplasmas will keep growing into ellipsoidal plasmas under continuous irradiation and finally evolve into plasma nanoplanes promoted by the field enhancement. The nanoplanes are randomly spaced at the beginning of the formation, and the light propagation will be re-distributed after the quasi-metallic waveguides were formed in the nanoplanes. The interference of the lower order optical mode determines the spacing between two planes to be $\lambda / 2n$. The incident light is more likely to be coupled into the nanoplanes and generate high pressure in these regions and subsequently form nanocracks under continuous irradiation.

Although half-wavelength period of the nanograting was explained to agree with their experiment, the later research found that the period could deviate from the prediction [67]. Recently researchers try to explain the mechanism by combining the both theories and take fully into account multiple effects including surface plasmonwave at interface, interference between the incident and the inhomogeneity-scattered light waves, mutual interference between the scattered waves from multiple laser-induced inhomogeneities [68]. Nanoplanes with different periods are classified into two types: low frequency nanograings ($\Lambda = \lambda / n$) and high frequency nanogratings ($\Lambda = \lambda / 2n, \lambda / 3n...$). The interference between incident light and the scattered light from a single inhomogeneity will form spherical standing waves with period $\lambda / 2n$. The nanogratings are arisen from superposition of the formed waves from randomly distributed inhomogeneities and incident light waves. The periodicity of the organized nanoplanes is

determined by the density of the inhomogeneities [68]. For lower concentration inhomogeneities, the interaction between sacatterings from nearby nanoplasmas is very weak due to the large distance, so only the interference between the incident light and the inhomogeneity-scattered light waves is taken into account. In this scenario, low frequency nanogratings is formed by the nanoplasmas elongating along the enhancement fringe perpendicular to the laser polarization direction with period λ / n . On the other hand, the mutual interference among multiple scatterings from nearby nanoplasmas becomes unneglectable for higher concentration of inhomogeneities and this mutual interference would finally lead to the formation of high frequency nanogratings. So the periodicity of the nanogratings is depending on the density of the inhomogeneities resulted from electron density. At the same time, the optical cavitation, which is the origin of the nanogratings, can only occur when the laser induced stress is larger than the Young's Modulus of the silica. Therefore, the geometry of the nanograting should highly depend on the number of laser pulses and pulse energies.

2.5.3 Inscribing Periodic Nano-gratings in Fiber

Rayleigh scattering in fiber, arising from disordered lattice with micro density and refractive variations, provide the opportunity of distributed measurement along the fiber. A lot of research focused on the scheme using optical time domain reflectometry(OFDR) with Rayleigh scatter due to its high resolution and fast scanning speed. However, due to the low amplitude of the scattering signal, the sensitivity based on Rayleigh scattering is limited. Additionally, for high temperature measurement, the thermal induced change of the density of the glass material will cause the failure of tracking the spectral shift. In order to overcome these limitation, we need to increase the scattering signal as well as the thermal stability.

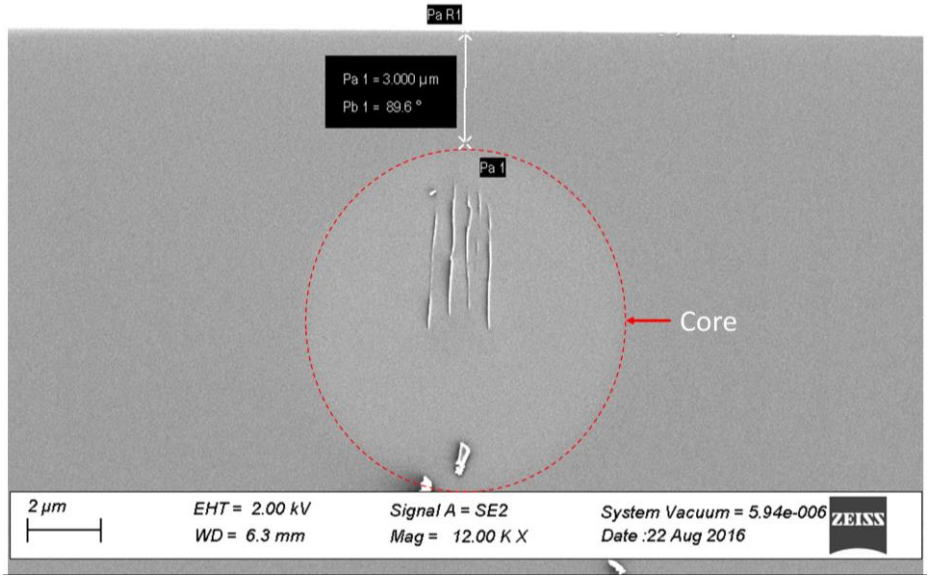

Figure 6. SEM figure of nanogratings inscribed on the core of D-shaped fiber.

The nanograting discussed in last section is a structure with relative larger random refractive index variation and is proved to be stable at high temperature, so it enabled a possibility to obtain higher scattering signal with thermal stability if the nanograting is inscribed in the fiber. Among these three regimes induced in the ultrafast laser irradiation, the smooth refractive index change from regime 1 can be erased in high temperature and the disruptive modification from regime 3 will cause huge transmission loss. For the distributed sensing scheme in harsh high-temperature environments, regime 2 corresponding to intermediate pulse energy is only choice for its thermal stability and acceptable light transmission loss of the formed structure. Figure 6 shows a nanogratings inscribed on the core the D-shaped fiber. D-shaped fiber is specialty fiber with a standard telecommunicate fiber core and a flat faucet with half of the cladding removed. The diameter of the core is ~ 9 μm and the distance to the flat surface is 3 μm, so it's easier to focusing on the fiber core without oil immerse system. Another advantage of D-shaped fiber is the strong evanescent on the flat side provide the capability of the chemical

sensing without any complicate fabrication process. For standard telecommunication fiber with circular geometry, oil immersing approach should be used to focus the laser beam into the core of the fiber.

3.0 CHEMICAL GAS SENSING USING D-SHAPED FIBER

The refractive index of the metal oxides film can be tailored using the copolymer template method to introduce nanostructures in the sub-wavelength regime at scales of 20 nm or less. With on this approach, this chapter presents the chemical gas sensor based on optical fibers coated with functional metal oxides. D-shaped fiber with have cladding removed was used in this work due to the essential mechanism of evanescent filed interaction used for chemical gas sensing. We have test the sensing performance for point sensor using fiber Bragg grating and distributed sensing using OFDR technique.

3.1 BACKGROUND

Metal oxides have been widely used in conductometric type electronic sensors, or chemiresistors, it is well known that changes in the conductive properties are to be expected. Specific doping by certain metals, such as Al, Pd, and Pt[3, 69], are known to modify the free electron concentration and mobility of metal oxides, which can enhance their sensitivity, selectivity and response times. However, these electronic sensors cannot function in harsh environments such as extremely high temperatures (e.g. <500^{o}C). In this paper, we demonstrate a fiber optical sensing technique using metal oxide nanomaterials to perform hydrogen measurement at extremely high temperature up to 700^{o}C, which cannot be attained using electronic sensors.

Hydrogen has been the focus of a great amount of attention recently as a clean and environmentally friendly energy source. However, the dangers associated with the use and storage of hydrogen has always been a tremendous problem due to the wide explosive range (4-75%) and small ignition energy (0.02mJ). Security systems monitoring of the concentration of hydrogen gas demand fast, sensitive, and reliable hydrogen sensors, especially for large scale energy generation system where a large amount of hydrogen is stored and consumed at high temperatures. Semiconducting metal oxides such as SnO_2, TiO_2, and ZnO are widely used for hydrogen gas sensing applications due to their electrical conductivity change after adsorption of hydrogen gas [70, 71]. Despite of the intrinsic properties of the material, the sensitivity to gases is also related to the structure of the sensing material, especially on the porosity and grain size[15]. Nanostructured material is believed to be more sensitive to chemicals due to the increased surface-to-volume ratios and reduced cross sections [72, 73]. Compare to other metal oxide, TiO_2 is well known for its wide bandgap and structural stability at high temperatures [72]. TiO_2 is a prototypical metal oxide for gas sensing which also exhibits suitable stability at high temperatures relevant for solid oxide fuel cells and other power generation systems [4, 23]. Nanostructured TiO_2 has been predicted and demonstrated to be an excellent candidate for ultrasensitive sensors [16]. But pure TiO_2 shows slow response to hydrogen gas and low sensitivity at high temperatures [1]. Palladium (Pd) incorporating has been theoretically and experimentally confirmed as a feasible way to improve selectivity and sensitivity of the sensor for hydrogen measurement [25, 26].

Most of the semiconducting metal oxides hydrogen sensors are electrical sensors based on resistance measurement. All optical fiber hydrogen sensors, due to their explosion proof nature anti-electromagnetic interference, have been developed as well. These sensors can

perform effective hydrogen concentration measurements at slightly low temperature, usually lower than 400 ^{o}C. The sensitivity of these sensors will degrade with the increase of temperature due to thermal instability. However, there are amount of industrial application demand to monitor the hydrogen concentration above 600 ^{o}C. To address this problem, we develop this all-optical-fiber hydrogen sensor with Pd-doped TiO_2, which can provide rapid hydrogen concentration measurement up to 700 ^{o}C. With the nanostructure in sub-wavelength regime, the refractive index of Pd-doped nanoporous TiO_2 can be tailored to match the fiber core (n_{core} ~ 1.46) according to effective medium theory. A rapid and ultrasensitive high-temperature hydrogen senor was realized by using this Pd-doped nanoporous TiO_2 thin film coated D-shaped fiber, which is an optimally designed optical fiber sensor platform. High-temperature-stabilized fiber Bragg grating is induced in D-shaped fiber for high-temperature resistance. The sensitivity of the sensor was investigated from 300 ^{o}C to 700 ^{o}C.

3.2 SENSOR FABRICATION PROCESS

The D-shaped fiber used to prepare gratings was first soaked in pure hydrogen atmosphere at T ~ 25°C, P ~ 2400 psi for more than two weeks to enhance photosensitivity. Then, the strong grating with λ_{bragg} = 1551.5 nm was inscribed into the core of D-shaped fiber by using a 248 nm KrF laser and a phase mask. The spectra and schematic of the grating are shown in figure 7. The grating was inscribed with strong reflection to survive high-temperature processing. In order to get a higher sensitivity, the residual 4 μm cladding material on the flat side of the D-shaped fiber was removed by placing it in a buffered HF solution (5 NH_4F : 1 HF) for 21minutes. After the

etching process was finished, the etched grating was rinsed several times in deionized water and ethanol. Then the grating was dried for Pd-doped TiO_2 coating.

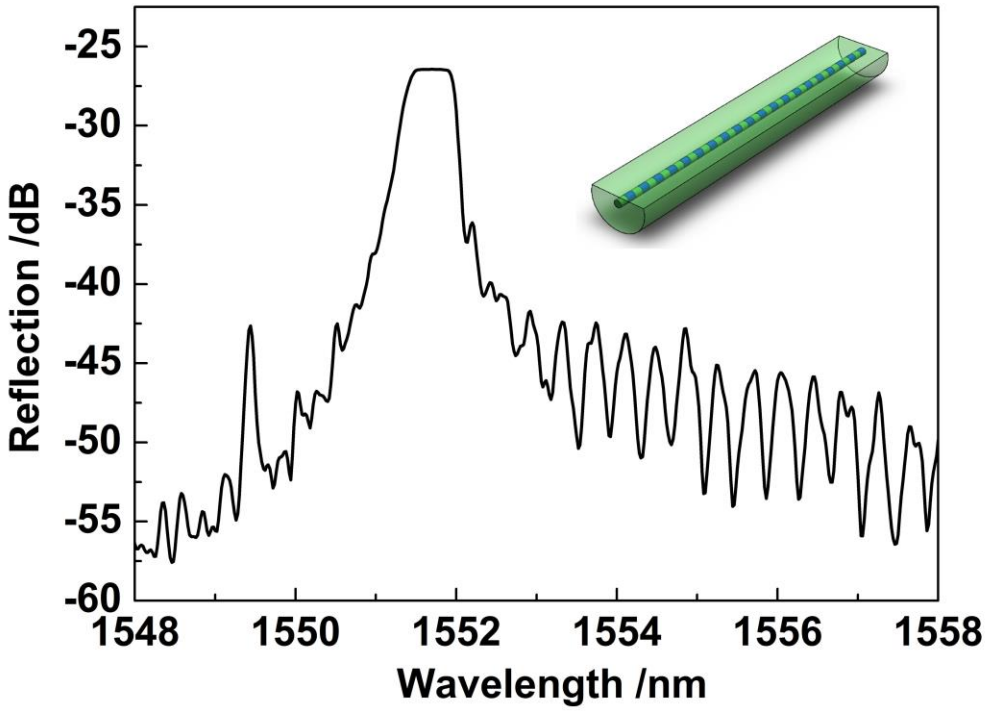

Figure 7. Schematic of the D-shaped fiber Bragg grating and the reflection spectrum of the seed grating.

The etched fiber with grating was immersed in the sol solution and coated through dip coating procedure at the speed of 0.2 mm/s. The coated fiber was dried in the air at room temperature overnight, and sol-gel Pd-doped TiO_2 film was formed by the hydrolysis. Then the coated fiber was put into a tube furnace and annealed with heating to 130 ^oC at 5 ^oC/min, and held there for 1 hour. Followed by heating to 600 ^oC at 3 ^oC/min and calcined for 1 hour. These procedures were conducted in air atmosphere. The FBG were stabilized at the same time. After these procedures, the coated fiber was cooled to 300 ^oC at 3 ^oC/min, and then switched from air gas to 5 vol. % H_2/N_2 for 1 hour with 40 ccm/min flow speed to reduce the PdO in the film. The

schematic diagram of D-shaped fiber Bragg grating hydrogen sensor characterization system is shown in figure 8. The reflection spectrum of FBG sensor was monitored by an optical spectrum analyzer. A tube furnace that can control temperature up to 800 ^{o}C was used. The fiber was inserted in a quartz tube, which was placed in tube furnace. Figure 9 shows the SEM picture of the cross section of the D-shaped fiber coated with Pd/TiO_2. The bread like interconnected 3D structure formed by the use of block copolymer Pluronic F-127 is clearly visible. The thickness of the coating is about 1μm. Two rubber ferules were used to seal both ends of the tube and to apply tension to ensure that the fiber has no contact to the inner wall of the tube. The sensor can be exposed to various concentrations of hydrogen balanced with nitrogen or pure nitrogen by using two calibrated mass flow controllers. Hydrogen concentrations from 0.25 vol. % H_2/N_2 to 5 vol. % H_2/N_2 were tested in this work.

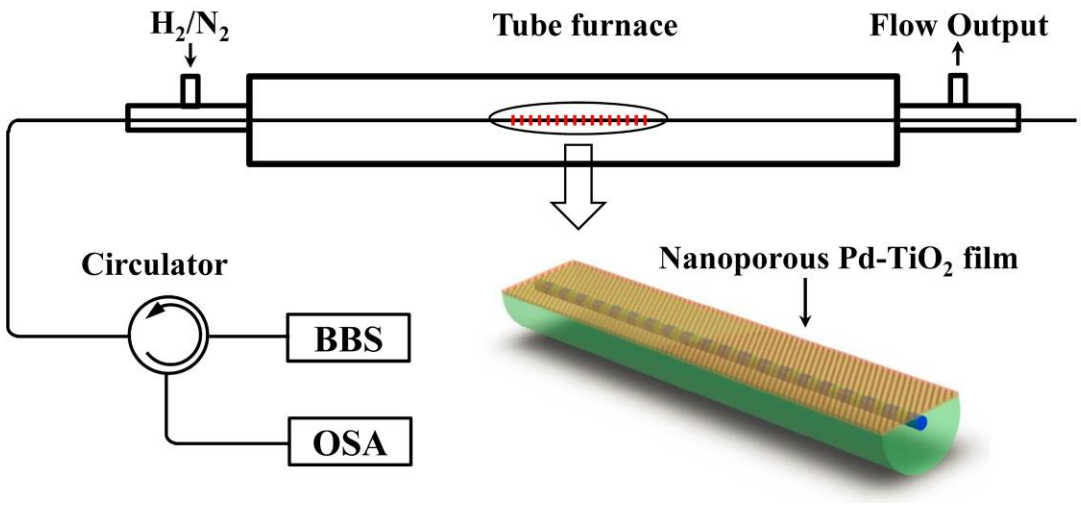

Figure 8. Schematic diagram of Pd-TiO_2 nanoporous film coated D shape FBG hydrogen sensor.

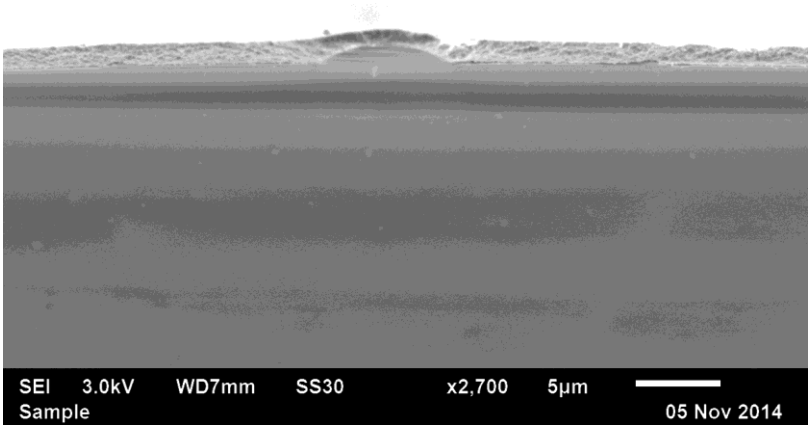

Figure 9. SEM picture of the cross section of the D-shaped fiber coated with Pd/TiO_2.

3.3 HYDROGEN SENSOR USING GRATINGS

The intensity of the Bragg resonance peak highly depends on the index of the coating. The light can barely transmit through the coated fiber before heat tread due to the relatively high index of the uncalcined film cladding. The index of the coated film will decrease when Pluronic F-127 template is removed by heating. In our experiment, the peaks disappeared after the coating and appeared again after temperature reached 300^{o}C. Then the intensity increased by the temperature. Finally, the peak stabilizes at 600^{o}C with intensity around -60 dB. Figure 10(a) shows the hydrogen response of the sensor in ambient cycled from pure N_2 to 5% H_2 in N_2, and then back to pure N_2 for several cycles at 600^{o}C. The intensity of the resonance peak decrease dramatically with exposure to H_2 and goes back when N_2 is restored. After the system was flushed with nitrogen gas, the results were repeatable with very small amount of baseline drift. This indicates

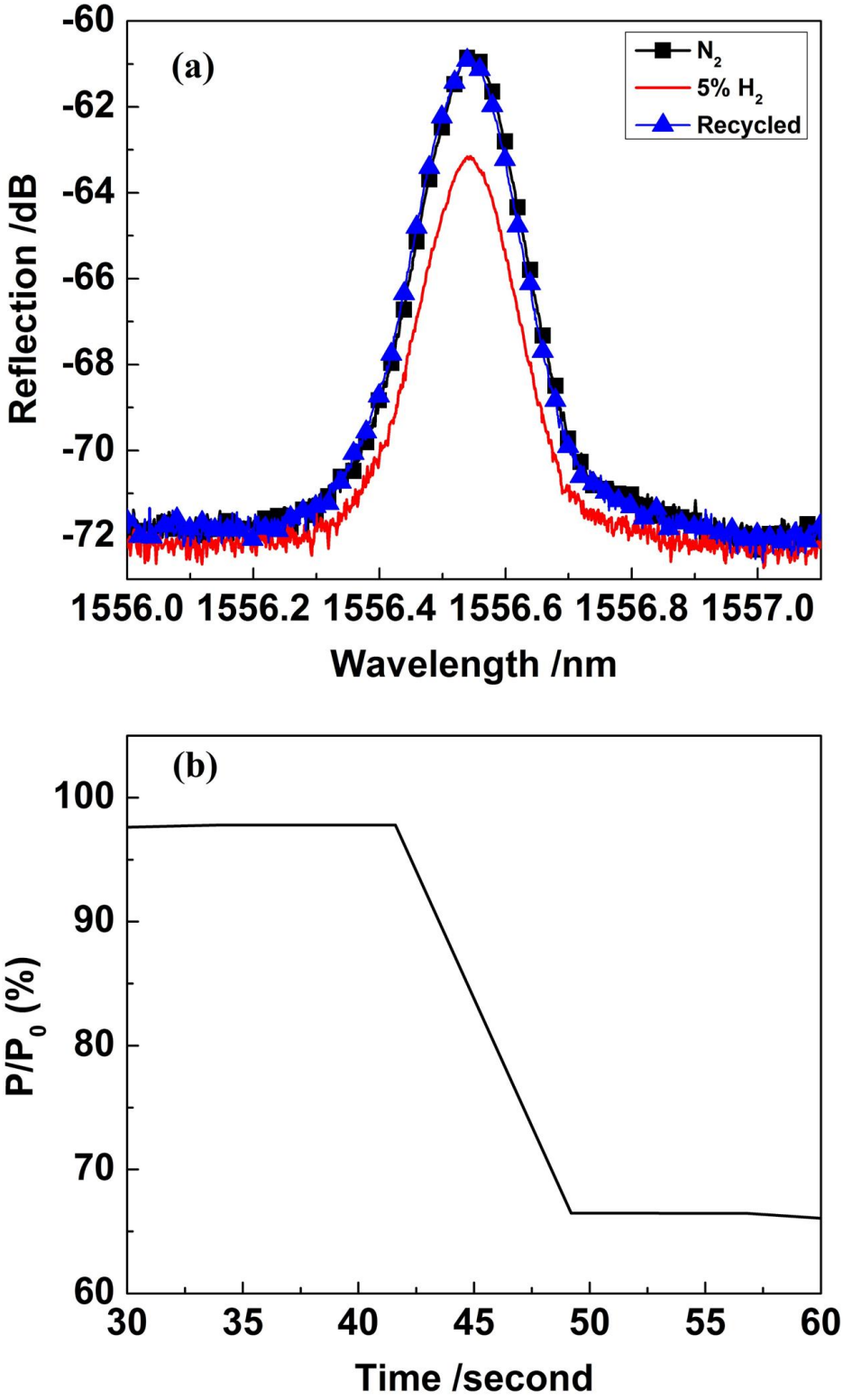

Figure 10. (a) Spectra of the sensor cycled in 5% H_2 and N_2, (b) response time of the hydrogen.

the hydrogen sensor based on nano-porous Pd-TiO_2 coated etched D shaped FBG is reliable at high temperature. Response time is an important sensitivity indicator of a sensor, which is defined as the time required for the sensor to reach its average maximum wavelength shift. In order to measure the response time of the Pd incorporated nano-porous TiO_2, the intensity of the transition was directly measured. The response time of the sensor upon exposure to hydrogen is 7~8 s as figure 10(b) shows. The restore time of the sensor is about several minutes in pure N_2 flush. The restore time is believed to decrease dramatically if small amount of O_2 is added into the N_2.

Figure 11(a) presents the reflection spectra of the FBG exposed to H_2 with concentration range from 0.25% to 5% at the highest testing temperature of 700^{o}C. The decreases of reflected FBG peaks indicate strong optical absorption caused by more effective catalytic dissociation of H_2 in Pd-doped TiO_2 at higher temperatures. The reduction of 6-dB of FBG peak magnitude was measured for the change of hydrogen concentration from 0% to 5%. The reduction of FBG peaks are also accompanied by shift of FBG peaks, which is the indication of refractive index changes of FBG. An 80-pm FBG wavelength shift is noted in Figure 11(a). Given that up to 2% of guided light is propagated in Pd-doped TiO_2 coating, up to 4×10^{-3} refractive index change could be due to the redox reaction of Pd-doped TiO_2 film [14]. However, the FBG peak shifts could also be due to temperature variation. The thermal optic coefficient of FBG in silica fiber is ~13pm/^{o}C. The FBG wavelength shifts shown in Figure 11(a) could be attributed to up to 7^{o}C temperature fluctuation at the elevated temperature of 700^{o}C. Figure 11(b) shows the decrease of the peak intensity upon switching ambient from N_2 to 5 % H_2 in N_2 as a function of temperature. The improvement of the sensor performance at high temperature is considered to be caused by more effective catalytic dissociation of H_2 in Pd-doped TiO_2 at higher temperatures.

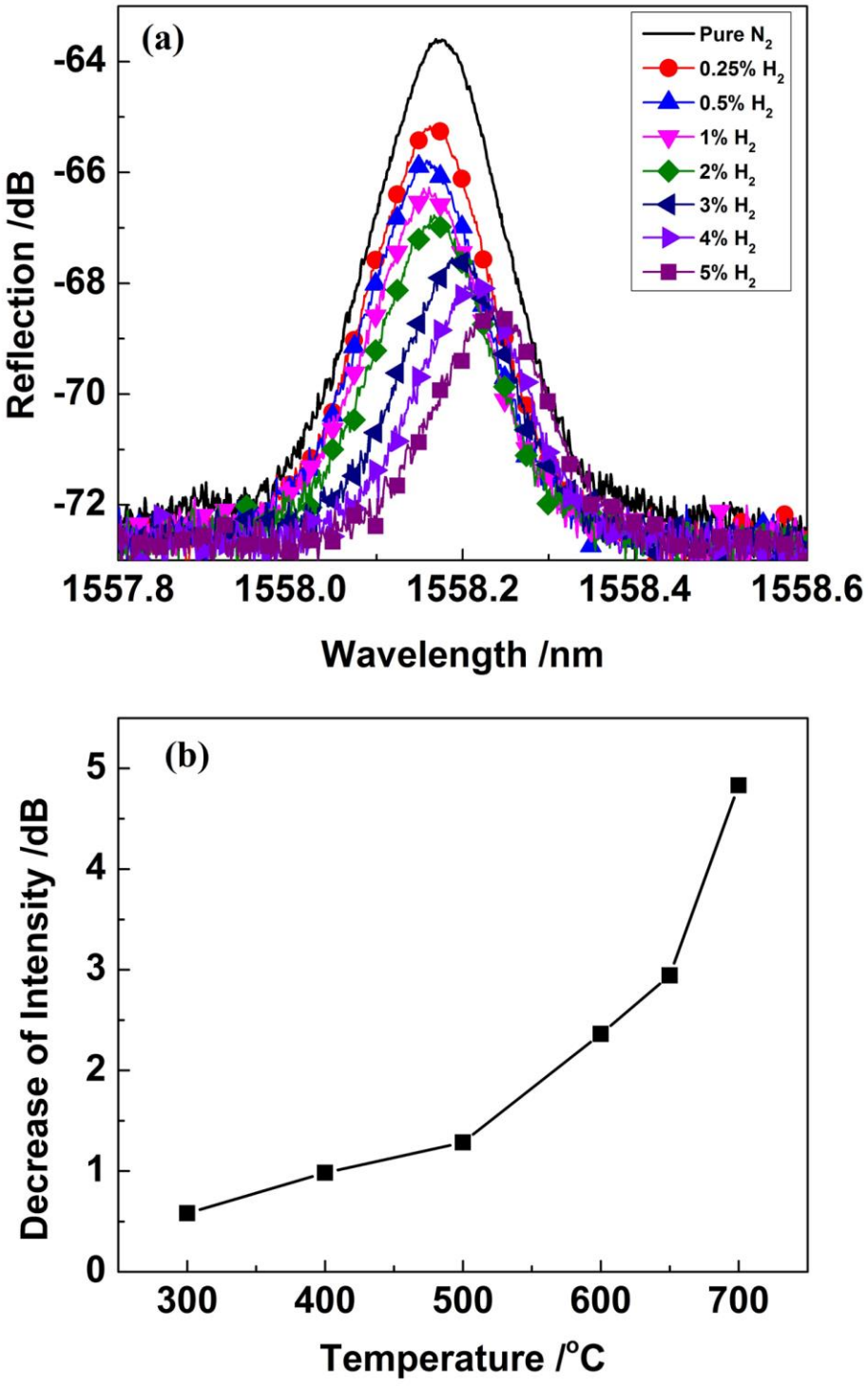

Figure 11. Hydrogen response of the D-shaped fiber senor. (a) Spectrum of the coated D-shaped FBG exposed to 0.25%, 0.5%, 1%, 2%, 3%, 4%, 5% H_2 and pure N_2 respectively, (b) Peak intensity as a function of temperature for 5% H_2.

However, our experiments also show that the performance will degrade when temperature is higher than 780^{o}C, due to thermal stability problem of the porosity structure at this temperature. The porosity structure begins to collapse when temperature is higher than 780^{o}C, which will decrease the surface to volume ratio and increase the refractive index of the film, resulting in large optic loss.

In summary, a solution-based scalable nanofabrication scheme to manufacture metal oxide and their doping variants with controlled index of refraction was presented here. Through block copolymer templating, nanoporous Pd-doped TiO_2 3D nanostructure with pore size from 5 nm to 20 nm was synthesized. Through this approach, the indices of refraction of SiO_2 and TiO_2 can be controlled over a wide range from 1.2 to 2.4. In this paper, this new material synthesis technique has been successfully applied for new optical sensor developments. Using solution-based coating technique, Pd incorporated TiO_2 functional coating were successfully integrated with high-temperature stable fiber Bragg grating in D-shaped fiber for evanescent wave sensing for hydrogen at elevated temperature up to 700^{o}C. Using the same nano-synthesis scheme, it is also possible to manufacturing other metal oxides with desired index such as SnO_2 and ZnO.

3.4 DISTRIBUTED HYDROGEN SENSOR AT HIGH TEMPERATURE

It is of considerable interest to perform distributed chemical gas sensing instead of single point detection. The sensor with capability to sense a wide area with single device would be highly desirable. One example is detection of hydrogen concentration gradient inside of the solid oxide fuel cell channel. When the gas mixture flow through the catalytic surface of the electrolyte, the concentration will change due to the reaction in the cell. As discussed before, another advantage

of fiber sensor is capability of high spatial resolution distributed measurements. Distributed sensor presents the potential to retrace the chemical gradient which is useful to improve the reaction efficiency. Quasi-distributed fiber optical hydrogen sensor with multiplexing several FPI sensors has been reported recently [74]. The hydrogen concentration can be simultaneously monitored with limit by the multiplexing density. Another truly distributed approach is based on in fiber Rayleigh, Brillouin, and Raman scatterings, in which the fiber itself is treated as continuous sensing element. Distributed hydrogen sensing with Pd/Cu coated optical fiber has been reported based on measurement of in-fiber Rayleigh scattering by Optical Frequency Domain Reflectometry (OFDR) [75]. This sensor can provide 1 cm spatial resolution at room temperature. However, many fossil fuel power generation systems (such as fuel cell) require sensors working at high temperature.

In this section, we reported high temperature distributed hydrogen sensing by integration of high-temperature stable metal oxides on optical fibers. By measuring the amplitude of Rayleigh scattering by OFDR system, the hydrogen concentration can be continuously monitored along the fiber. As shown in last section, Pd-doped metal oxides can induce significant optical absorption in near infrared spectra around 1550-nm when exposed to hydrogen gas. The induced absorption can be measured by optical fiber through evanescent wave interactions. Herein D-shaped fibers with Pd-doped metal oxides are further extended for distributed hydrogen sensing. Hydrogen sensing was performed up to 700^{o}C in lab with hydrogen concentration from 0.1% to 10%. The distributed hydrogen sensor was also put into the solid oxide fuel cell(SOFC) chamber to probe the hydrogen gradient at different load current and different initial hydrogen concentration. To further improve the spatial resolution and high-temperature stability, D-fibers with enhanced scattering profile was also used for preliminary test.

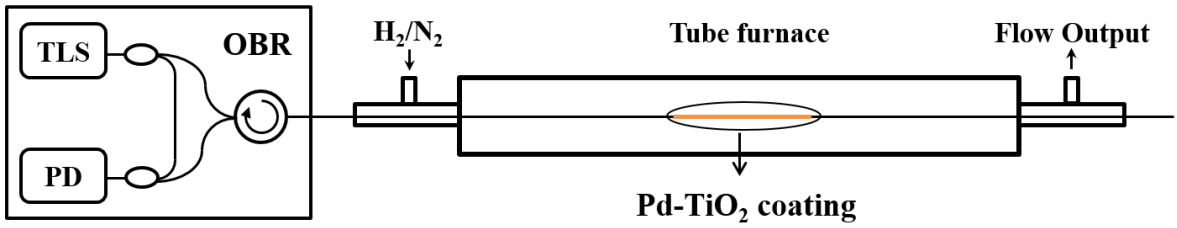

Figure 12. Schematic of distributed fiber optical hydrogen sensing using Rayleigh OFDR scheme.

As shown in figure 12, the experiment schematic is similar to the D-fiber FBG based sensor in the previous section, except that a commercial optical backscatter reflectometer (OBR) system OBR4600 was used to examine the Rayleigh scattering signal. The D-shaped fiber was first etched with 10-cm section in buffered HF solution (5 NH4F:1 HF) to remove the 3-μm cladding material on the flat side. Then the etched section was coated with 3% Pd doped TiO_2 thin film by dip-coating in sol-gel solution. A tube furnace was used provide a controlled high-temperature environment for hydrogen sensing. The coated fiber was then inserted into a quartz tube and sealed using ceramic ferrules. The anneal process is the same as the previous experiment and after that the sensor was heat up to 700^{o}C for testing. Two mass flow controllers were used to pre-mix the nitrogen and hydrogen gas with concentration ranging from 0.1% to 10%. Then the H_2/N_2 gas mixture was fed into the quartz tube at atmosphere pressure.

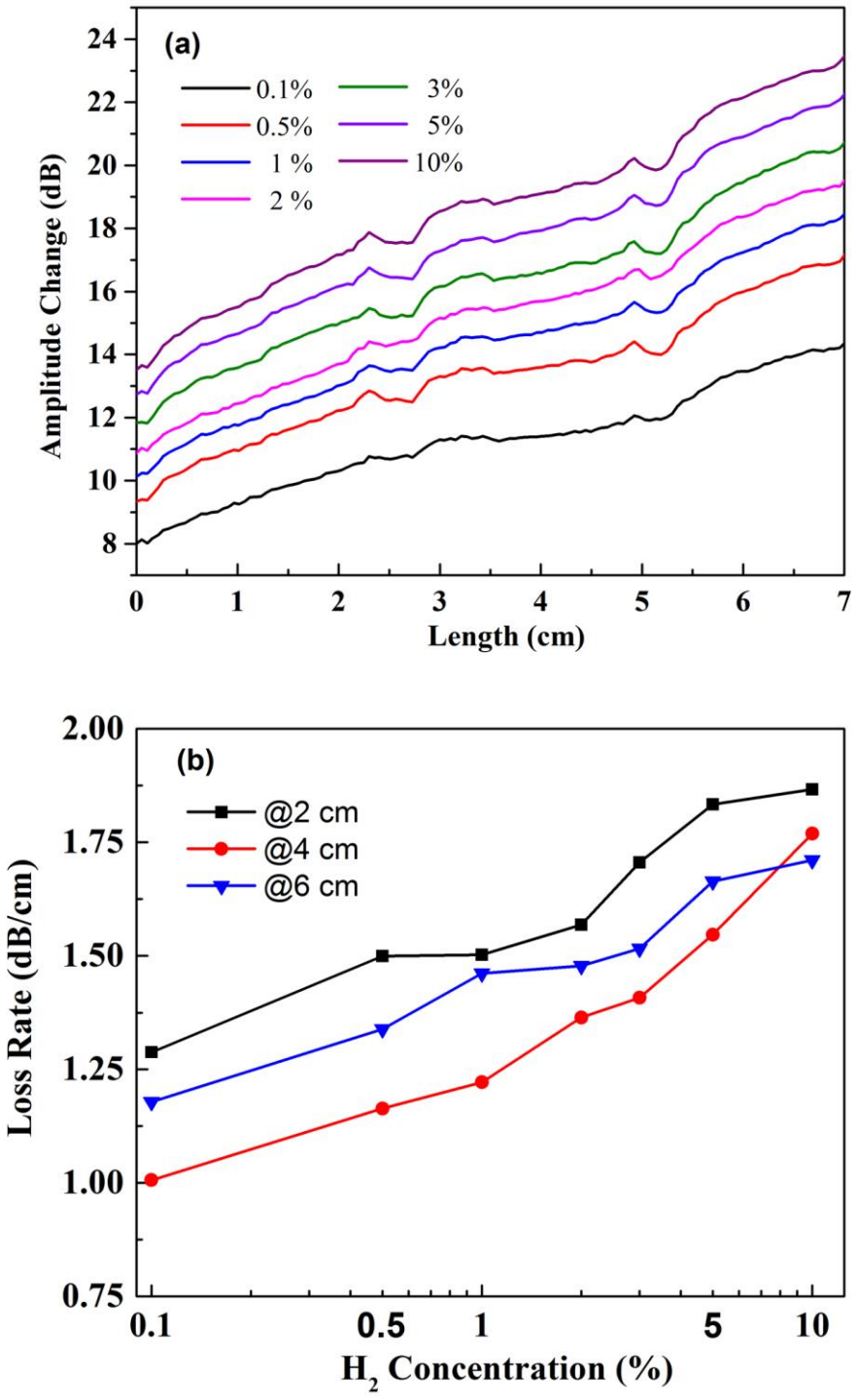

Figure 13. (a) Rayleigh scattering amplitude of Pd-TiO_2 coated D-fiber sensor in various hydrogen concentration at 700ºC; (b) loss rate at 2cm, 4cm and 6cm location.

Figure 13 (a) shows the amplitude change of the Rayleigh scattering signal along a 7-cm section of fiber in different hydrogen concentration. The data in this plot is obtained by using the amplitude of the Rayleigh scattering signal to divide the signal amplitude in various hydrogen concentration. In this measurement, the obtained original data was set to get 0.25mm spatial resolution. Then the signal was smoothed by average of every 40 data points, which corresponding to 1-cm spatial resolution. The fluctuations of the signal along the sensor is considered to be caused by the irregular coating rate. In this data, we can notice that the loss is increasing as the hydrogen concentration increase. When the Pd-TiO_2 is exposed to hydrogen, the free carrier density will increase due to the reduction which will induce light absorption in NIR. As a result, the power transmits in the optical fiber, include both laser source and the Rayleigh scattering signal, will decrease due to the interaction of the evanescent optical field with the Pd-TiO_2 coating. The loss rate of specific location is determined by the local hydrogen concentration if the coating is constant. Thus, by calculating the differential of the Rayleigh scattering signal change, we are able to probe the hydrogen gradient along the fiber sensor. Figure 13(b) show the local loss at 2cm, 4cm and 6 cm respectively.

By using this local loss measurement scheme based on OFDR system, the local hydrogen concentration can be detected at 700^{o}C. Additionally, due to the high-temperature resistance and insulation material of the fiber, it's possible to directly measure the energy reaction at high-temperature reactors such as solid oxide fuel cell system. Figure 14 shows the test result of 100% H_2 in SOFC. The bar in green color is located in the 2 cm to the inlet of the H_2, the red bar is 4 cm away from the inlet, and black bar is 6 cm from the inlet. We can notice the change rate of the backscattering signal is decrease at middle and outlet of the chamber while the current increase, which indicate the concentration at these two points decrease when current increase.

Although the green bar (close to the inlet) also changed, the value is still close to the value when current is 0 A, which indicate the concentration of H_2 around the inlet doesn't change too much.

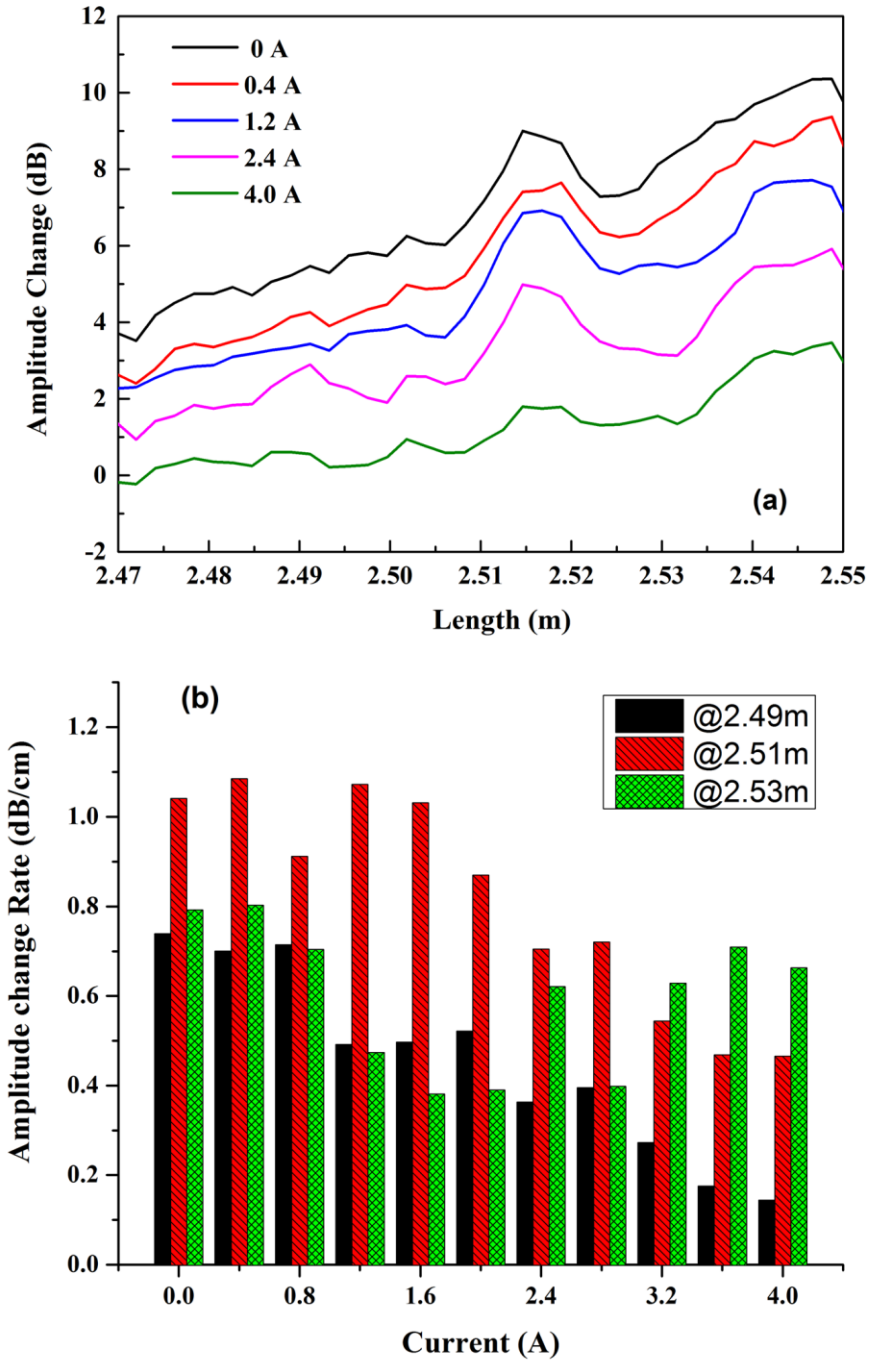

Figure 14. Distributed hydrogen sensing in 100% H_2 in SOFC at different operation current.

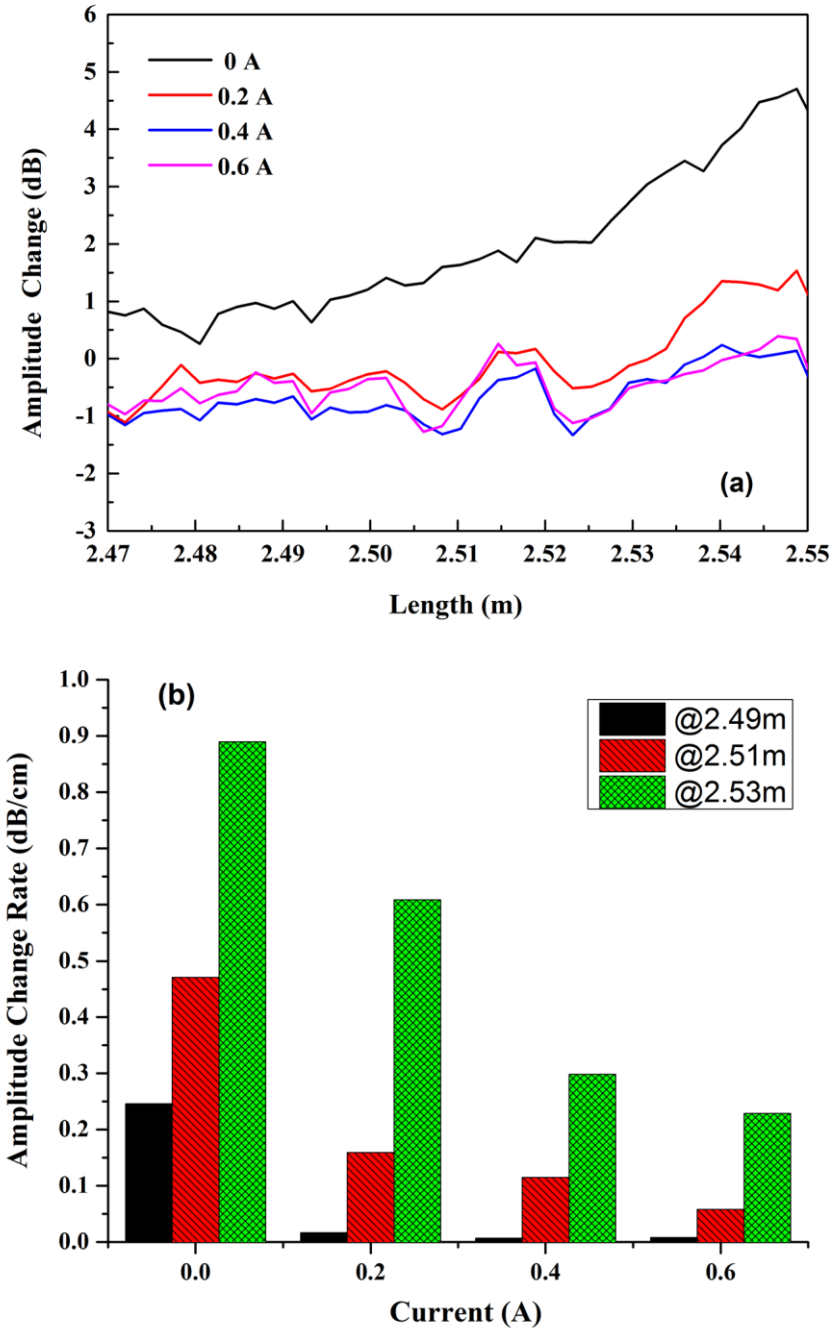

Figure 15. Distributed hydrogen sensing in 4% H_2 in SOFC at different operation current.

For 4% H_2 test shown in figure 15, the concentration of the H_2 at the outlet(Black) is lower than the inlet even there is no current. One possible reason is that the H_2 will be consumed even there is no current. For the result with current, we can notice the concentration at the outlet is always close to 0 for 4% H_2 feed. The H_2 concentration at inlet and middle keep decreasing when the current increase.

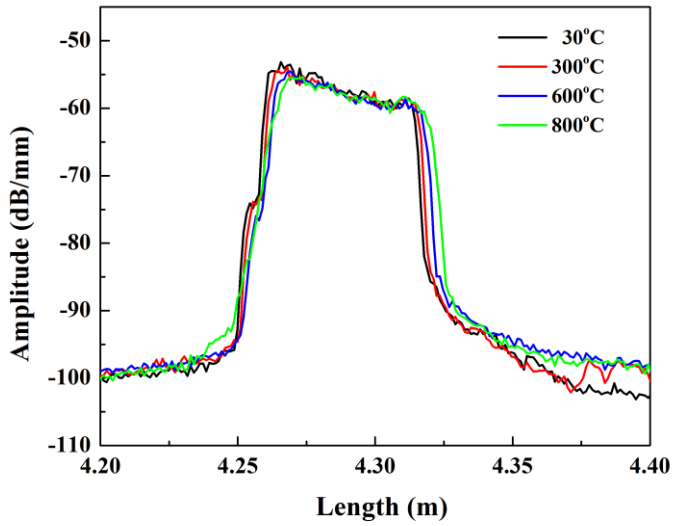

Figure 16. Rayleigh backscattering features enhanced by the ultrafast laser annealed at 30°C, 300°C, 600°C, and 800°C, respectively.

From the test results, we could notice that the sensitivity, detection distance and spatial resolution of the distributed sensing with standard core fiber are limited due to the weak signal of the in-fiber scattering. To further explore the potential of distributed chemical gas sensing using optical fiber, we demonstrated the sensing schemes to probe energy chemistry with high spatial resolution by using the fiber with enhanced scattering signal. Since the sensing scheme is based on the measurement of distributed loss caused by evanescent wave interaction along the fiber, the increased amplitude of the scattering gives larger dynamic range resulting in longer detection

length. Another advantage of the sensor is the thermal stability for high temperature operation. As shown in figure 16, the backscattering signals at different temperature were plotted. The result shows no significant changes of the amplitude working in high temperature up to 800^{o}C. After ultrafast laser processing, the fiber was etched using HF solution for 7 minutes to remove part of the cladding, which could enhance the evanescent-wave. The etching rate of the fiber after ultrafast laser irradiation is faster than the regular fiber, so the etching time will be shorter here. By using a Rayleigh Optical Frequency Domain Reflectometry (R-OFDR) to perform the hydrogen-induced distributed fiber loss, we could measure the hydrogen concentration along the fiber. Figure 17(a) and (b) shows the preliminary result of the distributed hydrogen sensing at 600^{o}C and 750^{o}C. The length of the enhanced region is 7 cm. Due to the 40 ~ 45 dB increase in back scattering return signal and smooth coating on the fiber, the amplitude is linear decrease along the fiber in the sensing region. The slope will increase while the H_2 concentration increase, which indicated that the loss of the fiber in unit length increases. The H_2 concentration can be obtained by calculating the local slope at a specific spot with 1-mm spatial resolution.

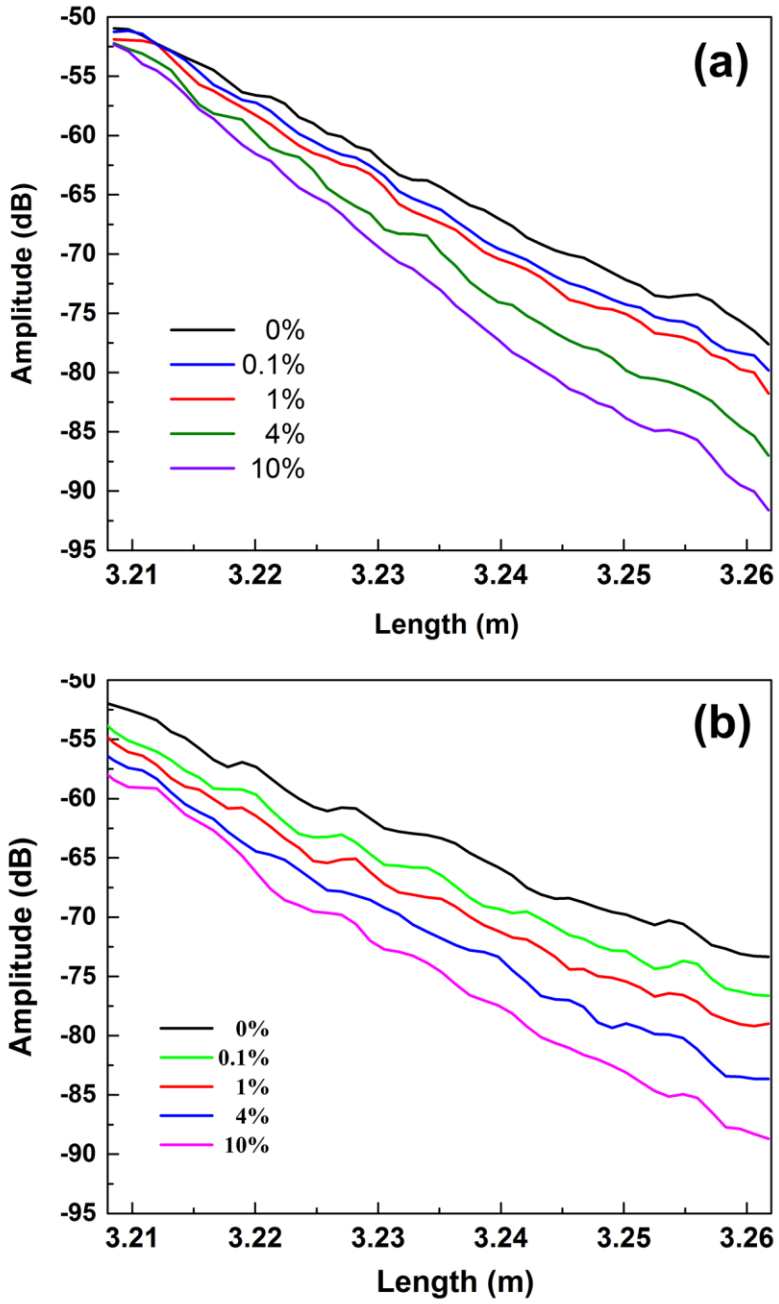

Figure 17. Distributed hydrogen measurement with enhanced Rayleigh backscattering features on D-shaped fiber at (a) 600ºC and (b) 750ºC.

3.5 FIBER OPTICAL METHANE SENSOR

Methane, as the main component of natural gas, is considered to be cleaner than other fossil fuel and is widely used in industry and home supply. To support safe utilization of natural gas, a large number of methane sensor has been developed, especially the conductometric sensors based on metal oxides [76, 77]. Besides using as conductometric sensor, the metal oxides are excellent candidates for fiber optic sensors[14]. Additionally, the fiber optic sensor can take full advantage of robust performance in harsh environments.

In this work, we reported evanescent wave based fiber optical CH_4 sensor at high temperature operation. D-shaped fiber, an optimized platform for sensing applications, was used as the sensor platform. A templated based sol-gel manufacturing approach was employed to produce Pd-doped nano-porous SnO_2. By coating the fiber with nanostructured Pd-doped SnO_2 functional sensing material, we demonstrated CH_4 sensor with good sensitivity and stability, which has been successfully measure CH_4 concentration range from 1% to 50%.

In order to improve the sensitivity of the fiber optic sensor, one feasible way is increasing the interaction length between the light and coating materials [14]. However, one of the critical challenges of integrating Pd-doped SnO_2 sensory film on silica fibers is the mismatch of refractive index of metal oxide ($n>2$) and that of silica fiber ($n\sim1.468$). The guiding light can't be maintained with thick or lengthy high index metal oxide coating as the fiber cladding. To address this issue, a sol-gel chemistry approach combined with block copolymer template was used to produce nanostructured Pd-doped SnO_2, which can enhance the evanescent wave interactions by tailoring the refractive index and porosity[14]. In this work, Pluronic F-127 block copolymer template is used due to its higher temperature stability, which ensures to keep the nano-structure since it'll be removed after the crystallization of the inorganic framework is completed. The sol-

gel solution was obtained by mixing of 1.37 g $SnCl_4$, 1g HCl, 6.26g Ethanol, 0.75g Pluronic F-127 and 0.028 $PdCl_2$ (ACS Reagent, Sigma Aldrich). The solution was stirring for 1 hour at 60°C on the hot plate to obtain a homogeneous solution. Afterwards the solution was cooled to room temperature and aged for 24 hours.

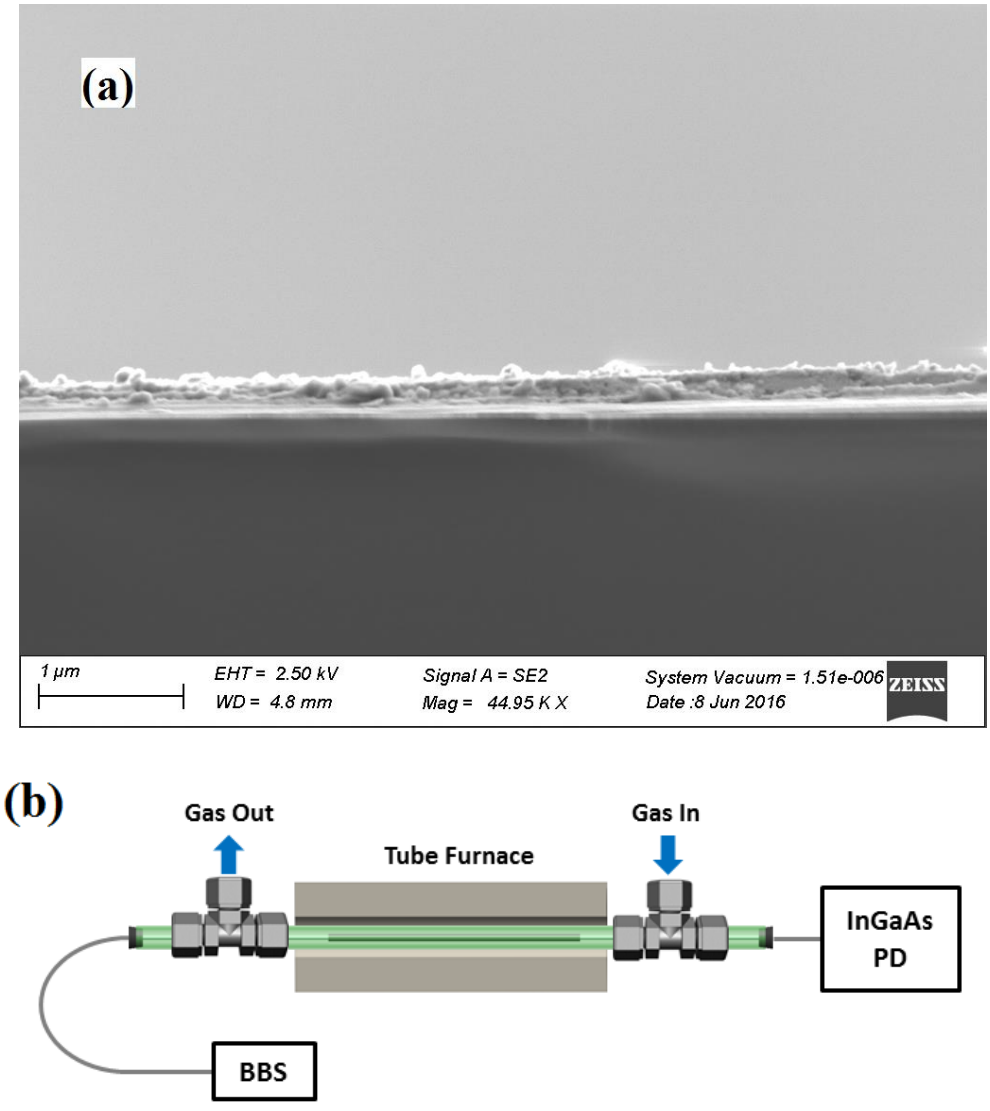

Figure 18. Methane gas sensor based on D-shaped fiber. (a) cross sectional SEM image of the constructed sensor with Pd-doped SnO_2 thin film; (b) schematic of D-shaped fiber CH_4 gas sensing setup.

In order to get a higher sensitivity, the residual cladding material on the flat side of the D-shaped fiber was removed by placing it in a buffered HF solution (5 NH_4F : 1 HF) for 18 minutes. Then it was immersed in the sol gel solution and coated through dip coating procedure with a coating length of 15cm. The coated fiber was dried in the air at room temperature overnight for hydrolysis. Then the coated fiber was calcined in a programmable tube furnace in air at 600^oC for 1 hour. Then it was cooled down to 500^oC for methane detection. Figure 18(a) shows the SEM picture of the cross section of the D-shaped fiber coated with Pd doped SnO_2. The interconnected porous structure formed by the use of block copolymer Pluronic F-127 is clearly visible. The thickness of the coating is about 300nm.

The schematic sketch of fiber optic CH_4 sensing experiment setup is shown in Figure 18(b). The fiber was inserted in a quartz tube with two ends sealed, and placed in tube furnace. The rubber ferrules used for sealing also applied tension to ensure that the fiber has no contact to the inner wall of the tube. The sensor can be exposed to various concentrations of methane gas balanced with N_2 using two calibrated mass flow controllers. In measuring the sensory response, light from broadband light source (EBS-7210 Er^{3+} Broadband, MPB Technologies) was coupled into the D-shaped fiber and power transmission through the fiber was monitored with an InGaAs photo detector in the other end.

The SnO_2 exhibits strong optical absorption in the presence of CH_4 due to the removal of chemisorbed oxygen concentration on the surface [76, 78]. Thereby releasing the trapped electrons and resulting in an increasing optical absorption of NIR light in the sensory film. When doping with Pd, the catalytic behavior of Pd will enhance the reaction between CH_4 and the adsorbed oxygen [76, 77]. To study the sensor response to hydrogen, the gas flow from two cylinders containing compressed nitrogen and methane were mixed with different volume ratio

between 0% and 50%. The flow rate of the mixture gas was kept a constant to 40 SCCM during the whole experiment. The repeatability of the sensor was first test by cycling between 0% and 25% CH_4 atmosphere at 500^oC. Each cycle contains 10 minutes of 25% CH_4 followed by 15 minutes pure N_2 flow. Figure 19(a) shows the transmission output of the sensor. The transmission loss in 25% CH_4 is 8.5% and the response time is about 1 minitues. The base line drift less than 0.5% which means the sensor has good repeatability. The dynamic response of the sensor for 5%, 10%, 25% and 50% methane were shown in the inset of figure 19(b). The obtained data form of optical loss vs. the concentration of CH_4 are plotted in figure 19(b).

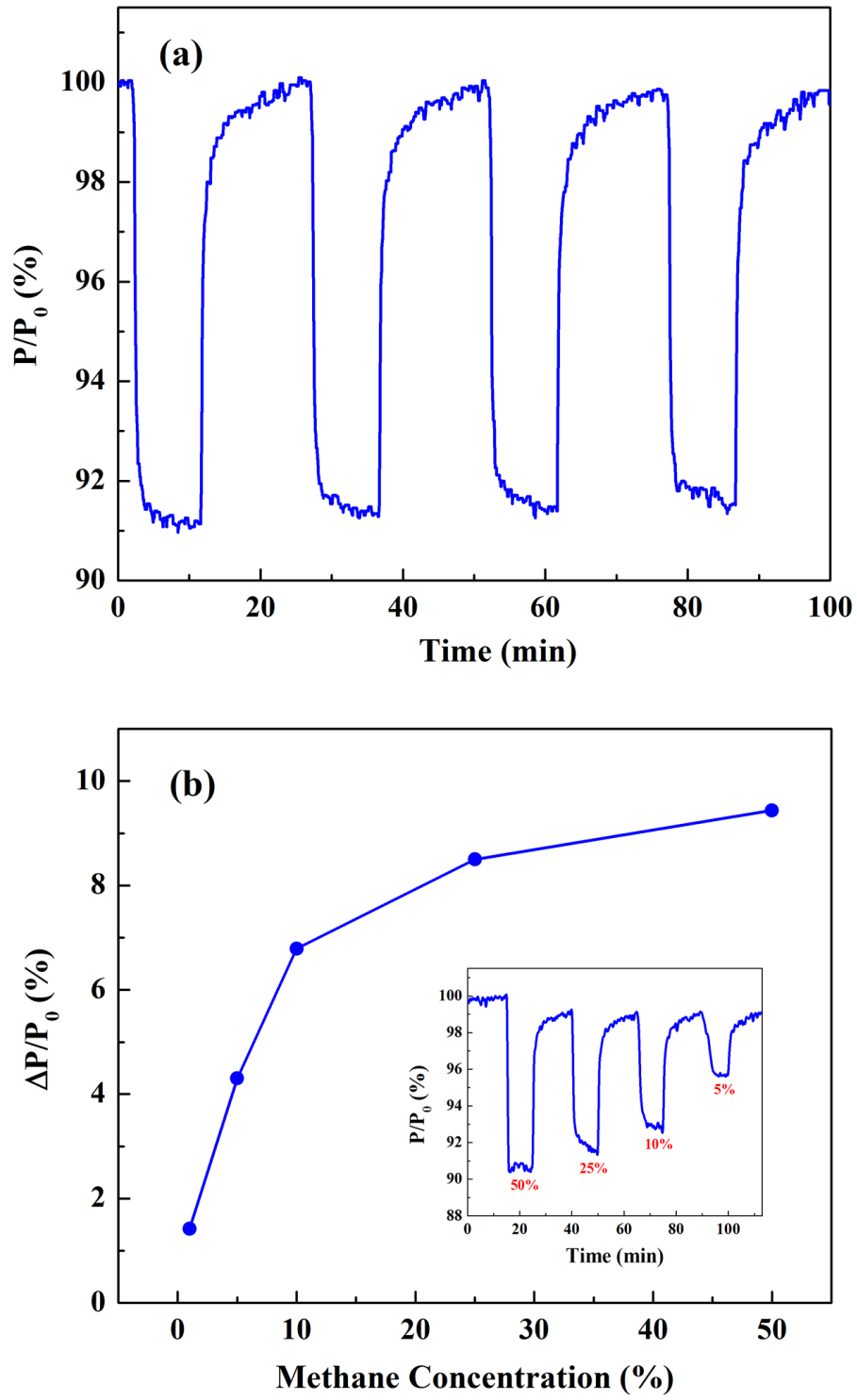

Figure 19. (a) Repeatability of the sensor output for 25% CH_4 in N_2; (b) sensor response for CH_4 concentration varying from 0% to 50% at 500ºC.

4.0 SAPPHIRE FIBER OPTICAL HYDROGEN SENSORS FOR HIGH TEMPERATURE ENVIRONMENTS

4.1 BACKGROUND

In order to overcome the operation temperature limit of the silica fiber based gas sensing platform, a single-crystal sapphire fiber was used for test. The fiber sensor platform used in this work is single-crystal sapphire fiber with 100-μm diameter (Micromaterials Inc) with refractive index of 1.74 at 1550 nm. In comparison with the fibers used in previously reported optical fiber hydrogen sensor, single crystal sapphire fiber has extreme high melting point above 2000^{o}C, superior mechanical properties especially at high temperatures, stable chemical properties resistant to corrosion, hydrogen ingress, and hydrogen-induced optical property changes at high temperatures. It is well suited for ultra-high temperature sensing applications [36, 79, 80]. Here we demonstrate a single crystal sapphire fiber coated with nanostructured Pd doped TiO_2 thin film for hydrogen sensing rated at 800^{o}C by taking advantage of the excellent high temperature performance of single-crystal sapphire fiber and TiO_2.

4.2 MATERIAL AND METHOD

One of the critical challenges of integrating Pd-TiO_2 sensory films on sapphire fibers is the mismatch of refractive indices of the metal oxide (n~2.4) and that of sapphire fiber (n~1.74). The high index coating of metal oxide does not satisfy the guiding properties and can result in dramatically reduced light transmission for sufficiently thick layers [81]. To address this challenge, a block-copolymer template scheme was used to produce nano-porous Pd-TiO_2 film with appropriate porosity to lower its refractive index using a sol-gel synthesis scheme [81]. By controlling the mole fraction of the copolymer with respect to the metal source, we were able to tune the refractive index of the resulting metal oxide thin films. In this works, TiO_2 precursor solution was synthesized by adding 1.5 g $Ti(OCH(CH_3)_2)_4$ and 0.45 g HCl into 6 g ethanol and stirred for 10 minutes. 1 g $PdCl_2$ ethanol solution (2.7%) was subsequently added into the solution as Pd source (corresponding to 3 at.% of Ti). 0.8 g Pluronic F-127 block co-polymer was added as the structure template for the 3D nano-engineering of metal oxides in the sub-wavelength regime. The mixture was stirred for 12 hours at 60^oC to obtain a homogeneous solution. Afterwards the solution was cooled down to room temperature and aged for 24 hours.

The index-temperature relationship is crucial in evanescent wave based fiber high temperature gas sensors. The annealing temperature can have a substantial influence on the resultant refractive index due to densification, resulting in a porosity reduction. Prior to hydrogen exposure, the effect of the annealing temperature on the refractive index was examined. In order to characterize the refractive indices of nanoporous Pd-TiO_2 calcination at different temperatures, the Pd-TiO_2 thin films were produced on silicon substrates by spin coating. The spun-on films were then calcined at 500^oC, 600^oC, 700^oC and 800^oC for 2 hours, respectively. A Jobin-Yvon UVISEL Spectroscopic Ellipsometer was used to characterize the refractive index of

the samples. Figure 20 shows results of refractive indices of the prepared sol-gel derived nanostructured Pd-TiO_2 at different temperatures. The refractive index of single-crystal sapphire around 1.74 is also shown in this figure for reference. The V-number for 100 μm of this multi-mode sapphire fiber is 288, which support over 40,000 modes. The results indicate that the refractive index of the film increases as the calcination temperature increases but it is still below the refractive index of sapphire even for samples calcined at temperatures as high 800^{o}C.

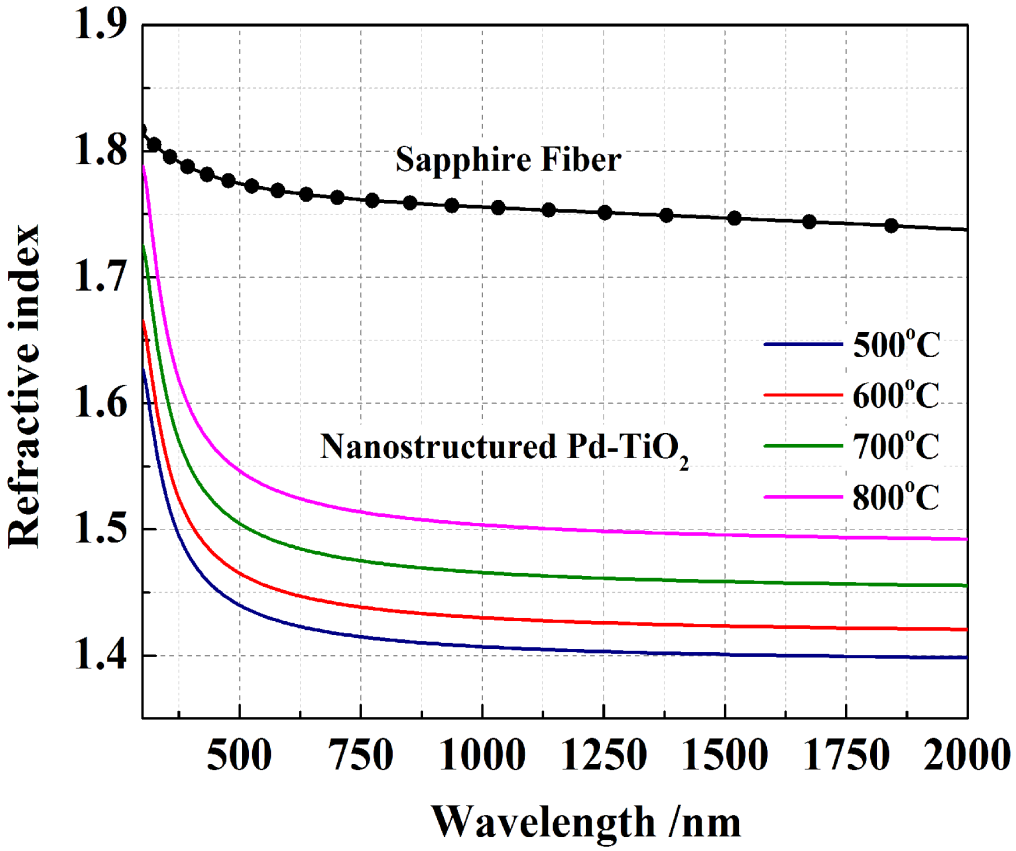

Figure 20. Refractive indices of nanoporous Pd-TiO_2 film calcined at different temperatures.

An experiment setup shown in figure 21(a) was used to study the hydrogen response of the sapphire fiber chemical sensors. A tube furnace was used to provide high temperature environments for the sol gel annealing process and also for hydrogen tests. The fiber was immersed in the precursor solution and coated through a dip coating procedure. The coated length is 10 cm. The coated fiber was dried in the air at room temperature for at least 12 hours. The coated fiber was then inserted into a quartz tube gas cell. Two rubber ferules were used to seal both ends of the tube. They also apply a slight tension to ensure that the fiber does not contact the inner wall of the quartz tube. An amplified spontaneous emission broadband light source (MPB EBS-7210), with a span of 1515nm to 1615nm, was butt-coupled into the sapphire fiber sensor for the sensing testing. At the other end of the fiber, the transmitted optical power was measured by an InGaAs photo detector. With the tubing connected to the gas cell, the sensor can be exposed to various concentrations of H_2 balanced with either N_2 or air using two calibrated mass flow controllers.

The coated film was first annealed at 130^{o}C for one hour for pre-heat treatment. This is followed by heating to 600C with a rate of 3 ^{o}C/min. The coated sapphire fiber was held at this temperature for one hour for the calcination process. These procedures were conducted in air atmosphere. Once the calcination process was completed, the coated fiber was cooled to 300 ^{o}C at 3 ^{o}C/min at which time the air atmosphere was replaced with 5 vol. % H_2/N_2 for 1 hour with a flow of 50 SCCM to reduce the PdO in the TiO_2 film to Pd nanoparticles [82].

The Pd-TiO_2 film on the sapphire fiber was first studied by a Tecnai F20 transmission electron microscope (TEM) operating at 200kV. Focused ion beam (FIB) lift-off procedure was used to prepare cross-sectional TEM samples of the coated sapphire sample. The TEM image in figure 21(b) shows the interconnected 3D structure formed by the use of block copolymer. The TiO_2

grain size is about 50~100 nm and the Pd nanoparticles are roughly 20nm in diameter. A High-resolution TEM (HRTEM) image of TiO_2 layer is shown in figure 21(c). TiO_2 in anatase phase could be indexed from the image with a fast Fourier transform (FFT) analysis, which is included as an inset of figure 21(c). HRTEM diffraction patterns of the Pd nanoparticles could be indexed to the FCC Pd phase. Prior work has also shown that moderate temperature reducing atmosphere treatments can reduce oxidized Pd-based nanoparticles to metallic Pd [82].

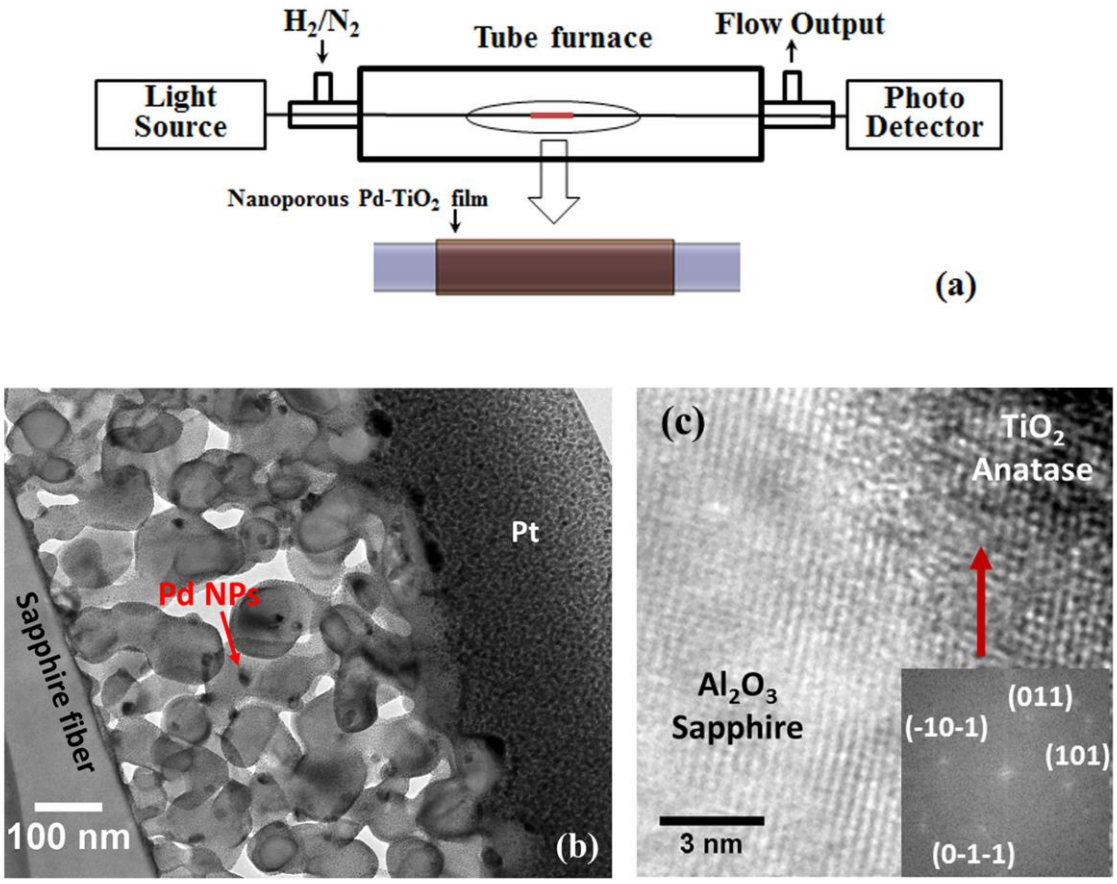

Figure 21. Characterization of Pd-TiO_2 coated on sapphire fiber. (a) Experiment setup for investigating the hydrogen response of the sapphire fiber based sensor, (b) cross-sectional TEM image of the Pd-TiO_2 film coated on sapphire fiber (protective Pt overlayer is deposited before and during FIB sample preparation), (c) high-resolution TEM image obtained at the interface.

4.3 HYDROGEN SENSING CHARACTERIZATION

To study the sensor response to hydrogen, the gas flow from two cylinders containing compressed nitrogen and 10% hydrogen (balanced in nitrogen) were mixed with different volume ratio between 0% and 4% hydrogen. The total flow rate was kept at 50 SCCM. In order to test the repeatability of the sapphire fiber sensor, the sensor was first cycled between 4% hydrogen and 0% hydrogen (pure nitrogen) atmosphere at 800^{o}C. Each cycle contains 10 minutes of 4% H_2 followed by 15 minutes pure N_2 flow. The transmission output of the sensor is shown in figure 21(a). The transmission optical loss of 23% can be observed when exposure to 4% H_2. The optical transmission baseline drifts at 0% and 4% hydrogen was less than 0.5% as shown in figure 22(a). Figure 22(b) shows a typical sensor response to exposure to different hydrogen concentrations from 0.05% to 4%. At low hydrogen concentration of 0.05% a transmission loss of 7.5% can be clearly resolved.

The strong optical absorption observed in the sensor in the presence of hydrogen-containing atmosphere is likely caused by removal of the chemisorbed oxygen concentration on the TiO_2 surface in reducing gas exposure [83]. On removal of chemisorbed oxygen, the free electron concentration will increase and result in increasing optical absorption of NIR light in the sensory film. When doped with palladium, hydrogen adsorbed on palladium simultaneously spill over the surface of TiO_2, enhancing the reaction between hydrogen and the adsorbed oxygen [25, 83], which significantly improves selectivity and sensitivity of the sensor.

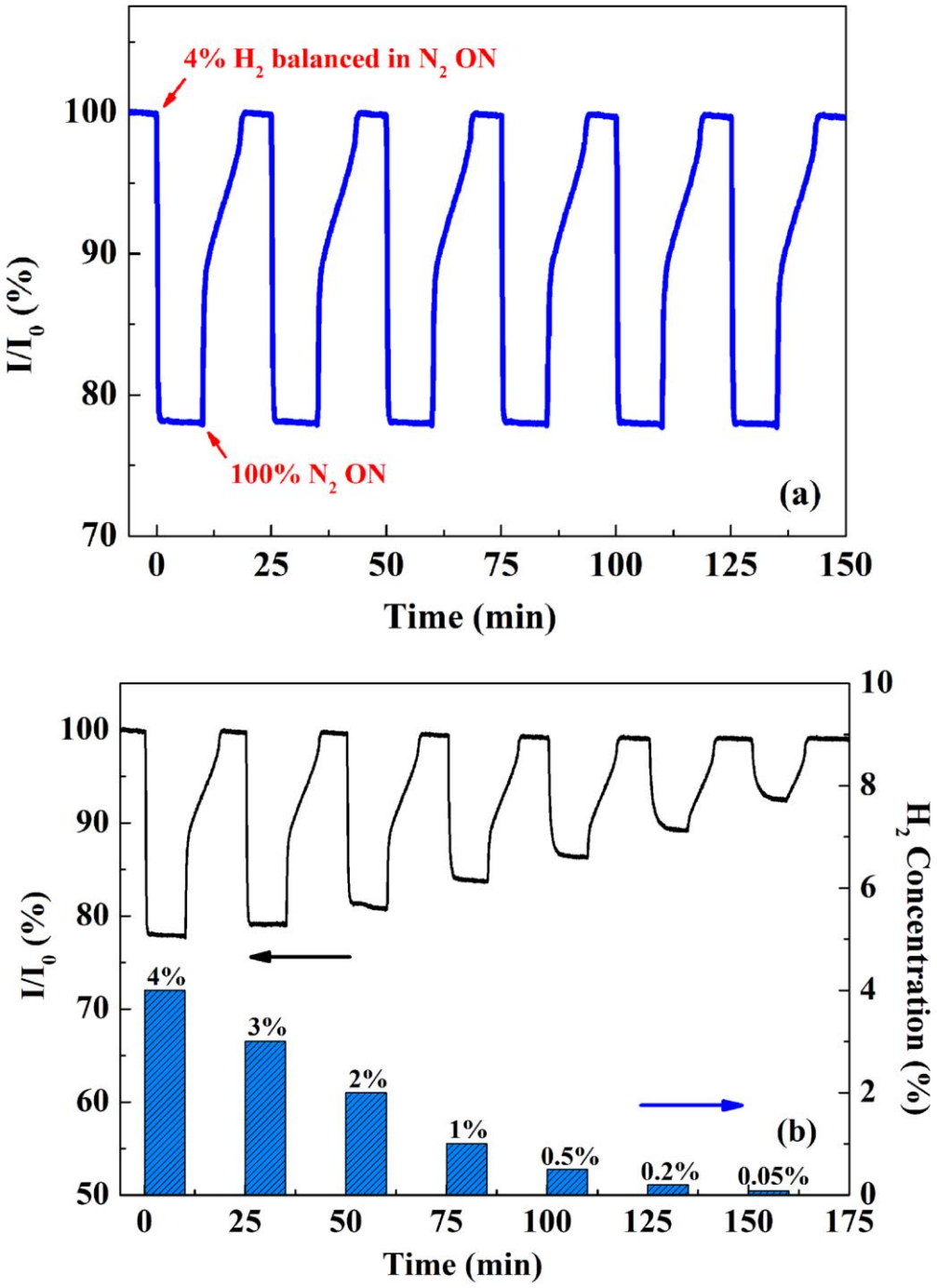

Figure 22. (a) Repeatability of the sensor output for 4% hydrogen; (b) typical sensory response for different concentrations of hydrogen at 800°C.

Stability of the sensory responses was tested by keeping the sensor operation in high temperature environment for three weeks. Table I lists the sensory response at 800°C for different concentrations of H_2 during this period. During the first week, small increases of optical transmission loss were observed. The sensor was first prepared by calcination at 600°C before the test, so when we increased the temperature to 800°C, changes in nanostructure of the Pd-TiO_2 film are expected, which might be the cause of these changes [84]. After the sensor was aging at 800°C for several days, the sensor tended to be stable. The variations observed in the subsequent weeks are quite small, generally less than 0.28%.

Table 1. Optical transmission loss of the sensor at 800°C

H_2 (%)	4	2	1	0.5	0.1	0.05
1st week	21.27%	18.52%	16.00%	13.48%	8.04%	5.78%
2nd week	23.45%	20.38%	17.66%	15.21%	10.12%	7.75%
3rd week	23.39%	20.18%	17.38%	15.02%	10.06%	7.83%

In addition, a response time analysis was performed. Here we define the response time as the time from flushing with hydrogen to the transmission power reaching 90% of the total loss of hydrogen stable value. The sensor recovery time is from flushing with pure nitrogen to 90% of total loss recovered. The response time of the sensor at 800°C for various hydrogen concentrations was illustrated in figure 23(a). With an increase in the hydrogen concentration, the response time decreased while the recovery time increased, and both response time and recovery time trend to saturated values. For 4% H_2, the response and recovery time are 14.5s and 8 minutes, respectively. The response time for 4% H_2 at 14.5s is comparable with other hydrogen sensors that can only function at lower temperatures.[85] However, the recovery time can be dramatically shortened in present of O_2, which is common for most of the practical

situations[24]. As shown in figure 23(b), the recovery time is only 45 s when 1% O_2 was introduced to the N_2 background, which is significantly accelerated.

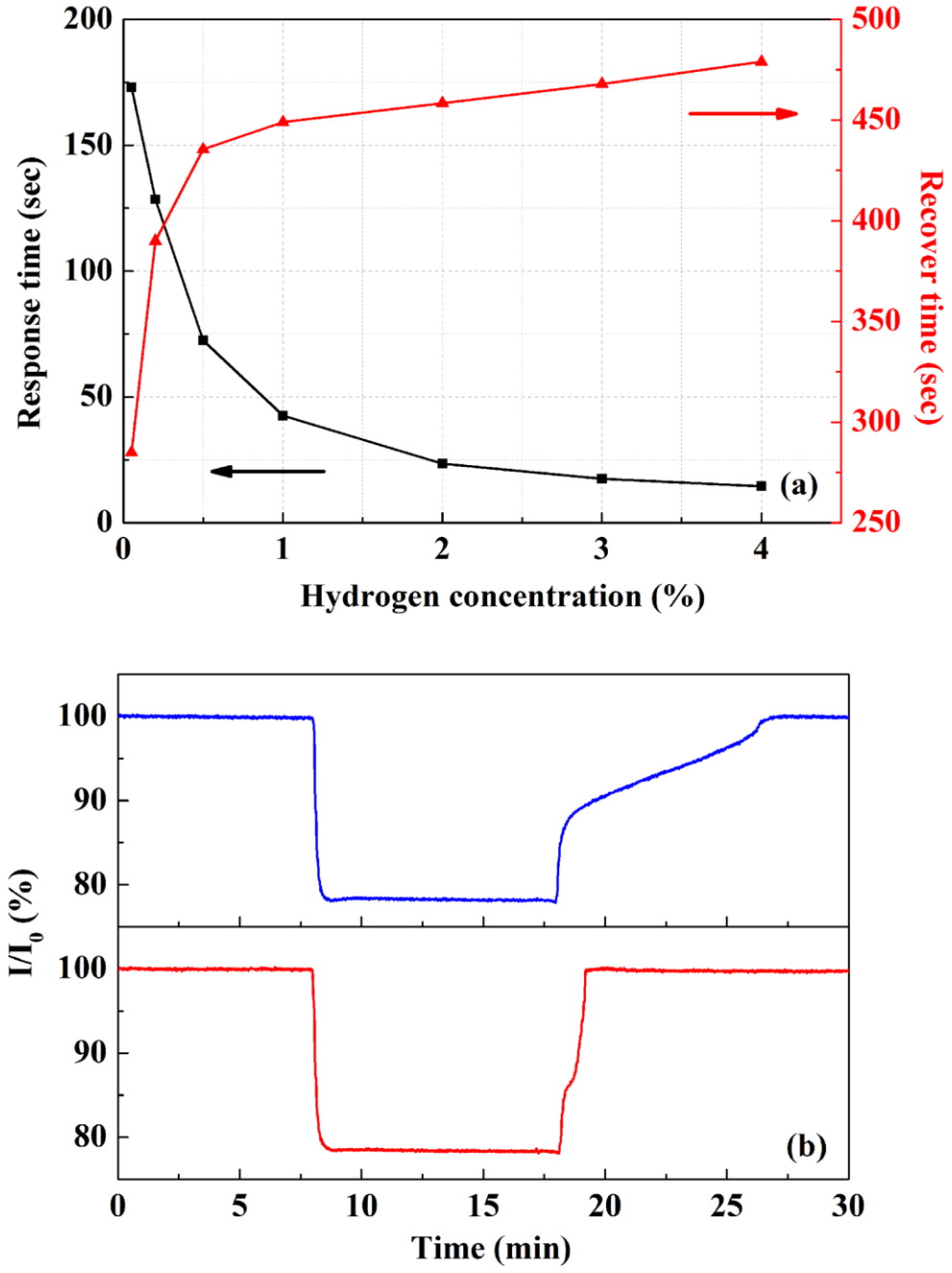

Figure 23. (a) Response time and recovery time for different concentration of hydrogen; (b) comparison of the recovery time in pure N_2 and in present of O_2.

The performance of sensory response was further studied by exposing to various H_2 concentrations at different temperatures. The concentration of the H_2 ranging from 0% to 4% was introduced into the testing chamber incrementally every 20 minutes. Figure 24(a) shows the normalized transmission of the sensor at 700^{o}C and 800^{o}C, respectively. The lowest hydrogen concentration under the test was 0.02% due to instrumentation limitations. The transmission power output increased as the concentration decreased. More importantly, the sensitivity of fiber sensors also increases significantly with the temperatures. Figure 24(b) shows the sensitivity of the sensor for various hydrogen concentrations from 600^{o}C to 800^{o}C with 50^{o}C interval. The improvement of the sensor performance at higher temperature may be due to more effective catalytic dissociation of H_2 in Pd-TiO_2 at higher temperatures [86]. An increased electronic conductivity and hence free carrier absorption resulting in stronger optical gas sensing response at higher temperatures may also be playing a role [24].

In summary, we demonstrated an optical hydrogen sensor based on single crystal sapphire fiber coated with Pd nanoparticles incorporated TiO_2 sensory film. The refractive indices of thin film are controlled by the method of triblock copolymer templating. The sensor is stable and repeatable for ultra-high temperature operation up to 800^{o}C. The results presented in this paper show that the sensor can reliably measure H_2 concentration from 0.02% to 4% with favorable time response. Additional study shows that the sensor performance improves at higher temperature.

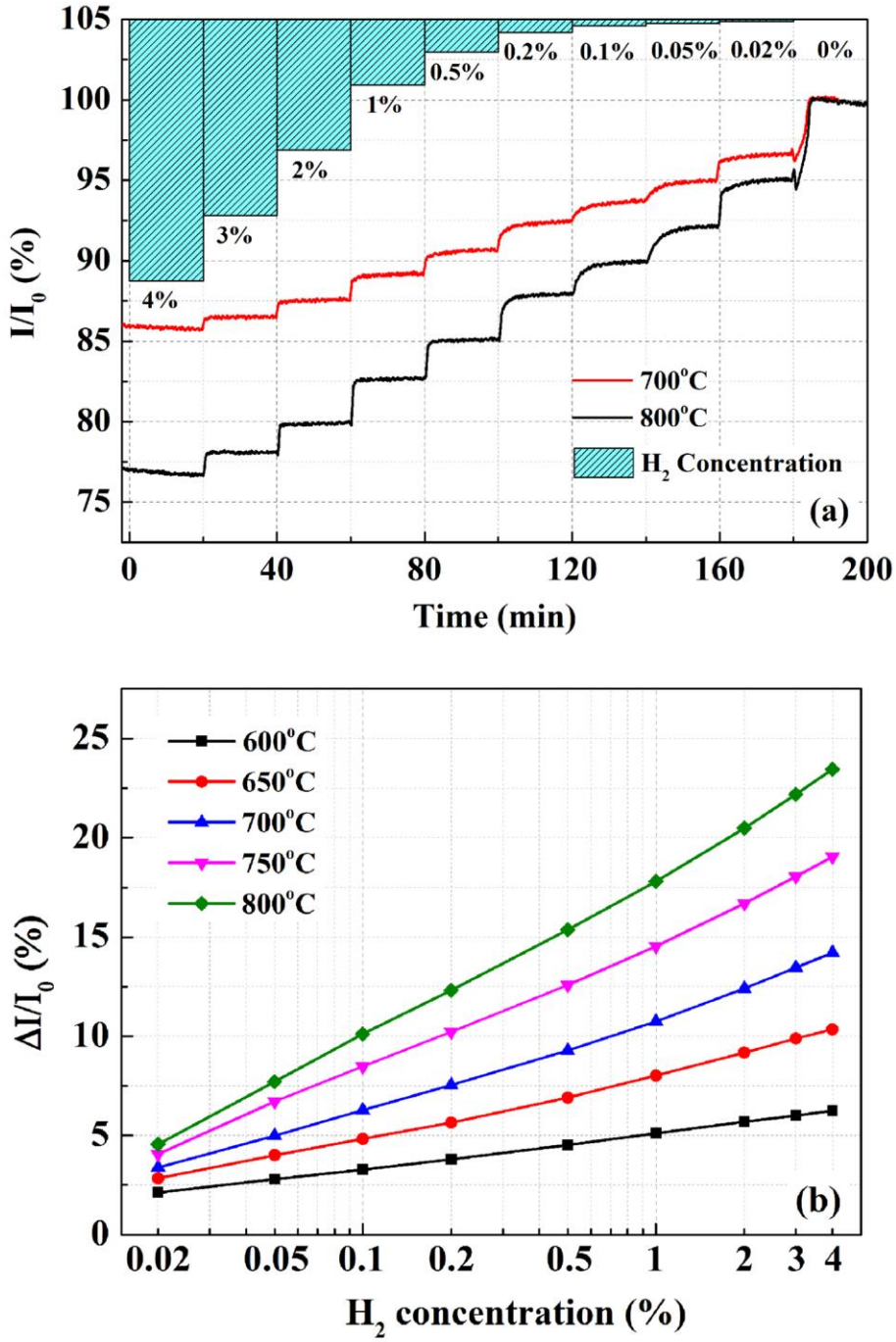

Figure 24. Sensory response with variant temperature and hydrogen concentrations. (a) Comparison of sensory output for varying concentrations of hydrogen at 700°C and 800°C, (b) sensitivity of the sensor for varying concentrations of hydrogen evaluated at different temperature.

5.0 DISTRIBUTED OPTICAL FIBER SENSORS WITH ULTRAFAST LASER ENHANCED RAYLEIGH BACKSCATTERING

We demonstrated a technique to enhance the magnitude and high-temperature stability of Rayleigh back-scattering signals in silica fibers for distributed sensing applications. With femtosecond laser radiation, more than 40-dB enhancement of Rayleigh backscattering signal was generated in silica fibers using 300-nJ laser pulses at 250 kHz repetition rate. The laser-induced Rayleigh scattering defects were found to be stable from the room temperature to 800^{o}C even in hydrogen gas. The Rayleigh scatter at high temperatures was correlated to the formation and modification of nanogratings in the fiber core. The morphology of the nanograting was studied at different laser scanning speed. Optimum irradiation conditions were used to process the fiber with lower insertion loss. Study of the thermal stability of the inscribed nanogratings shows decrease slightly in the polarization at high temperature and the enhancement of the scattering is rendered truly thermal stable by annealing. Using optical fibers with enhanced Rayleigh backscattering profiles as distributed temperature sensors, we demonstrated real-time monitoring of solid oxide fuel cell (SOFC) operations with 5-mm spatial resolution at 800^{o}C. Information gathered by these fiber sensor tools can be used to verify simulation results or operated in a process-control system to improve the operational efficiency and longevity of SOFC-based energy generation systems.

5.1 BACKGROUND

Over the last decade, optical fiber sensors have attracted growing interest for their resilience in many harsh conditions including in high-temperature, corrosive, and strong electromagnetic environments. Various optical fiber based sensors have been designed for applications with high operation temperature such as fossil-fuel and nuclear power generation systems, in which accurate and real-time parameter monitoring is highly desirable for safe and efficient operations. However, it's quite challenging to monitor the whole system by using these single point sensors. Distributed optical fiber sensing using unmodified fibers are becoming major thrusts in fiber optics research and engineering applications. Currently, distributed strain or temperature sensing schemes in optical fiber based on Raman[43], Brillouin[44], and Rayleigh scattering [87] have been widely adapted for many industrial applications. The method uses Rayleigh backscattering Optical Frequency Domain Reflectometry(OFDR) gives the highest spatial resolution of several millimeters while allowing reasonable temperature resolution of 0.1^{o}C [47, 51, 52, 88]. The main limitation of OFDR in sensitivity and accuracy comes from the weak intensity of the Rayleigh backscattering from the conventional fiber [53]. The weak Rayleigh backscattering is hardly a surprise, given that telecommunications optical fibers are designed for low-losses, including low Rayleigh-scattering losses. To address this challenge, several approaches have been attempted to increase Rayleigh scattering in fiber, such as UV exposure of the hydrogen-loaded single mode fiber[53], isotopes irradiation of Ge/P co-doped fiber[89], larger scattering cross-sections using polymer fiber[90]. The enhanced Rayleigh scattering profiles result in larger scattering signals at the detector(s) and better spectral correlation quality between the measured high-temperature Rayleigh profile and the reference room-temperature Rayleigh profile. This in turn improves the fidelity of the distributed measurement as well as the useful range of temperatures over which

the sensor-fiber can operate effectively. However, even though Rayleigh scattering enhancement may be used to effectively extend the operational temperatures and longevity of fiber sensors, eventually environmental effects will overcome the stability of the measurement during extended periods at high temperatures. Buric *et. al* reported rapid degradation of spectral shift quality of Rayleigh distributed temperature measurements at high temperature up to 800^{o}C[91]. These changes will eventually compromise sensitivity and reliability of the distributed measurements, although the use of the types of scattering enhancement modifications described here may delay or mitigate the effects of such degradation, yielding a new regime of measurement capability.

On the other hand, the direct laser writing (DLW) based on a femtosecond pulse induced multiphoton process is a fast, flexible and simple approach to induce high temperature-stable refractive index change in glass. And it has been used to fabricated high temperature resistance fiber Bragg grating which can operate above 1000^{o}C [92]. It's also used to produce random gratings to increase the light scattering in single-mode fiber for multi-parameter measurements[93] and the anisotropic index change result from the formation of self-ordered nanogratings were proved to be stable at high temperature[62, 94-96]. Thus, femtosecond pulse laser inscribed nanograting in fiber is a very attractive candidate to enhance the scattering in fiber for high temperature sensing applications.

In this section, we demonstrate uses of ultrafast laser irradiation to enhance performance of Rayleigh scattering based distributed fiber sensing. The ultrafast laser fabrication of Bragg gratings requires precise optical alignments for point-by-point grating writing. Alternatively, holographic or interferometric apparatus are needed to form periodic refractive index patterns in fiber cores. In contrast, the manufacturing method introduced here produce distributed fiber sensors with high spatial resolution using ultrafast laser pulses to perform continuously scan of

the fiber cores. It does not require point-by-point periodic laser writing or holographic laser exposure to form fiber Bragg gratings with nanometer precision in grating periods. Nanogratings contributing to the scattering enhancement was inscribed by direct laser writing in the core of the fiber. The enhancement and insertion loss was characterized at different scanning speed corresponding to different effective pulse number, which is believed to be critical to the geometry of the nanogratings [67]. The thermal stability of the enhancement was demonstrated at temperature up to 800^{o}C and the polarization properties are also characterized before and after the annealing process. With this thermal stable enhancement, distributed temperature measurement was demonstrated with 5-mm spatial resolution at 800^{o}C in highly reactive fuel gas (hydrogen) stream based on OFDR. Using this powerful sensing tool, we demonstrate distributed temperature measurement in an operating SOFC system. Information gathered by this fiber sensor tool can now be compared with simulation results to aid in SOFC system design, and ultimately improve the operational efficiency and longevity of the SOFC system.

5.2 FABRICATION PROCESS

The schematic diagram of the experimental method is shown in figure 25. The diameter of the fiber core is 9 μm, which has identical optical and material specifications as the Corning standard telecom fiber SMF-28. A Coherent RegA 9000 Ti:sapphire laser system operating at central wavelength 800 nm with pulse duration 300 fs and repetition rate of 250 kHz was used to boost laser pulses. The pulses from the RegA was then follow a beam path that allows for adjustment of the power through a rotating half-wave-plate. The on-target pulse energy was set

at 300-nJ, which was determined to be slightly above the threshold pulse energy required to enhance the Rayleigh backscattering of the fiber. A cylindrical telescope was used to shape the laser beam and control the shape of the focal volume. An 80X aberration-corrected microscope objective (NA = 0.75) was used to focus the irradiation beam. Oil immersed objectives (80×) were used to process cylindrical shaped fibers. The objective was also used to image the fiber and locate the fiber core with respect to the laser beam focal spot during the fabrication process, which allows for easier sample alignment of setup. The protection jacket of the fiber was removed with the length of 18 cm before the irradiation process. The laser beam was focused to the center of the fiber core. The beam waist diameter was estimated to be ~2 μm. The fiber being irradiated is also connected to a commercial OFDR interrogator (LUNA OBR4600). During the laser irradiation, the D-fiber samples were firmly clamped on a three-axis motion stage (Aerotech ABL2002) with repeatability of 50 nm and translated in the direction perpendicular to both the irradiation beam and the laser polarization. The translating speed of the stage varied from 0.1 mm/s to 1 mm/s, which allows to adjust the effective pulses number contributing to the formation of nanogratings at a specific spot. The laser was operated with a continuous pulse-train while the fiber can be translated over 20-cm longitudinally. With this ultrafast laser directly writing approach, we are able enhance the Rayleigh scattering profile in various optical fibers, including standard telecommunication fibers (Corning SMF-28), pure silica core fibers (Corning Vascade) and D-shaped fibers with a standard telecommunication fiber core.

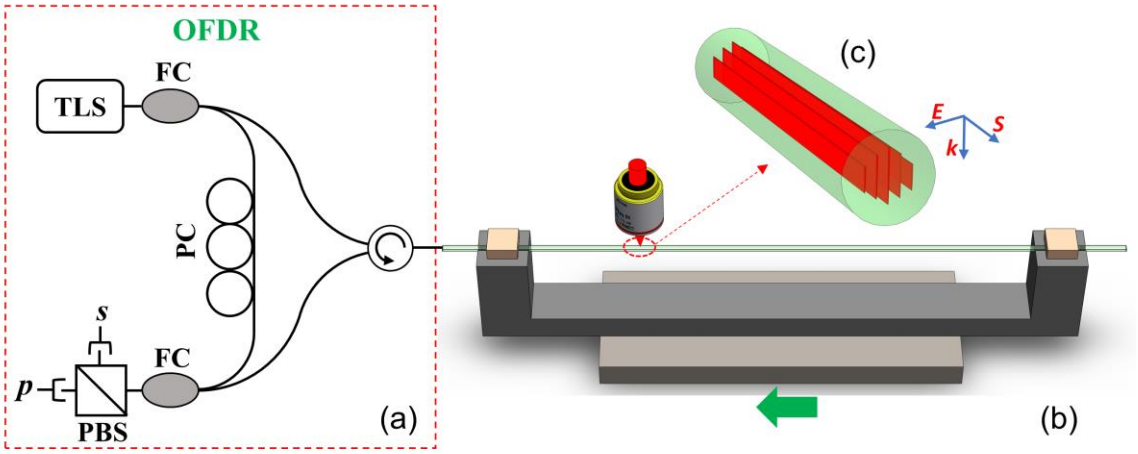

Figure 25. Schematic diagram of the ultrafast laser irradiation on D-shaped fibers.

5.3 ENHANCED RAYLEIGH SCATTERING PROFILES

First, a D-shaped fiber was used for demonstration, because it was easier to focus the laser into the core through the flat facet of the D-fiber. The diameter of the fiber core is 9 μm and the thickness of the cladding on the flat side is 3 μm. The laser beam was focused at depth of ~7 μm below the surface of the fiber, where the center of the core locates. The effective pulses number contributing to the formation of nanogratings was adjusted through different translation velocity. The quantity can be expressed as $N = d \times R/v$ here, where d is the width of the focal spot, v is the scanning speed and R is the repetition rate of the laser. Here, the translation speeds range from 0.1 mm to 1 mm/s, corresponding to effective pulse number ranging from 500 to 5000, were investigated to optimize the scattering profile. During the writing process, a commercial

Optical Frequency Domain Reflectometer (Luna OBR4600) was used to measure the change of the Rayleigh backscattering from the irradiation region in real time.

The use of the fiber for distributed measurement requires the insertion loss of the region is as small as possible to reach a longer detection length, while the loss of the modified section is determined by the volume of the formed nanogratings. And the volume of the formed nanogratings in the silica is highly depending on the pulse numbers and pulse energy [67, 97]. In order to minimize the insertion loss, the pulse energy is set to 300 nJ, which equals the threshold energy of producing self-ordered nanogratings here. Figure 26(a)~(c) shows the fiber backscattering profile at different scanning speeds, including the femto-second laser irradiated region with a length of 17cm at translation speed 0.1mm/s, 0.5mm/s and 1mm/s respectively. An increase with amplitude of 40~45 dB was obtained with irradiation by continuous laser pulses for all samples. The ultrafast laser irradiation did not yield Rayleigh scattering enhancements when the laser writing speed exceeded 2 mm/s. The laser irradiation also introduced significant optical propagation losses in the irradiated fiber-samples; which is characterized by the slope of the Rayleigh-enhanced region. At 300-nJ pulse energy, the average propagation losses in the irradiation sections are 0.41 dB/cm, 0.30 dB/cm and 0.15 dB/cm, respectively. Therefore, a scanning speed of 1mm/s was the optimal processing condition that minimized the insertion loss of the irradiated sensor-segment.

The morphologies of the nanogratings in the fiber core was directly characterized using an SEM (Zeiss Sigma 500 VP). The SEM sample was prepared by cleaving the fiber without any etching or polishing. Figure 26(d)~(f) present the different structures of the nanogratings corresponding to scanning speed of 0.1 mm/s, 0.5 mm/s and 1mm/s. It is clear that the ultrafast laser enhancement of the Rayleigh profile is closely linked to the formation of laser-induced

nano-gratings inside the fiber core. These nanogratings were only observed in fibers which exhibited enhanced Rayleigh back-scattering after processing. At present, several hypotheses have been proposed for the formation mechanisms of nanogratings including interference between the incident light field and the electric field of the induced plasma wave[65]; formation of spherically-shaped nanoplasmas from inhomogeneous hot-spots and their further evolution into periodic nanoplanes[60]; coupling between attractive interaction and self-trapping of exciton-polaritons[98]; and the development of periodically distributed defects near the edges of the irradiated section induced by plasma standing waves[67, 99]. Previous researchers have reported, the volume of laser-induced nanogratings in silica depends on the number of laser pulses and the total pulse energy deposited into the focal volume[67, 97, 100, 101]. These induced grating structures result in birefringence because the induced structures are oriented with respect to the induced standing plasma wave. This structural orientation will likely produce polarization-dependent Rayleigh scattering enhancement.

At the same time, periodically distributed nanoplanes can be observed clearly with intervals around 500 nm and 250 nm, which is corresponding to the wavelength or half wavelength of the laser pulse. The results in coarse agreement with the predicted and reported grating period of $\Lambda = \lambda/kn$, where k = 1, 2, 3 … [64, 65, 67, 68]. The width of the nanoplace is less than 20 nm. The depth of the nanograting in fiber with scanning speed of 0.1 mm/s is about 4 μm, while it's less than 1 um in fiber of 1 mm/s. The reason for the difference is that the effective pulse number of scanning speed of 0.1 mm/s is 10 times of the scanning speed of 1 mm/s. The volume of the nanogratings decrease when the scanning speed increase. However, all the back scattering in the presence of different scanning speeds increases by same order of magnitude, even for larger volumes with lower scanning speed as shown in figure 25(a) – (c).

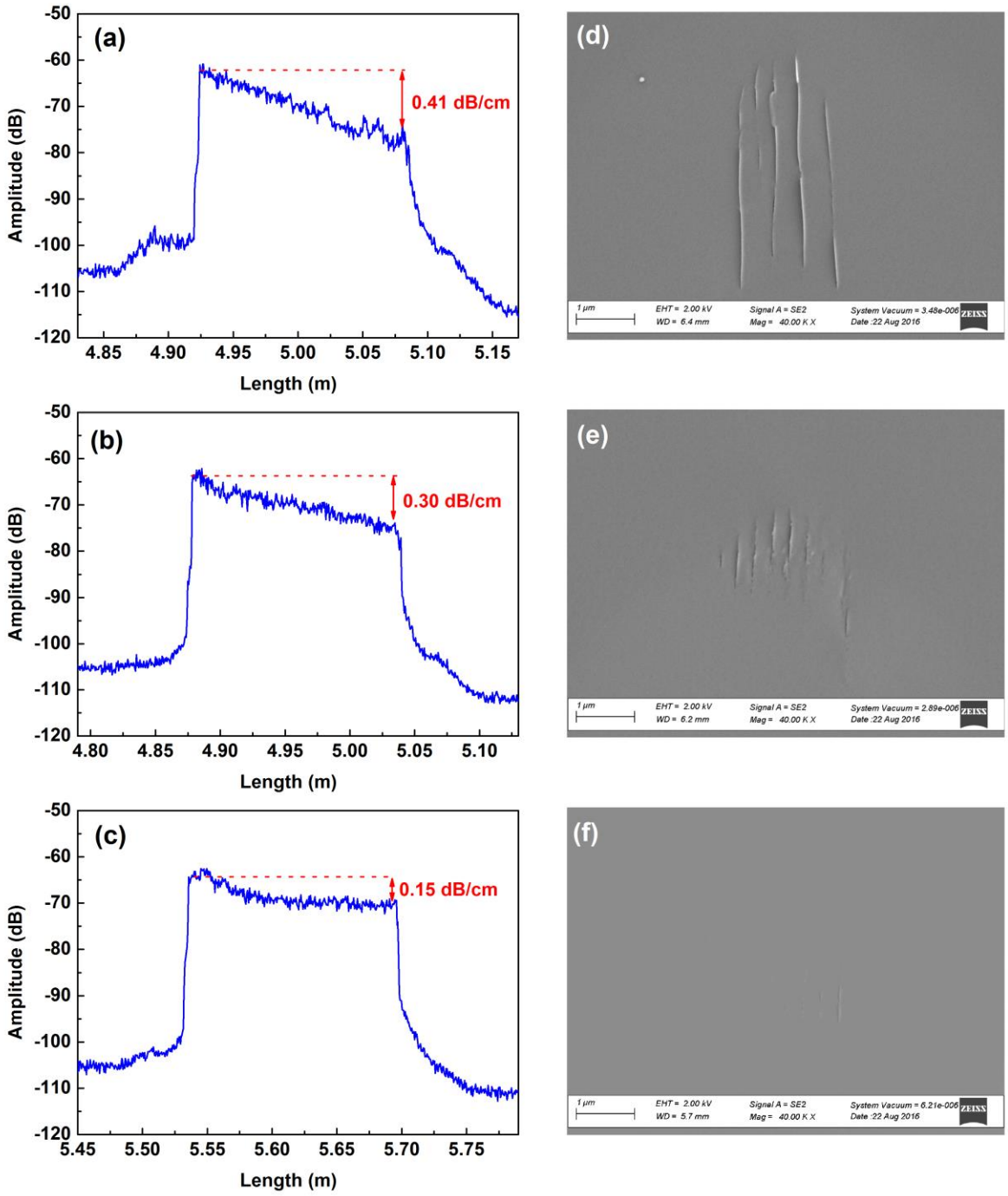

Figure 26. Enhancement of the Rayleigh backscattering after ultrafast laser irradiation. (a)-(c) Rayleigh backscattering features enhanced by the ultrafast laser and (d)-(f) cross-sectional morphologies of nanogratings at scanning speed of 0.1 mm/s, 0.5 mm/s and 1 mm/s, respectively.

To determine the resilience of the nanograting induced scattering enhancement at high temperature, the produced fibers samples using the femto-second laser irradiation technique were annealed in a tube furnace at 800^{o}C. With the tubing connected to the gas cell, the tube furnace is flushed with H_2 balanced with N_2. Two calibrated mass flow controllers were used to control the concentrations of H_2 up to 10% in the gas mixture. In this test, the temperature of the furnace was firstly raised up from room temperature to T = 800^{o}C in air flow, followed by holding there for 4 hours and switch to 10% H_2, The Rayleigh backscattering profile was monitored to determine the fiber sensor resilience while 10% H_2 was applied for 4 hours before switching back to air. The scattering profiles measured during the testing are presented in figure 27(a). The laser-enhanced section exhibits non-uniform Rayleigh intensity profiles where the beginning of the enhanced section has higher scattering amplitude than the end of the section. This is likely a direct result of optical loss from the propagation of the fundamental fiber mode through the laser-induced nanogratings in the fiber core. As the fundamental core mode propagates through the damaged core section, its intensity profile decreases due to the additional scattering loss. This is evident as shown in figure 26(a)-(b). This loss is closely connected to the formation of nanogratings as shown in figure 26(d)-(e). Via careful control of laser writing speed, it is possible to reduce the propagation loss in the enhanced section of the fiber, which results in a relatively flat Rayleigh profile (e.g. figure 26(c)).

The initial annealing process in N_2 at 800^{o}C yielded only a small decrease in the Rayleigh scattering profile. Given that the enhancements of Rayleigh scattering are closely tied to the formations of nanograting, the high temperatures stability of the Rayleigh profile are consistent with previous observations of temperature resilience of ultrafast laser induced nanogratings[94-96]. The subsequent exposure to 10% H_2 produced an increase in the scattering amplitude. This

change is permanent in both 10% H_2 and N_2 atmosphere as shown in figure 27(a). At the same time, the average loss of the irradiated fiber decreases to less than 0.1 dB/cm from 0.15 dB/cm (The main section has loss rate of 0.014 dB/cm, the near end has higher loss rate due to the fabrication imperfection). Per our experiment, the scattering increase in hydrogen can only happen when temperature is higher than 700^{o}C. This process occurs rapidly and the profile stabilized within 10 minutes in 10% H_2 atmosphere.

The birefringence of the irradiated fibers was also measured and correlated to the thermal annealing process using the OFDR instrument in order to shed light on stability of the laser-induced Rayleigh scattering and its degradation mechanisms. Given that nanogratings formed in the fiber cores are structurally asymmetric, they induce birefringence in negative uniaxial structures[65, 102]. The slow and fast optical axes of the induced gratings were aligned parallel and perpendicular to the nanoplanes, respectively [103]. Since the states of the PBS are rarely happened to match the principle state of the fiber in practical measurements, the periodic power variation can be measured at both detectors due to the beating of the two polarization modes and the beating length is given by the expression $L_b = \lambda/\Delta n$. Here, we make the assumption that the scattering signature of both of the polarization modes results from the same defect pattern. Figure 27(b)-(d) shows the Rayleigh backscattering signal demodulated into *s*- and *p*-polarizations by the OFBRs internal polarizing beam splitter [104]. The irradiated fiber produces scattering along both the fast and the slow axes of the fiber, which is not necessarily aligned with polarization states demodulated by the polarizing beam splitter. This results in birefringence beating as shown in figure 27(b)-(d). The fading of the beating fringes over the length of the irradiated section is caused by diminishing coherence of the two polarization modes as the spatial difference between the two modes exceeds the resolution limit of the instrument[104]. The

effective beating length of 3.2 mm was measured for the irradiated fiber at the laser scanning speed of 1mm/s as shown in figure 26(c) at 1.5-μm wavelength. The magnitude of the effective index difference (i.e. modal birefringence Δn) can be quantified by $\Delta n = \lambda / L_b = 4.8 \times 10^{-4}$, which agrees with birefringence in type II-IR gratings fabricated by ultrafast lasers in silica[105]. After annealing at 800°C in N_2 for 4 hours, the beating length increased and settled to 4.9 mm. This corresponds to a slight reduction of the modal birefringence to 3.2×10^{-4} as shown in figure 27(c). In sharp contrast, exposure in 10% H_2 at 800°C quickly reduced the birefringence to $<10^{-6}$ as shown in figure 27(d).

To determine the origin of this decay in birefringence, SEM photos of the nanogratings in samples annealed in air and H_2 are reported in figure 27(e) and (f). As shown in figure 27(e), parts of the nanoplane have morphed into several discontinuous shorter segments after annealing in air, which results in a slight decrease in the birefringence. However, for the fiber samples annealed with hydrogen, the nanograting planes evolve into a series of nanopores with diameters around 50-nm (figure 27(f)), this is probably the underlining cause of the decrease of optical loss of the irradiation fiber as shown in figure 27(a). A possible reason for this pore formation is that the nanograting features in silica are more likely to be densified during exposure to hydrogen at high temperatures[106]. As a result, birefringence for the nanogratings was almost erased after hydrogen exposure.

To further characterize the induced Rayleigh scattering stability, the annealed fibers were used as temperature sensors over a wide range of applied temperatures. Temperature changes are measured by the OFDR system by cross-correlating the Rayleigh backscattering profile at a known temperature with the Rayleigh backscattering profile after heating. This cross correlation yields a spectral shift value plotted over the length of the test-section which may be further fitted

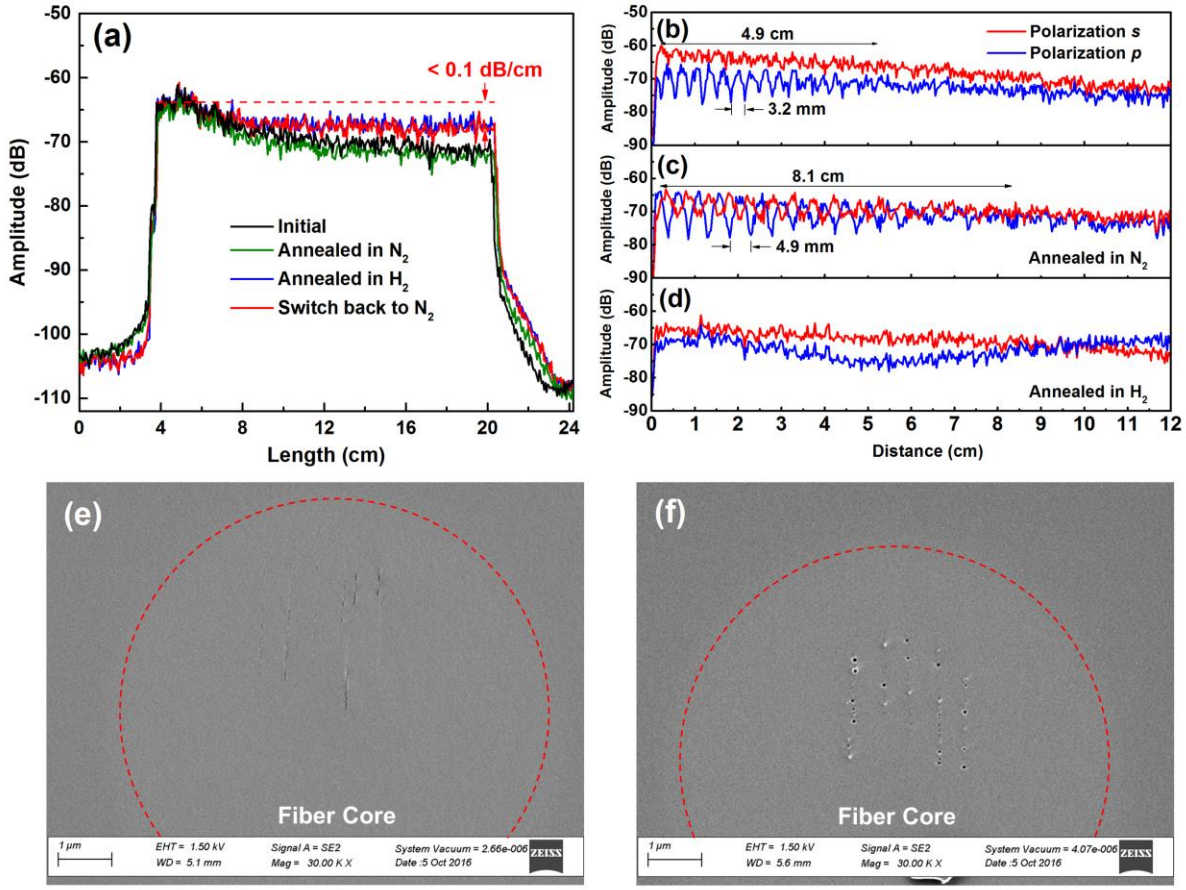

Figure 27. Anneal process at 800°C in N_2 and 10% H_2. (a) OFDR measurements of scattering amplitude during anneal process. (b)-(d) scattering signal in two detected polarization states of the processed fiber before and after high temperature anneal in in N_2 and 10% H_2 respectively. (e), (f) morphology change of nanogratings.

to the temperature using a calibration curve intrinsic to the fiber material. After the initial thermal annealing in 10% hydrogen at 800°C for 10 minutes, the Rayleigh scattering enhancement becomes significantly more stable. The scattering profiles measured using the annealed fibers from 24°C to 800°C in a 10% H_2 atmosphere are shown in figure 28(a). No significant scattering amplitude changes were observed as compared to the post-annealed fiber. Figure 28(b) shows the comparison of the spectral shift quality between the laser-irradiated fiber and a normal single-mode fiber (Corning SMF-28) at 800°C. The spectral shift quality is a measure of the strength of correlation between the backscattering profiles in measurement and reference spectra[52]. The parameter is defined as the maximum value of cross-correlation between the measurement and reference spectra normalized by the maximum of the reference spectrum autocorrelation. The reference spectrum was recorded at 800°C. A spectral shift quality of 1.0 indicates that there is a perfect match between reference and measurement spectra. The shift quality will decrease when the scattering signal becomes significantly different from the reference signal. Results shows that the spectral shift quality at T = 800°C under 10% hydrogen decreased from 1 to less than 0.3 within 2 hours for Corning SMF-28 fiber, while the spectral shift quality in the fiber with the enhanced scattering profile remained above 0.8 for the same time period. When the irradiated fiber was tested more than 20 hours under the same conditions, the value of the spectral shift quality remained above 0.75. This result shows that distributed temperature measurement can be performed with high fidelity at high temperature over a long period of time; even in a highly reactive hydrogen containing environment.

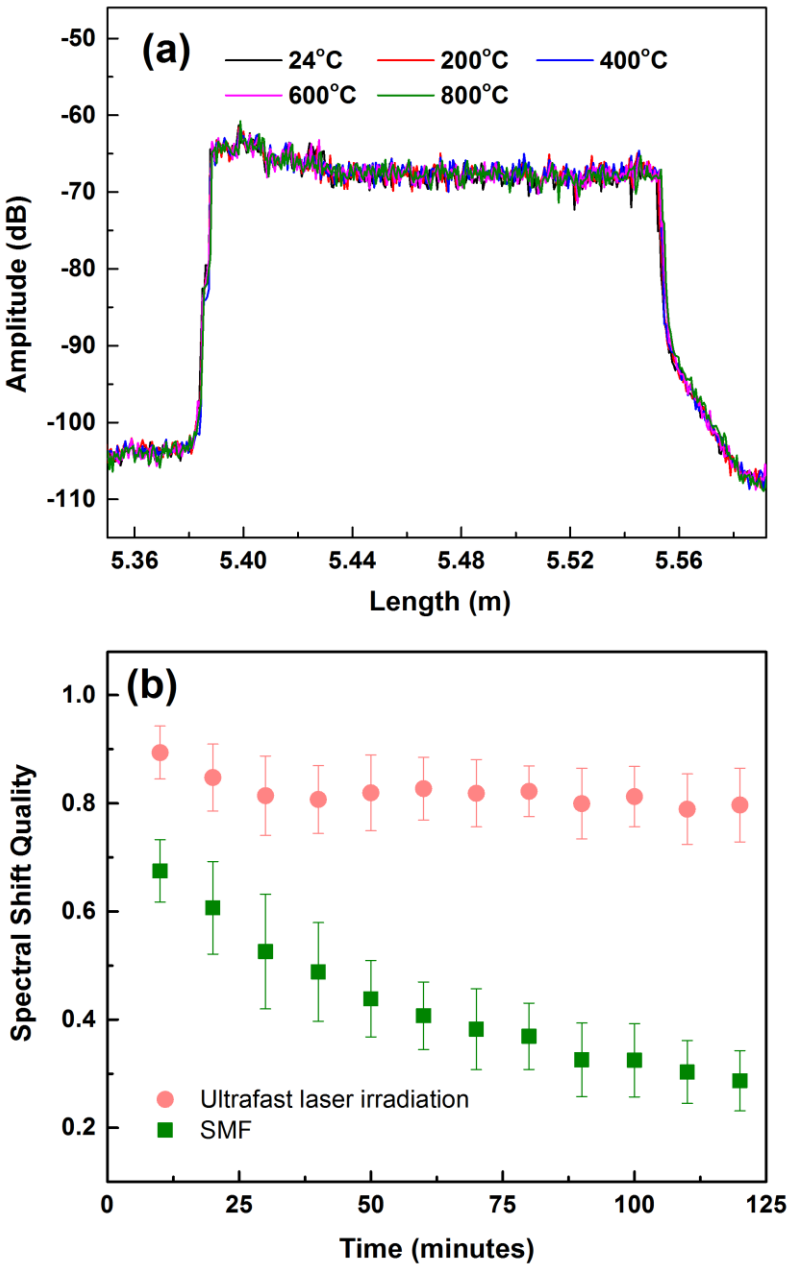

Figure 28. Stability of the enhanced scattering signal evaluated at high temperature. (a) thermal stability of scattering features after anneal process and (b) comparison of the spectral shift quality vs time at 800°C for fiber with ultrafast laser inscribed nanogratings and un-irradiated SMF fiber. For these measurements, the fiber was set into a tube furnace with heating capability up to 800°C.

The temperature dependence of the fiber segment with enhanced scattering was characterized over the temperature range from 24^{o}C to 800^{o}C. Figure 29(a) shows the spectral shift versus temperature change for the ultrafast laser irradiated fiber. There appears to be a change in slope around 300^{o}C. Two linear temperature-spectral shift coefficients are obtained in respective temperature regimes. Between 23^{o}C and 300^{o}C, the temperature changes linearly depend on the spectral shift with a slope of $-\partial T/\partial \nu \sim 0.67$ ^{o}C/GHz. While in temperature above 300^{o}C, the coefficient changes to ~ 0.53 ^{o}C/GHz. This temperature dependent coefficient change is caused by the transition change of glass around 300^{o}C [107]. The formation of nanogratings also results in a significant increase in the spectral-shift quality for distributed temperature measurement over a wide temperature range. This is shown in the inset of figure 29(a). When the Rayleigh profile at 23^{o}C was taken as the reference, and the temperature was then increased to 800^{o}C; the spectral shift quality remained above 0.3, which is significantly higher than the threshold spectral-shift quality required for reliable temperature measurement (0.15).

With the calibrated coefficient, distributed measurement of high temperature was tested using a tube furnace, in which most of the heated zone was set to temperature of 800^{o}C at the highest heating level. The furnace was heated up by two heaters with spacing ~ 7 cm. The spatially resolved temperature profile during the heating process of the furnace was shown in Figure 29(b) with spatial resolution of 0.5 cm. Figure 29(c) shows the temperature measurement repeatability using Rayleigh-enhanced fiber. The reference spectrum was taken at 23^{o}C. Then the temperature of the test furnace was raised to 800^{o}C. To gauge the repeatability of the distributed fiber sensor, the furnace was cooled to the room temperature and repeat the above thermal cycles 8 times. Error bars presented in figure 29(c), show a standard deviation less than 4^{o}C, which highlights the measurement reliability and repeatability.

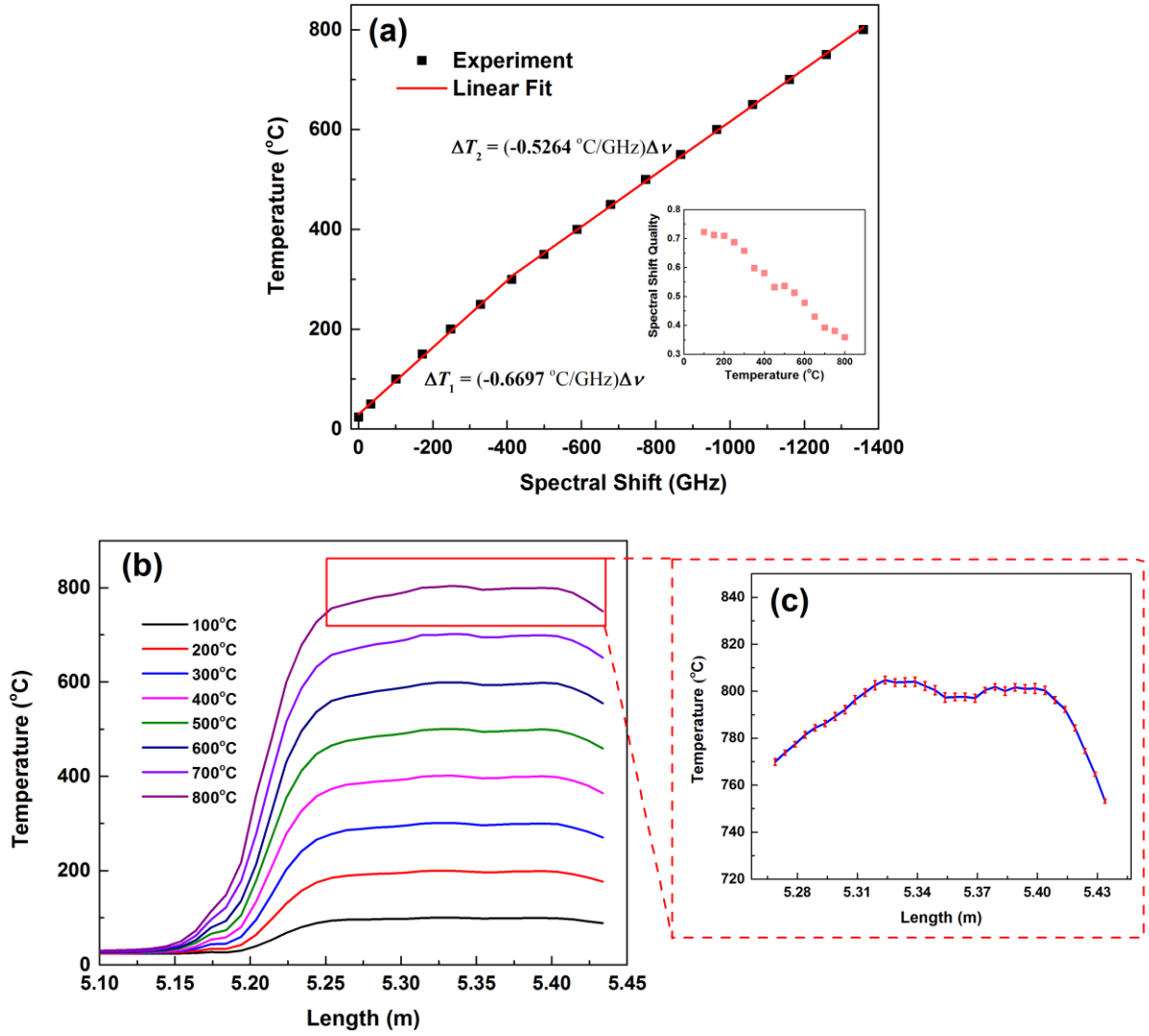

Figure 29. Calibration of the thermal coefficient of the distributed fiber optic sensor. (a) frequency shift at different ambient temperature for the fiber with enhanced back scattering. The inset shows the spectral shift quality of the fiber reference to the measurement at room temperature. This value will decrease as the temperature difference increase. (b) temperature profile of a tube furnace operating at 800°C. The error bar was obtained by 8 different measurements for each with cooling cycle to room temperature.

The measurement also reveals that the heater locations have slightly higher temperatures than the location of thermocouple which was regulating the temperature. In the experiment, 20 sccm of 10% hydrogen flows from one side of the furnace's quartz tube to the other. As a result of the high thermal conductivity of hydrogen gas, larger temperature gradients were observed from the gas injection side (right side in the figure). These fine details of the temperature profile revealed by the distributed fiber sensors highlight the excellent temperature measurement capability which is useful for both the design and control of energy systems.

5.4 TEMPERATURE DISTRIBUTION OF OPERATIONAL SOFC

Solid oxide fuel cell (SOFC) technology is a promising and versatile energy generation scheme. SOFCs are used in a wide variety of applications ranging from clean automobiles to distributed electric power generation systems. SOFCs in stand-alone or hybrid generation configurations can utilize a wide array of gaseous fuels from hydrogen to biogas to achieve high energy conversation efficiencies and low emissions. Modern SOFC system exhibit high internal reaction temperatures, and are capable of internal gas-reforming to provide fuel flexibility and increased versatility. However, the long-term stability of SOFC-systems is primarily hindered by material and structural degradation; which impacts the profitability of large-scale SOFC system deployment. In order to improve the longevity of SOFC systems, we must be able to measure and engineer the temperature distribution inside fuel cell assembly. Temperature variations in an SOFC assembly are a result of convection as gasses with varying thermal conductivities flow through the cell, conduction of heat through the supporting structure, and the heat generated by the distributed internal reforming or oxidation reactions producing electrical output. Each of

these processes contributes to temperature variations inside a fuel cell. The temperature variations are responsible for the thermal stresses, which are one of the main issues that impact the lifetimes of SOFCs[108-110]. In addition, the spatial temperature variations also affect the current density distributions in SOFCs through the generation of local over-potentials[111]. Thus, the improvement and optimization of fuel cell lifetime and performance relies on a detailed understanding of temperature profiles inside an SOFC. Currently, numerical simulations are used to estimate temperature distributions in SOFC systems because experimental measurements during operation have been extremely challenging. Thermocouple devices have been used by some researchers to perform single-point measurements[110, 112]. As many as 36 thermocouples have been inserted in a fuel cell stack to perform multi-point measurements[112]. However, each thermocouple requires 2 electrical wires for each point-measurement; each of which introduces additional heat-losses which skews the accuracy of measurements. It is also physically impossible to place thermocouples in extremely close proximity to one another in order to produce high spatial-resolution measurements. Large numbers of wires in the cell could also impede fuel gas-flow, which may further alter the temperature profile during measurement.

Distributed fiber optic sensing is a potentially powerful technique to measure the spatial temperature profile of an operating SOFC system. Being well-suited for harsh environment sensing applications, fiber optic sensors have been widely used for high-temperature measurements. Distributed sensing schemes such as Rayleigh-scattering Optical Frequency Domain Reflectometry (OFDR) can perform distributed temperature sensing using unmodified single-mode optical fiber to achieve <1-cm spatial resolution. One of the key challenges of distributed sensing using the Rayleigh backscattering is the weak Rayleigh-backscattering intensity exhibited by conventional optical fibers. With this thermal-stable scattering feature in

fiber, we could perform distributed temperature measurements in a high temperature solid-oxide fuel cell (SOFC).

The fuel cell tests described here were performed at the U.S. Department of Energy's National Energy Technology Laboratory fuel-cell testing facility (Morgantown, WV). This fuel cell has a yttria-stabilized zirconia (YSZ) electrolyte, a Ni-YSZ anode, and a $La_{1-x}Sr_xCo_{1-y}Fe_yO_{3-d}$ (LSCF) cathode. The anode support is 5 cm x 5 cm, and the cathode active area is 4 cm x 4 cm. The SOFC presents a challenging harsh environment for most sensors with temperature up to 800^{o}C and ambient hydrogen concentration potentially ranging from 0-100% across the cell's anode.

Figure 30(a) shows the schematic of the SOFC with counter-flow configuration. Hydrogen fuel flows from the inlet to the outlet across a series of parallel channels on one side of the electrolyte, while the air flows in opposite direction on the other side of the electrolyte. The distance from the inlet to outlet is 8 cm and the length of the electrolyte is 5 cm. In order to probe the temperature change at different electric loads, fiber sensors were placed in the anode channel and cathode channel respectively, as shown in figure 30(b). Before installing fiber sensors, the fuel cell assembly was heated up to 860^{o}C to form a gas-tight seal using glass-ceramic sealant. The completed cell was then aged at 750^{o}C for 6 h to reduce the anode material under 100% H_2. After checking the normality of fuel cell operation, the assembly was brought down to room temperature and fiber sensors were inserted into the cell through nickel tubes which provided access to the cell-body and encased the fiber-sensor outside the cell-body. Both ends of the tubes positioned outside of the furnace were sealed with silicone putty where the fiber entered or exited the assembly. Prior to the operation, the sensor-embedded fuel cell was heated externally to ~ 720^{o}C, which is confirmed by both point thermocouple devices and the

distributed fiber sensors. The cell was seat in furnace with temperature hold at 800^{o}C. Due the heat dissipation of the supporting structure, the temperature of the cell is about 70^{o}C – 90^{o}C lower than the furnace. The distributed temperature profile of the cell was continuously monitored and compared with the reference during heating. Once the SOFC reached operational temperature, 500 sccm of 100% hydrogen was injected into the anode and 500 sccm of air was also injected into the cathode.

A strong gradient of temperature exists from the fuel-inlet to outlet when pure hydrogen was introduced at the anode. Figure (b)-(e) shows the temperature distribution with 5-mm gauge length. At the anode side, the temperature around the fuel inlet increase up to 55^{o}C above ambient. The temperature peaks near the border area of the electrolyte area. This is caused primarily by high thermal conductivity of hydrogen fuel. The electrolyte has significant influence on the temperature profile on the cathode side, where the temperature rise was much lower at about 25^{o}C. The temperature variation induced under different electric loads was also measured with load-current ranging from 0 A to 3 A. The current loading resulted in a slight temperature increase near the center section of the fuel cell. At a 3-A current, the temperature increase on both anode and cathode sides was about 5^{o}C. While this reaction-induced temperature profile change might not be a significant issue for a single SOFC operating with external applied heating, the cumulative induced temperature effects on stacked self-heated fuel cell assemblies should be carefully studied. The fuel-gas induced temperature changes inside the fuel cell depend strongly on the flow rate of hydrogen and its concentration. We note anecdotally that a mixture of 4% H_2 does not exhibit significant convective heating effects on the SOFC assembly, while a 10% mixture induces readily observable convective effects. Given that the convective impacts of fuel gas streams on temperature profiles at the anode and cathode are

significantly different, designing and implementing an optimal temperature control scheme will require modelling of the thermal characteristics of the SOFC assembly, along with the thermal and chemical properties of the cell materials and applied gases. The distributed fiber sensor demonstrated in this paper provides a new and valuable tool to measure the constantly-evolving SOFC temperature profile, which will lead us towards optimizing the efficiency and longevity of SOFC-based energy systems in the future.

In summary, we demonstrated that the Rayleigh scattering profile from commercially available silica fibers can be enhanced by 40~45dB through nanograting formations in the fiber core. This increases the available measurable intensity at the optical detectors, leading to significant improvements in both the SNR and spectral shift quality of an OFDR-based measurement. The new Rayleigh backscatter features induced by femtosecond laser irradiation are stable at high temperatures, which enables reliable temperature measurements in extreme environments. Using this distributed sensing tool, reliable temperature measurements were achieved from room temperature to 800^{o}C with 5-mm spatial resolution.

The capability for real-time temperature monitoring with high spatial resolution within operational energy conversion devices represents a significant opportunity for process efficiency and long-term stability; which are two key metrics required for enabling widespread deployment of SOFCs in the power generation sector. The system described here will also be useful for measurements in existing harsh-environment energy systems including combustion systems, boilers, and gas turbines. Distributed high-temperature sensor technology represents a major opportunity for potentially improved efficiencies, mitigating against undesirable emissions, improving safety, and reducing the cost of electricity to the consumer by decreasing maintenance and downtime.

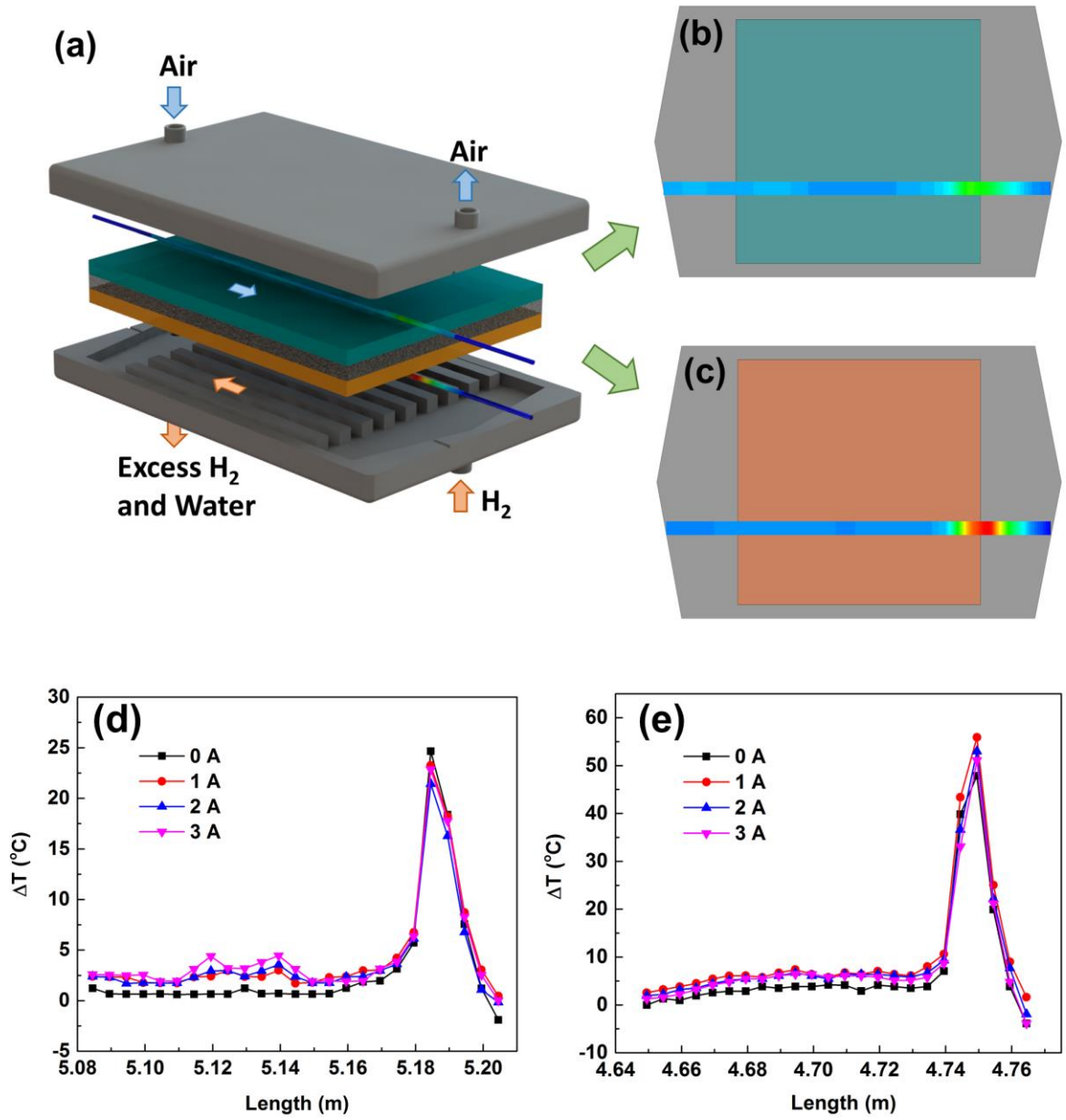

Figure 30. Temperature variation change of the cathode and anode in the solid oxide fuel cell at different current load. (a) Schematic of the solid-oxide fuel cell. Temperature measurement in (b), (d) cathode and (c),(e) anode at current 0 A, 1 A, 2 A, 3 A respectively with 100% hydrogen fuel.

6.0 MULTI-POINT FIBER OPTIC SENSORS FOR REAL-TIME TEMPERATURE DISTRIBUTION MONITORING

In this chapter, a distributed fiber optical temperature sensing system based on random air hole fibers is presented. The sensing element is fabricated using low loss random air hole fibers infiltrated with CdSe/ZnS quantum dots(QDs), of which photoluminescence properties are strongly dependent on the ambient temperatures. The intensity and peak wavelength change of the photoluminescence was studyed for temperature range from 23^{o}C to 120^{o}C. By bundling multiple sensors together, the temperature at multiple locations could be real-time monitored using one CCD camera. Based on this multipoint temperature sensing system, the temperature distribution in lithium-ion battery assembly was monitored during the charging and discharging process. Rapid temperature increase of the battery was observed during the high-rate of discharges.

6.1 BACKGROUND

Optical fiber sensors have attracted growing interest for their resilience in many harsh conditions including in corrosive, and strong electromagnetic environments. Various optical fiber based sensors have been designed for energy applications, in which accurate and real-time parameter monitoring is highly desirable for safe and efficient operations. Among the various optical

mechanisms, luminescence based sensors are especially sensitive and cost-effective. By combining the luminescent with optical fibers, remote and distributed detection can be achieved.

QDs are by far one of the most highlighted fluorescent materials used for sensing applications due to their unique optical and electronic properties[113]. The QDs are semiconductor nanoparticles with strong fluorescent properties subject to the quantum confinement effect[114]. The emission wavelength of the QDs can be suitably tuned by changing the size of the nanoparticles, which gives a large choice of emission wavelength. Additionally, both the emission intensity and the peak wavelength of the QDs highly depends on the ambient temperature, enabled their potentials in temperature sensing such as thermal imaging, biological labeling [115]. Recently, reversible PL changes of the QDs in intensity and wavelength for temperature sensing are investigated at moderate temperature up to 525K[116]. The sensing capability in this temperature range is quite suitable for lithium-ion battery and high-power transformer. By depositing QDs on optical fibers, several temperature sensor probes have been reported using fiber taper [117], hollow core fiber[118], and photonic crystal fiber[119]. The life time of the sensor was dramatically improved by encapsulating the QDs in the fiber. Taking advantage of the remote sensing capability of optical fiber and tunable wavelength of the QDs, it's very suitable for parallel sensing at different locations. However, all the reported sensors using fiber incorporated with QDs are compromised in practical applications for difficult fabrication process, poor sensitivity and expensive material.

In this chapter, we demonstrated multipoint temperature sensor based on the random hole fiber infiltrated with CdSe/ZnS core-shell type quantum dots. The large number of the random holes of the fiber provide a large optically active volume in which quantum dots were embedded using capillary effect. It also provides good protection of the quantum dots from ambient

environment by sealing the fiber end. Due to the compact size of the fiber sensor tip, the sensor can be easily integrated with battery assembly. Here, the luminescent properties of the QDs based sensor was firstly investigated. The thermal behavior of the emission intensity and peak wavelength at different temperatures was characterized and calibrated. Based on the emission intensity measurement, we built a multipoint temperature sensing system by bundling multiple sensors together and using one CCD camera to real-time measure the intensity variations. Finally, we demonstrated the used of the multipoint sensing system in thermal dynamics monitoring of lithium-ion battery pack which is widely used in electric cars.

6.2 SENSOR FABRICATION AND CHARACTERIZATION

Scanning electron micrograph of the random hole optical fibers shown in figure 31(a) is a multimode fiber, while the figure shown in figure 31(b) is a single mode fiber. The diameter of two fibers are both 125 μm. For single mode fiber, the fiber core is surrounded by a porous cladding, which has lower refractive index comparing to the dense silica. For the multimode fiber, micro pores are uniformly distributed in the whole core region and the diameter of the core is about 100 μm. Due to the existence of the random holes, the effective refractive index is lower than bulk silica. To support the guiding mode in the porous core, the cladding of the fiber was doped with boron to make sure the cladding is lower than the porous core region. The transmission loss of this multimode random air hole fiber was measured using cutback method and the loss in the fiber was measured to be around 1 dB/m at 462 nm. The structure shown in the figure is randomly variant along the fiber and the length of the holes is around 0~3 cm. Figure 31(c) shows a larger magnification of the porous region. As shown in the figure, the size

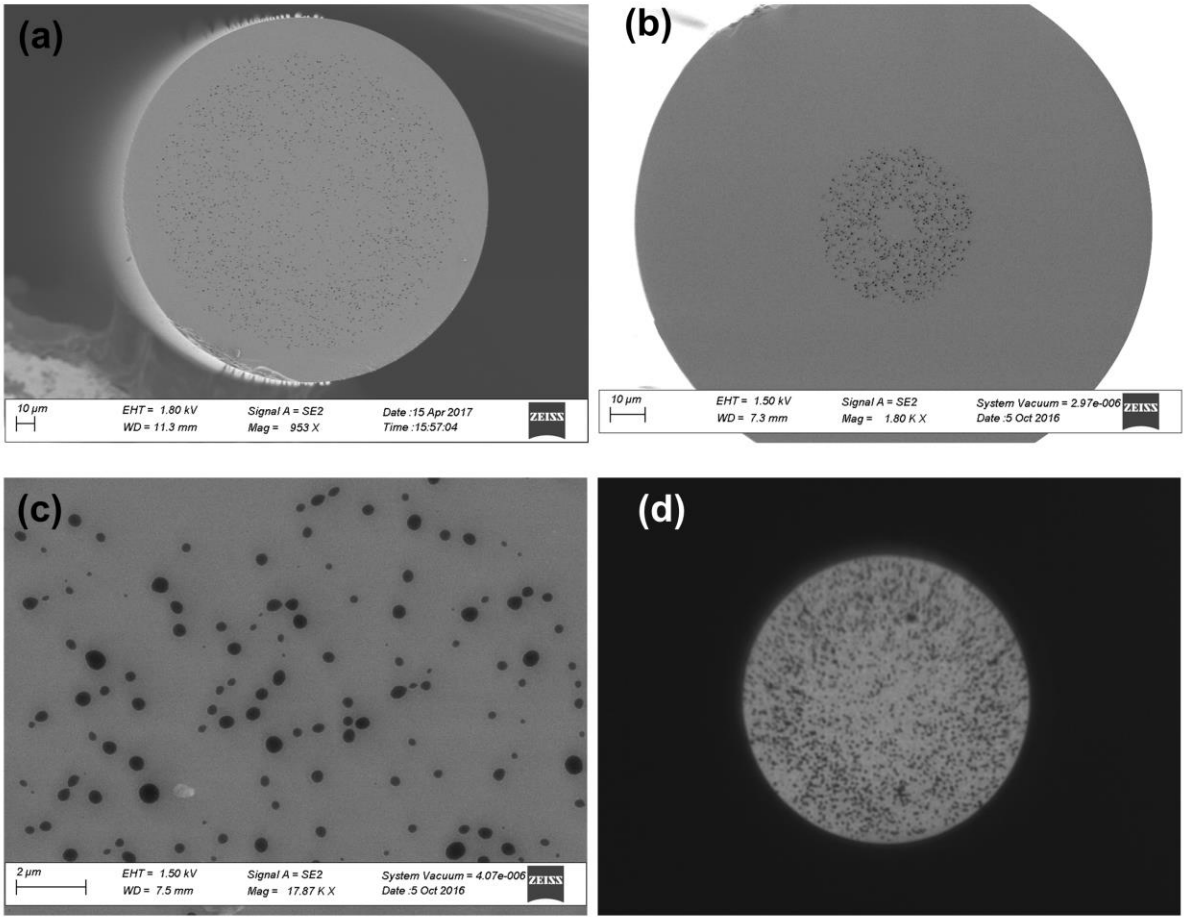

Figure 31. Random air hole fibers. (a) Cross-section SEM image of multimode random hole optical fiber and (b) single mode random hole optical fiber, (c) magnified image of the region of the core, (d) cross-section of multimode random hole optical fiber under white light illumination.

of the holes ranging from 1um to less than 50 nm. Owing to its uniformly distributed holes in the core region and low loss properties, the random hole fiber has great potentials for remote sensing platform as the holes could hold sensing medium inside. A cross-section image of multimode fiber under the white light illumination was presented in figure 31(d). Obviously, the multimode fiber has much larger optical active region comparing to the single fiber, which utilize the evanescent field to excite the sensing medium. Additionally, the light coupling of multimode fiber with 100 μm core is much easier than the single mode fiber with only 10 μm core.

The CdSe/ZnS core-shell type QDs (Sigma-Aldrich) used in this experiment have a 5 nm diameter and emission wavelength at 586 nm. In order to embed the QDs into the random hole optical fiber, 8 mg of highly purified CdSe/ZnS QDs were dispersed in 0.4 g toluene solvent, followed by sonicating for 3 minutes. Then a cleaned and cleaved end of a fiber sample was immersed into the colloidal QDs solvent for a duration of 30 mins and the solvent infiltrated into the holes by capillary effect. After that, the fiber was dried by evaporating the solvent in air for 24 hours, leaving with quantum dots thin film coatings on the inner wall of the holes. Finally, the fiber end was arc fused to seal as shown in the inset of figure 32(a), and the quantum dots was encapsulated in the holes of the fiber to protect against the exterior environmental agents. Figure 32(a) shows the digital image of the sensor probe under the illumination of excitation light. The fluorescence of QDs can be clearly observed and the infiltrated length of the QDs is about 2~3 cm.

The behavior of the emission of the single fiber sensor probe was examined by excitation at 462 nm. The excitation light from a laser diode (Thorlabs, LP462-MF1W) was coupled into multimode fiber and spitted with 2x2 fiber coupler. One beam was launched into the random hole fiber sensing probe with length of 3 meters and the other beam was monitored using power

meter. The excitation light guided in the random hole fiber and interacted with the QDs in the fiber tip. The fluorescent emission was collected by the same fiber and then launched end to the spectrometer (BW Tek, Compass^{TM} X) after using a 488-nm long pass filter to reject the excitation light. The sensor was first annealed at 130 ^{o}C in the furnace. A permanent red shift of the emission wavelength was observed with respect to the original emission of the QDs.[120] The sensor shows stable response and repeatability after the thermal anneal process.

To characterize the dependence of the emission intensity as a function of the excitation power for a random air hole fiber sensor at room temperature, different excitation powers ranging from 0.1 mW to 1.2 mW was launched into the fiber and the respective emission spectra was shown in figure 32(b). The peak wavelength of the emission is 586 nm. Due to the large optical active volume of the random hole fiber, the fiber sensor shows highly efficient excitation of QDs as well as fluorescence collection. The fluorescence was detectable even excitation power less than 0.1 mW. We can also note that the emission intensity is proportional to the excitation power as shown in figure 32(c).

Subsequently, the temperature-dependent emission of the sensor was investigated by mounting the sensor into a custom-built temperature cell. The excitation power from the laser diode was fixed at 1 mW for the luminescence measurements. The integration time of the spectrometer was 10 ms. Figure 32(d) shows the evolution of the emission spectra of the QDs sensor when the temperature was increased from 23^{o}C to 120^{o}C. The heating ramp of the temperature cell is set to 3^{o}C/min and the data were taken every 10^{o}C with dwell time of 5 minutes. A temperature caused read shift of emission wavelength, and simultaneously, reduction of quantum efficiency can be clearly seen from the spectra. So, both intensity and the peak wavelength of the emission can be used for thermal sensing and the dependence with

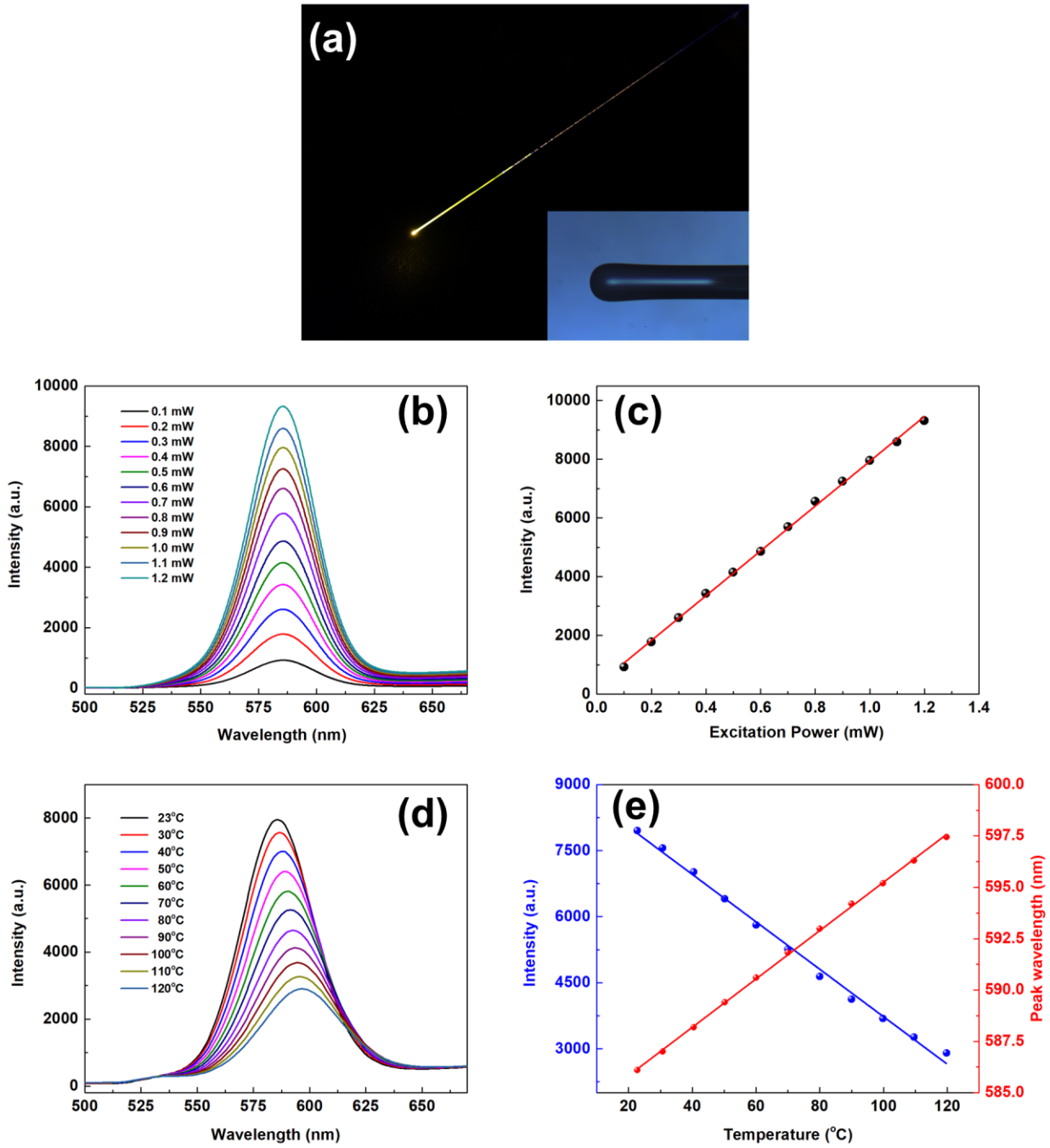

Figure 32. Temperature sensor based on random hole fiber infiltrated with CdSe/ZnS-QDs. (a) Digital image of the sensor probe obtained at room temperature under optical excitation; (b) emission spectra and (c) peak intensity of the CdSe/ZnS-QDs sensor probe at different pumping power; (d) emission spectra and (e) peak intensity/wavelength of the sensor probe at different temperatures.

temperature was plot in figure 32(e). As can be observed, the thermally induced intensity linearly decreased from room temperature to 100^{o}C and the fluorescence suffers a total reduction of 54% (0.7%/ ^{o}C). When temperature increased above 100^{o}C, the decreased of the intensity was slow down. A total reduction of 64% was observed when temperature was 120^{o}C, which is corresponding to 0.5%/ ^{o}C. The reduction of the QDs emission intensity is attributed to the thermal activation of surface trap states and an increased recombination probability of the nonradiative excitation [113]. To gauge the repeatability, the response of both intensity and wavelength shift was measured for 3 heating-cooling cycles. In this temperature region, the decrease of emission intensity is fully reversible[121].

At the same time, the emission peak red shift about 11 nm when temperature increased from 23^{o}C to 120^{o}C as shown in figure 32(e). The thermally induced spectral red shift is linearly dependent on the temperature change and the sensitivity shown by the sensor is around 0.113 nm/^{o}C, which is comparable to previously reported values in different QDs (ranging from 0.08 to 0.2 nm/^{o}C). [115, 119, 120, 122, 123] The temperature red shift of the emission wavelength is due to the temperature-dependent bad-gap shrinkage of the QDs. As the temperature increases, the crystalline network of the QDs will expand resulting in the barrier height changes. Due to the different temperature dependence of the CdSe and the ZnS energy gap, and the potential well becomes larger, due to thermal expansion.[113, 114, 116]

After we investigated the temperature influence on the emission properties of the CdSe/ZnS QDs embedded in random hole fiber, the next step is to demonstrate its use for multipoint sensing of Li-Ion battery assembly. The results in figure 32 indicate that the fluorescence intensity of the CdSe/ZnS QDs embedded in random hole fibers decreased with the increasing temperature. In order to realize multipoint sensing, the intensity from multiple sensors

should be recorded at the same time. For this purpose, we build a temperature sensing system using fiber bundle with 8 individual sensors as figure 33(a) shows. One single CCD camera was used to continuously monitoring the emission intensity of the QDs. The fiber bundle was fabricated by fixing the fibers in a ceramic ferrule using epoxy, followed by precisely polishing of the end face. The inner diameter of the ferrule is 400 μm which could fit 8 fibers.

The 462-nm exaction light from laser diode can be launched into the fiber bundle using a focal lens. Due to the gaussian distribution of the laser source, the sensor in the center of the bundle would has higher intensity of excitation power and resulting higher intensity of fluorescence emission. In order to get homogeneously emission intensity from all the sensors in the bundle, an engineered diffuser was placed right after the collimator to diffuse the gaussian laser beam into top-hat distribution. Then the laser beam with homogeneously intensity was coupled into the fiber bundle using a focal lens. The excitation laser beam was focused down to a spot size of 1.5 mm with estimated power density of 8 mW/mm^2. The power coupled into each sensor is about 0.2 mW. The backpropagated fluorescence emission from the QDs was collected through the same focal lens. After passing the aperture and a 488 nm long-pass filter, the fluorescence emission from the bundle end face was imaged using a CCD camera (Point Grey, BFLY-U3-13SM). The captured images were streamed to a PC and quantify the fluorescence intensity in both time and location. The different sensors were labeled using connected component algorithm and the fluorescence of the intensity was quantified in 4096 levels (i.e. 14-bit grey scale).

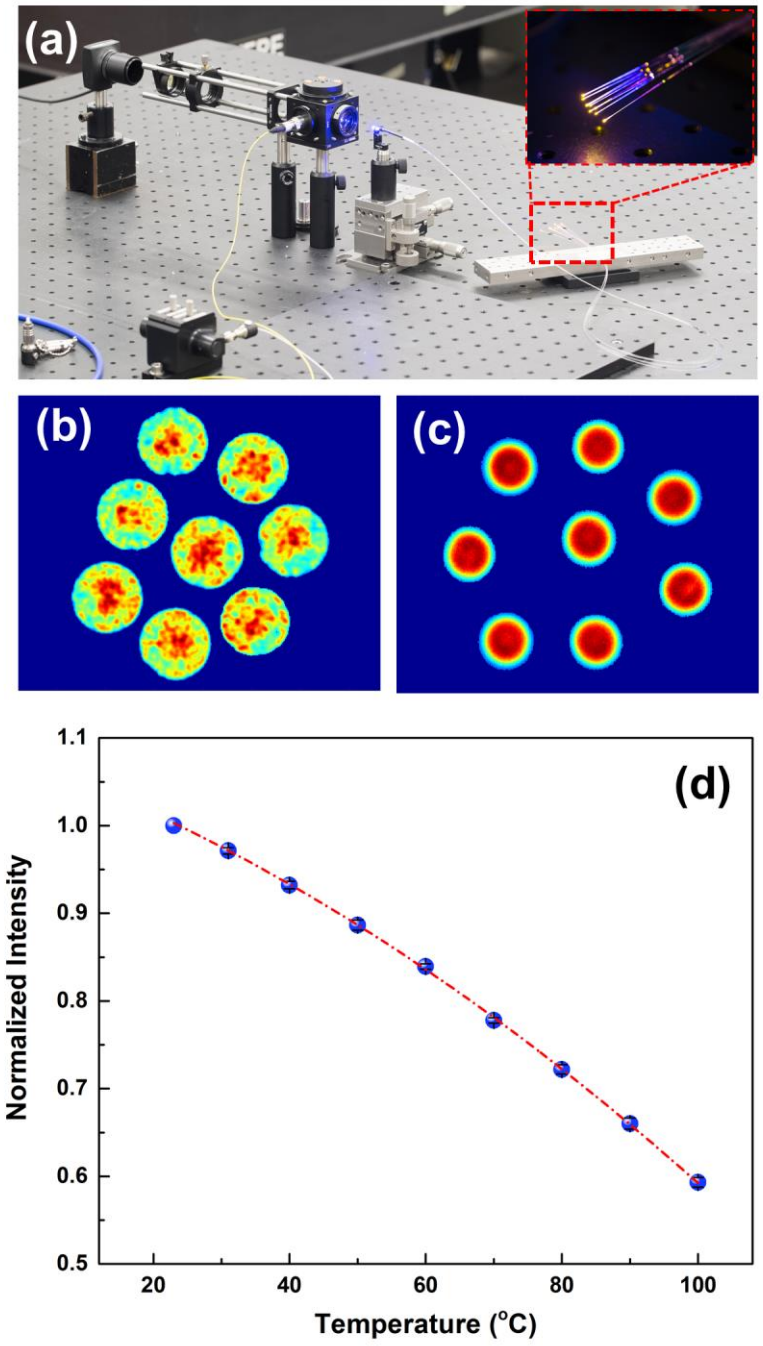

Figure 33. Multi-point fiber optic sensors. (a) Schematic of the multipoint sensor system for temperature monitoring of lithium-ion battery pack; (b) digital image of the sensor bundle with 8 sensors under the optical excitation; (c) normalized digital image of the fiber bundle end face under optical excitation at room temperature; (d) intensity of the emission at different temperatures captured by CCD camera.

Figure 33(b) and (c) shows the digital image of the sensor bundle under the exaction. During the real applications, the individual sensor could be installed in the interested location. Figure 3c shows image of the normalized fluorescence emission from the sensor bundle at room temperature. Using connected area picking algorithm, the fluorescence from each sensor could be clearly recognized and intensity value can be calculated by integration of specific area. Calibration procedure was presented for the sensor bundle by increase the temperature from 23^{o}C to 100^{o}C. Figure 33(d) shows the normalized fluorescence intensity of the sensors with respect to intensity at 23^{o}C. The result shown in figure 3d indicate all the sensors in this bundle have almost identical temperature response. The measured emission intensity here decreased faster when temperature is higher, which is slightly different from the linear relation in figure 32(e). Accompanying with thermal decay of the fluoresce intensity, the emission spectrum also shifted to longer wavelength. And the quantum efficiency of the CCD camera is not constant in that wavelength range. Thus, the normalized intensity is curve-fitted to polynomial line here.

6.3 PARALLEL MONITORING OF LITHIUM-ION BATTERIES

In the past years, lithium-ion batteries have been widely used in both electric vehicles (EV) due to their large energy density and simple functional characteristics [124]. The lithium-ion cells have long been considered as an inherently safer alternative to other lithium metal-anode cells[124]. However, challenges still exist in thermal related safety and performance issues, and hazards associated with lithium-ion cells usually originate from the overheating by electrical abuse (abnormal charging or discharging, short circuit) or mechanical abuse (penetration). When temperature goes above 50^{o}C, the charging efficiency and longevity of the battery will

compromise or even potentially lead to catastrophic fire or explosion [125]. Thus, in-situ monitoring of temperature inside individual lithium ion battery cells in battery assembly holds great promise in improving the safety by allowing earlier detection of overheating [126]. Non-intrusive sensing of the temperature of the battery is desirable for validation of many modeling and simulation works on thermodynamics analysis. Multiple temperature monitoring techniques have been developed to directly measure the temperature of the battery cell assembly, such as compact size thermocouple with junction of 1mm installed in the cell [127], four-probe method for individual battery [128], and polymer embedded thin film thermocouples [126]. However, all of these methods either hard for real-time multipoint sensing, or made of metal material which is not suitable to be installed inside of the battery. Additionally, for internal monitoring, the chemically aggressive and electrically noisy environments are also a critical challenge for these sensors, while sensors based on fibers are quite suitable for its immunity to electromagnetic noise and resilience to corrosive materials.

The sensor probes of multipoint sensing system were subsequently attached to the batteries in a battery packs, in order to investigate the thermal dynamics during the rapid discharging process. For this purpose, a battery pack was built using 8 Li-ion batteries (18650) with capacity of 2600mAh as shown in figure 34(a). Each battery in the pack can be charge and discharge under different current using individual controller. The sensor probes from the fiber bundle were directly taped on the surface of the batteries. The data was streamed to computer for real-time processing and temperature measurement.

In the first test, all the batteries were discharged at 3A at room temperature after fully charged. Heat generation during the discharging of the cell leads to the temperature increase of the cell. The temperature was monitored until all the batteries are fully discharged. Figure 34(b)

shows the fluorescence intensity obtained from different sensors during this process. By using the calibration data in figure 33(d), the temperature evolution characteristics of the battery pack during the discharging process was shown in figure 34(c) according to the fluorescence intensity. The result clearly shows that temperature rapidly increased with highest temperature at 95^{o}C in 51 minutes when the batteries was depleted and the currents were cut off. Different batteries at different locations may has variations in temperature. At the same time, a thermal couple was installed on the top of the battery pack to measure the temperature as a reference. The measurement shows similar temperature characteristics but it's about 20^{o}C lower than the temperature measured at the surface of the battery by the fluorescence sensor probe. Another test was conducted by selectively discharge 3 batteries of the assembly to test the sensor response. In this test, the battery labeled #4, #7 and #8 was discharged 35 minutes with constant current of 3 A. The fluorescence intensity image of the bundle shows that the intensity of the sensor #4, #7 and #8 are darker than other sensors. The system successfully measured the real-time temperature evolution as shown in figure 34(e). We can notice that temperature of the selected batteries for discharging increased fast during this process. Due to the heat conduction, the temperature of other batteries also increased with value corresponding to the distance to the discharged batteries.

In summary, we have demonstrated multipoint fiber optical temperature sensing system by using novel random hole fiber embedded with CdSe/ZnS QDs. Due to the large active optical volume of the random hole fiber, the sensor is highly efficient in temperature measurement. Both the emission peak wavelength and intensity of the QDs sensor depends on the environment temperature. By using single CCD to monitor the emission intensity from multiple fiber sensors, we demonstrated reliable and repeatable temperature measurement of the lithium-ion assembly.

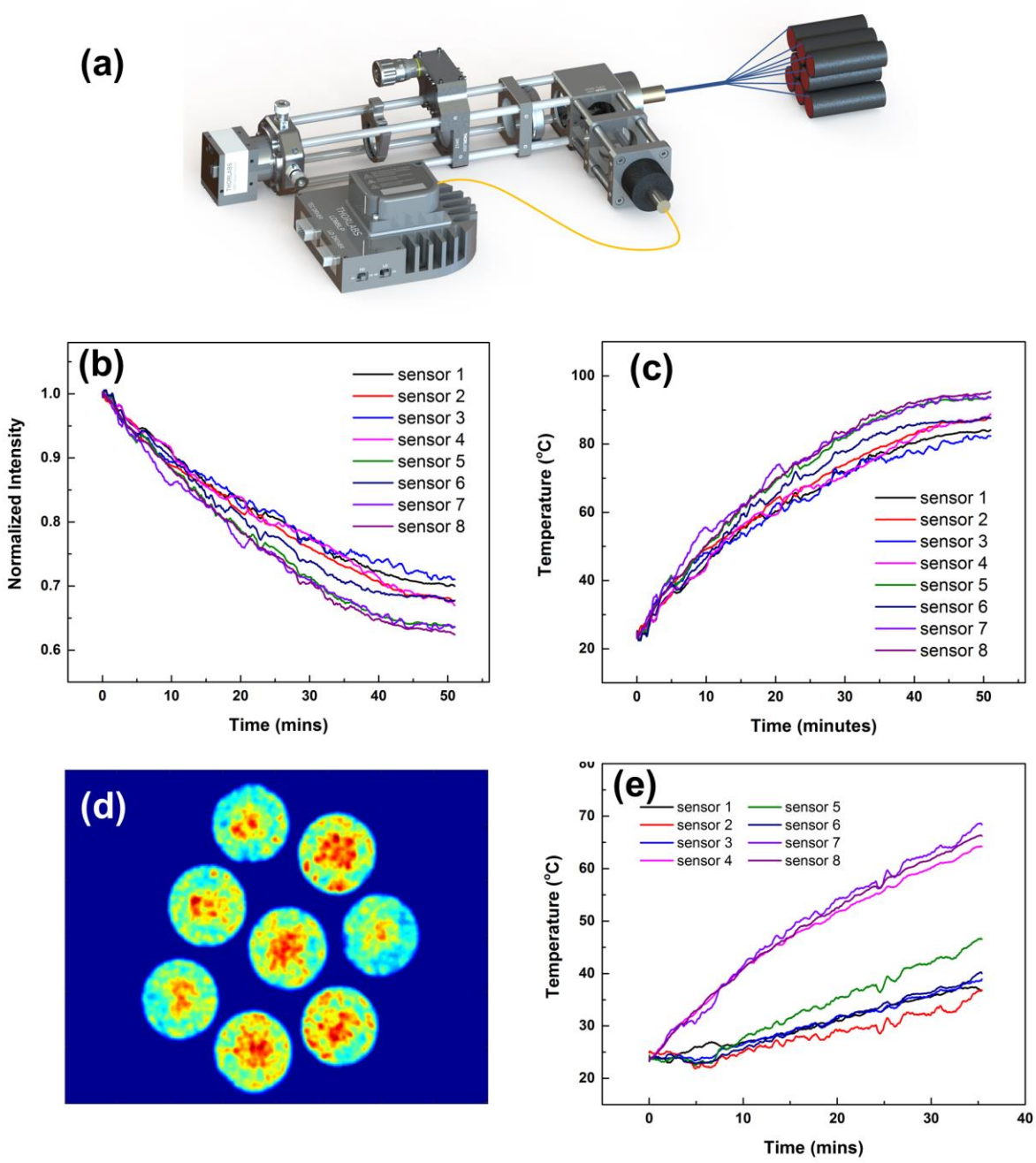

Figure 34. Temperature monitoring of the lithium-ion battery assembly. (a) Schematic of the multi-point sensor for real-time monitoring of lithium-ion batteries; (b) integrated emitted intensity of different sensors and (c) corresponding temperature during the constant discharging process; (d) digital image of the fiber bundle end face for selectively discharging 3 batteries in the assembly and (e) corresponding temperature variation during the whole process

7.0 CONCLUSION AND FUTURE WORK

In conclusion, we have mainly investigated and demonstrated the applications of several fiber optical sensors for real-time accurate monitoring of both chemical and physical parameters in energy industries under harsh environments, where the conventional available sensors exhibit poor reliability. The sensing performance of the developed sensors in this dissertation can allow them either to emphasize a significant improvement in energy efficiency or to reduce the hazard associated with energy industries.

In this chapter 3 and 4, we mainly focused on the development of fiber optic sensors for chemical gas detection at high temperature. A solution-based scalable nanofabrication scheme is proposed to manufacture metal oxides and their doping variants with controlled index of refraction. Through block copolymer templating, metal oxides (including TiO_2, SnO_2, ZnO and SiO_2) with 3D nanostructure were synthesized with refractive index range from 1.2 to 2.4. This new material synthesis technique has been successfully applied for new optical sensor developments. Using solution-based coating technique, Pd-TiO_2 thin film were successfully integrated with high-temperature-stable fiber Bragg grating in D-shaped fiber and single crystal sapphire fiber for evanescent wave sensing for hydrogen at elevated temperatures up to 800^{o}C. The experimental result shows the sensor's hydrogen response is reversible and fast.

In chapter 5, we demonstrated the enhancement of the in-fiber Rayleigh scattering using ultrafast laser irradiation method to improve the distributed sensing for high temperature operation. The in-fiber scatter was improved more than 40 dB due to the formation of periodic

nanogratings. By optimized the writing parameter, the insertion loss of the irradiated fiber was minimized by adjusting the scanning speed. Attributed to the thermal stability of the inscribed nanogratings, revisable temperature measurements were taken from room temperature to 800^{o}C even in ambient hydrogen atmosphere. The developed sensor successfully performed distributed temperature measurements in an operational SOFC.

In chapter 6, we presented a low-cost and compact multipoint fiber optic sensing system to monitoring the thermal dynamics of lithium-ion batteries during operation. Fiber optic temperature sensors were fabricated by infiltrating random air hole fibers with quantum dots, of which luminescence properties are highly dependent on ambient temperature. Comparing to the evanescent field excitation configuration using single mode random hole fiber, the multimode random air hole fibers provide larger optical active region, which significantly improved the sensitivity. A multiplexable sensing system with multiple sensors was used to parallelly monitor the battery assembly during the rapid charging and discharging process.

Based on optical frequency domain reflectometry, preliminary results of chemical gas distributed sensing were presented in chapter 3. Using the optical fiber with enhanced Rayleigh scattering described in chapter 5, the spatial resolution was significantly improved. As a good starting point to take advantage of the enhanced scattering, it's possible to design distributed chemical gas sensors with longer detection range and higher spatial resolution. The detection of chemicals is based on the distributed loss measurement in time domain. At the same time, we could obtain the response in the frequency domain from the fiber under the test at the same time, which means the temperature change can be detection using the same sensor.

BIBLIOGRAPHY

[1] S. Joo, I. Muto, and N. Hara, "Hydrogen Gas Sensor Using Pt- and Pd-Added Anodic TiO_2 Nanotube Films," *Journal of The Electrochemical Society*, vol. 157, no. 6, pp. J221-J226, June 1, 2010 2010.

[2] L. L. Fields, J. P. Zheng, Y. Cheng, and P. Xiong, "Room-temperature low-power hydrogen sensor based on a single tin dioxide nanobelt," *Applied Physics Letters*, vol. 88, no. 26, p. 263102, 2006.

[3] J. Moon, J.-A. Park, S.-J. Lee, T. Zyung, and I.-D. Kim, "Pd-doped TiO_2 nanofiber networks for gas sensor applications," *Sensors and Actuators B: Chemical*, vol. 149, no. 1, pp. 301-305, 8/6/ 2010.

[4] P. R. Ohodnicki, M. Andio, and C. Wang, "Optical gas sensing responses in transparent conducting oxides with large free carrier density," (in English), *Journal of Applied Physics*, vol. 116, no. 2, p. 024309, Jul 14 2014.

[5] P. R. Ohodnicki, S. Natesakhawat, J. P. Baltrus, B. Howard, and T. D. Brown, "Characterization of optical, chemical, and structural changes upon reduction of sol–gel deposited SnO_2 thin films for optical gas sensing at high temperatures," *Thin Solid Films*, vol. 520, no. 19, pp. 6243-6249, 7/31/ 2012.

[6] M. Buric, K. P. Chen, M. Bhattarai, P. R. Swinehart, and M. Maklad, "Active fiber Bragg grating hydrogen sensors for all-temperature operation," (in English), *Ieee Photonics Technology Letters*, vol. 19, no. 5-8, pp. 255-257, Mar-Apr 2007.

[7] X. Bévenot, A. Trouillet, C. Veillas, H. Gagnaire, and M. Clément, "Surface plasmon resonance hydrogen sensor using an optical fibre," *Measurement Science and Technology*, vol. 13, no. 1, p. 118, 2002.

[8] J. Villatoro, D. Luna-Moreno, and D. Monzon-Hernandez, "Optical fiber hydrogen sensor for concentrations below the lower explosive limit," (in English), *Sensors and Actuators B-Chemical*, vol. 110, no. 1, pp. 23-27, Sep 30 2005.

[9] Z. Gu, Y. Xu, and K. Gao, "Optical fiber long-period grating with solgel coating for gas sensor," *Opt. Lett.*, vol. 31, no. 16, pp. 2405-2407, 08/15 2006.

[10] N. Yamazoe, "Toward innovations of gas sensor technology," *Sensors and Actuators B: Chemical,* vol. 108, no. 1–2, pp. 2-14, 7/22/ 2005.

[11] J. B. Pendry, D. Schurig, and D. R. Smith, "Controlling electromagnetic fields," (in English), *Science,* vol. 312, no. 5781, pp. 1780-1782, Jun 23 2006.

[12] Q. Wu, J. P. Turpin, and D. H. Werner, "Integrated photonic systems based on transformation optics enabled gradient index devices," (in English), *Light-Science & Applications,* vol. 1, Nov 2012.

[13] S. Shao, M. Dimitrov, N. Guan, and R. Kohn, "Crystalline nanoporous metal oxide thin films by post-synthetic hydrothermal transformation: SnO_2 and TiO_2," *Nanoscale,* 10.1039/C0NR00079E vol. 2, no. 10, pp. 2054-2057, 2010.

[14] Z. L. Poole, P. Ohodnicki, R. Chen, Y. Lin, and K. P. Chen, "Engineering metal oxide nanostructures for the fiber optic sensor platform," *Optics Express,* vol. 22, no. 3, pp. 2665-2674, 2014/02/10 2014.

[15] A. Rothschild and Y. Komem, "The effect of grain size on the sensitivity of nanocrystalline metal-oxide gas sensors," *Journal of Applied Physics,* vol. 95, no. 11, pp. 6374-6380, 2004.

[16] H. Liu, D. Ding, C. Ning, and Z. Li, "Wide-range hydrogen sensing with Nb-doped TiO_2 nanotubes," *Nanotechnology,* vol. 23, no. 1, p. 015502, 2012.

[17] M. C. Orilall and U. Wiesner, "Block copolymer based composition and morphology control in nanostructured hybrid materials for energy conversion and storage: solar cells, batteries, and fuel cells," *Chemical Society Reviews,* 10.1039/C0CS00034E vol. 40, no. 2, pp. 520-535, 2011.

[18] B. E. Yoldas and D. P. Partlow, "Formation of broad band antireflective coatings on fused silica for high power laser applications," *Thin Solid Films,* vol. 129, no. 1, pp. 1-14, 1985/07/12 1985.

[19] D. Haridas, V. Gupta, and K. Sreenivas, "Enhanced catalytic activity of nanoscale platinum islands loaded onto SnO_2 thin film for sensitive LPG gas sensors," (in English), *Bulletin of Materials Science,* vol. 31, no. 3, pp. 397-400, 2008/06/01 2008.

[20] C. Wang, L. Yin, L. Zhang, D. Xiang, and R. Gao, "Metal Oxide Gas Sensors: Sensitivity and Influencing Factors," *Sensors,* vol. 10, no. 3, p. 2088, 2010.

[21] Y.-L. Liu *et al.*, "Hydrogen sulfide sensing properties of $NiFe_2O_4$ nanopowder doped with noble metals," *Sensors and Actuators B: Chemical,* vol. 102, no. 1, pp. 148-154, 9/1/ 2004.

[22] M. Penza *et al.*, "Enhancement of sensitivity in gas chemiresistors based on carbon nanotube surface functionalized with noble metal (Au, Pt) nanoclusters," *Applied Physics Letters,* vol. 90, no. 17, p. 173123, 2007.

[23] P. R. Ohodnicki, C. J. Wang, S. Natesakhawat, J. P. Baltrus, and T. D. Brown, "In-situ and ex-situ characterization of TiO_2 and Au nanoparticle incorporated TiO2 thin films for optical gas sensing at extreme temperatures," (in English), *Journal of Applied Physics,* vol. 111, no. 6, p. 064320, Mar 15 2012.

[24] P. R. Ohodnicki Jr, T. D. Brown, G. R. Holcomb, J. Tylczak, A. M. Schultz, and J. P. Baltrus, "High temperature optical sensing of gas and temperature using Au-nanoparticle incorporated oxides," *Sensors and Actuators B: Chemical,* vol. 202, no. 0, pp. 489-499, 10/31/ 2014.

[25] Y. Shen *et al.*, "Microstructure and H2 gas sensing properties of undoped and Pd-doped SnO_2 nanowires," *Sensors and Actuators B: Chemical,* vol. 135, no. 2, pp. 524-529, 1/15/ 2009.

[26] P. R. Ohodnicki, Jr. *et al.*, "Plasmonic nanocomposite thin film enabled fiber optic sensors for simultaneous gas and temperature sensing at extreme temperatures," *Nanoscale,* 10.1039/C3NR02891G vol. 5, no. 19, pp. 9030-9, Oct 7 2013.

[27] P. Wang, G. Brambilla, M. Ding, Y. Semenova, Q. Wu, and G. Farrell, "High-sensitivity, evanescent field refractometric sensor based on a tapered, multimode fiber interference," *Optics Letters,* vol. 36, no. 12, pp. 2233-2235, 2011/06/15 2011.

[28] A. Armin, M. Soltanolkotabi, and P. Feizollah, "On the pH and concentration response of an evanescent field absorption sensor using a coiled-shape plastic optical fiber," *Sensors and Actuators A: Physical,* vol. 165, no. 2, pp. 181-184, 2// 2011.

[29] L. Zhang, F. Gu, J. Lou, X. Yin, and L. Tong, "Fast detection of humidity with a subwavelength-diameter fiber taper coated with gelatin film," *Optics Express,* vol. 16, no. 17, pp. 13349-13353, 2008/08/18 2008.

[30] A. M. Schultz, T. D. Brown, M. P. Buric, S. Lee, K. Gerdes, and P. R. Ohodnicki, "High temperature fiber-optic evanescent wave hydrogen sensors using La-doped $SrTiO_3$ for SOFC applications," *Sensors and Actuators B: Chemical,* vol. 221, pp. 1307-1313, 12/31/ 2015.

[31] S. Korposh, H. Okuda, T. Wang, S. W. James, and S. W. Lee, "U-shaped evanescent wave optical fibre sensor based on a porphyrin anchored nanoassembled thin film for high sensitivity ammonia detection," 2015, vol. 9655, pp. 965518-965518-4.

[32] F. B. Xiong, W. Z. Zhu, H. F. Lin, and X. G. Meng, "Fiber-optic sensor based on evanescent wave absorbance around 2.7 μm for determining water content in polar

organic solvents," (in English), *Applied Physics B,* vol. 115, no. 1, pp. 129-135, 2014/04/01 2014.

[33] A. Valadez, C. Lana, S.-I. Tu, M. Morgan, and A. Bhunia, "Evanescent Wave Fiber Optic Biosensor for Salmonella Detection in Food," *Sensors,* vol. 9, no. 7, p. 5810, 2009.

[34] N. Zhong, Q. Liao, X. Zhu, M. Zhao, Y. Huang, and R. Chen, "Temperature-independent polymer optical fiber evanescent wave sensor," *Scientific Reports,* Article vol. 5, p. 11508, 06/26/online 2015.

[35] S. Avino *et al.*, "High-sensitivity ring-down evanescent-wave sensing in fiber resonators," *Optics Letters,* vol. 39, no. 19, pp. 5725-5728, 2014/10/01 2014.

[36] H. Chen, F. Tian, J. Kanka, and H. Du, "A scalable pathway to nanostructured sapphire optical fiber for evanescent-field sensing and beyond," (in English), *Applied Physics Letters,* vol. 106, no. 11, p. 111102, Mar 16 2015.

[37] V. Ruddy, B. D. MacCraith, and J. A. Murphy, "Evanescent wave absorption spectroscopy using multimode fibers," *Journal of Applied Physics,* vol. 67, no. 10, pp. 6070-6074, 1990.

[38] E. Sinchenko, W. E. K. Gibbs, A. P. Mazzolini, and P. R. Stoddart, "The Effect of the Cladding Refractive Index on an Optical Fiber Evanescent-Wave Sensor," *Journal of Lightwave Technology,* vol. 31, no. 20, pp. 3251-3257, 2013/10/15 2013.

[39] A. Othonos, "Fiber bragg gratings," *Review of scientific instruments,* vol. 68, no. 12, pp. 4309-4341, 1997.

[40] Y. Sano and T. Yoshino, "Fast optical wavelength interrogator employing arrayed waveguide grating for distributed fiber Bragg grating sensors," *Journal of Lightwave Technology,* vol. 21, no. 1, pp. 132-139, 2003.

[41] X. Wang *et al.*, "An OTDR and Gratings Assisted Multifunctional Fiber Sensing System," *IEEE Sensors Journal,* vol. 15, no. 8, pp. 4660-4666, 2015.

[42] M. Froggatt and J. Moore, "Distributed measurement of static strain in an optical fiber with multiple Bragg gratings at nominally equal wavelengths," *Applied Optics,* vol. 37, no. 10, pp. 1741-1746, 1998/04/01 1998.

[43] X. Bao and L. Chen, "Recent progress in distributed fiber optic sensors," *Sensors,* vol. 12, no. 7, pp. 8601-8639, 2012.

[44] X. Bao and L. Chen, "Recent progress in Brillouin scattering based fiber sensors," *Sensors,* vol. 11, no. 4, pp. 4152-4187, 2011.

[45] T. Horiguchi and M. Tateda, "Optical-fiber-attenuation investigation using stimulated Brillouin scattering between a pulse and a continuous wave," *Optics Letters,* vol. 14, no. 8, pp. 408-410, 1989/04/15 1989.

[46] T. Horiguchi, T. Kurashima, and Y. Koyamada, "Measurement of temperature and strain distribution by Brillouin frequency shift in silica optical fibers," 1993, vol. 1797, pp. 2-13.

[47] B. J. Soller, D. K. Gifford, M. S. Wolfe, and M. E. Froggatt, "High resolution optical frequency domain reflectometry for characterization of components and assemblies," *Optics Express,* vol. 13, no. 2, pp. 666-674, 2005/01/24 2005.

[48] A. K. Sang, M. E. Froggatt, D. K. Gifford, S. T. Kreger, and B. D. Dickerson, "One Centimeter Spatial Resolution Temperature Measurements in a Nuclear Reactor Using Rayleigh Scatter in Optical Fiber," *IEEE Sensors Journal,* vol. 8, no. 7, pp. 1375-1380, 2008.

[49] S. T. Kreger, D. K. Gifford, M. E. Froggatt, B. J. Soller, and M. S. Wolfe, "High Resolution Distributed Strain or Temperature Measurements in Single- and Multi-Mode Fiber Using Swept-Wavelength Interferometry," in *Optical Fiber Sensors*, Cancun, 2006, p. ThE42: Optical Society of America.

[50] R. J. M. Robert, N. M. William, S. B. James, M. Scott, and J. S. J. Benjamin, "Distributed sensing using Rayleigh scatter in polarization-maintaining fibres for transverse load sensing," *Measurement Science and Technology,* vol. 21, no. 9, p. 094019, 2010.

[51] D. K. Gifford *et al.*, "Swept-wavelength interferometric interrogation of fiber Rayleigh scatter for distributed sensing applications," 2007, vol. 6770, pp. 67700F-67700F-9.

[52] M. Froggatt and J. Moore, "High-spatial-resolution distributed strain measurement in optical fiber with Rayleigh scatter," *Applied Optics,* vol. 37, no. 10, pp. 1735-1740, 1998/04/01 1998.

[53] S. Loranger, M. Gagné, V. Lambin-Iezzi, and R. Kashyap, "Rayleigh scatter based order of magnitude increase in distributed temperature and strain sensing by simple UV exposure of optical fibre," *Scientific Reports,* Article vol. 5, p. 11177, 06/16/online 2015.

[54] K. O. Hill, Y. Fujii, D. C. Johnson, and B. S. Kawasaki, "Photosensitivity in optical fiber waveguides: Application to reflection filter fabrication," *Applied Physics Letters,* vol. 32, no. 10, pp. 647-649, 1978.

[55] K. M. Davis, K. Miura, N. Sugimoto, and K. Hirao, "Writing waveguides in glass with a femtosecond laser," *Optics Letters,* vol. 21, no. 21, pp. 1729-1731, 1996/11/01 1996.

[56] D. Homoelle, S. Wielandy, A. L. Gaeta, N. F. Borrelli, and C. Smith, "Infrared photosensitivity in silica glasses exposed to femtosecond laser pulses," *Optics Letters,* vol. 24, no. 18, pp. 1311-1313, 1999/09/15 1999.

[57] W.-J. Chen, S. M. Eaton, H. Zhang, and P. R. Herman, "Broadband directional couplers fabricated in bulk glass with high repetition rate femtosecond laser pulses," *Optics Express,* vol. 16, no. 15, pp. 11470-11480, 2008/07/21 2008.

[58] N. Takeshima, Y. Narita, S. Tanaka, Y. Kuroiwa, and K. Hirao, "Fabrication of high-efficiency diffraction gratings in glass," *Optics Letters,* vol. 30, no. 4, pp. 352-354, 2005/02/15 2005.

[59] E. N. Glezer and E. Mazur, "Ultrafast-laser driven micro-explosions in transparent materials," *Applied Physics Letters,* vol. 71, no. 7, pp. 882-884, 1997.

[60] R. Taylor, C. Hnatovsky, and E. Simova, "Applications of femtosecond laser induced self‐organized planar nanocracks inside fused silica glass," *Laser & Photonics Reviews,* vol. 2, no. 1‐2, pp. 26-46, 2008.

[61] M. Ams *et al.*, "Investigation of Ultrafast Laser--Photonic Material Interactions: Challenges for Directly Written Glass Photonics," *IEEE Journal of Selected Topics in Quantum Electronics,* vol. 14, no. 5, pp. 1370-1381, 2008.

[62] C. Hnatovsky *et al.*, "Pulse duration dependence of femtosecond-laser-fabricated nanogratings in fused silica," *Applied Physics Letters,* vol. 87, no. 1, p. 014104, 2005.

[63] Y. Liao *et al.*, "Direct laser writing of sub-50 nm nanofluidic channels buried in glass for three-dimensional micro-nanofluidic integration," *Lab on a Chip,* vol. 13, no. 8, pp. 1626-1631, 2013.

[64] C. Hnatovsky *et al.*, "Fabrication of microchannels in glass using focused femtosecond laser radiation and selective chemical etching," *Applied Physics A,* vol. 84, no. 1-2, pp. 47-61, 2006.

[65] Y. Shimotsuma, P. G. Kazansky, J. Qiu, and K. Hirao, "Self-Organized Nanogratings in Glass Irradiated by Ultrashort Light Pulses," *Physical Review Letters,* vol. 91, no. 24, p. 247405, 12/11/ 2003.

[66] P. Rajeev *et al.*, "Memory in nonlinear ionization of transparent solids," *Physical review letters,* vol. 97, no. 25, p. 253001, 2006.

[67] Y. Liao *et al.*, "Formation of in-volume nanogratings with sub-100-nm periods in glass by femtosecond laser irradiation," *Optics Letters,* vol. 40, no. 15, pp. 3623-3626, 2015/08/01 2015.

[68] A. Rudenko, J.-P. Colombier, and T. E. Itina, "From random inhomogeneities to periodic nanostructures induced in bulk silica by ultrashort laser," *Physical Review B,* vol. 93, no. 7, p. 075427, 2016.

[69] M. Zhang, Z. Yuan, J. Song, and C. Zheng, "Improvement and mechanism for the fast response of a Pt/TiO2 gas sensor," *Sensors and Actuators B: Chemical,* vol. 148, no. 1, pp. 87-92, 6/30/ 2010.

[70] A. Kolmakov and M. Moskovits, "CHEMICAL SENSING AND CATALYSIS BY ONE-DIMENSIONAL METAL-OXIDE NANOSTRUCTURES," *Annual Review of Materials Research,* vol. 34, no. 1, pp. 151-180, 2004.

[71] H. T. Wang *et al.*, "Hydrogen-selective sensing at room temperature with ZnO nanorods," *Applied Physics Letters,* vol. 86, no. 24, p. 243503, 2005.

[72] I.-D. Kim, A. Rothschild, B. H. Lee, D. Y. Kim, S. M. Jo, and H. L. Tuller, "Ultrasensitive Chemiresistors Based on Electrospun TiO2 Nanofibers," *Nano Letters,* vol. 6, no. 9, pp. 2009-2013, 2006/09/01 2006.

[73] A. S. Zuruzi, A. Kolmakov, N. C. MacDonald, and M. Moskovits, "Highly sensitive gas sensor based on integrated titania nanosponge arrays," *Applied Physics Letters,* vol. 88, no. 10, p. 102904, 2006.

[74] K. S. Park *et al.*, "Compact and multiplexible hydrogen gas sensor assisted by self-referencing technique," *Optics Express,* vol. 19, no. 19, pp. 18190-18198, 2011/09/12 2011.

[75] T. Chen *et al.*, "Distributed hydrogen sensing using in-fiber Rayleigh scattering," *Applied Physics Letters,* vol. 100, no. 19, p. 191105, 2012.

[76] D. Haridas and V. Gupta, "Enhanced response characteristics of SnO_2 thin film based sensors loaded with Pd clusters for methane detection," *Sensors and Actuators B: Chemical,* vol. 166–167, pp. 156-164, 5/20/ 2012.

[77] P. Bhattacharyya, P. K. Basu, C. Lang, H. Saha, and S. Basu, "Noble metal catalytic contacts to sol–gel nanocrystalline zinc oxide thin films for sensing methane," *Sensors and Actuators B: Chemical,* vol. 129, no. 2, pp. 551-557, 2/22/ 2008.

[78] F. Quaranta *et al.*, "A novel gas sensor based on SnO_2/Os thin film for the detection of methane at low temperature," *Sensors and Actuators B: Chemical,* vol. 58, no. 1–3, pp. 350-355, 9/21/ 1999.

[79] X. Hai, D. Jiangdong, G. Pickrell, R. G. May, and W. Anbo, "Single-crystal sapphire fiber-based strain sensor for high-temperature applications," *Journal of Lightwave Technology,* vol. 21, no. 10, pp. 2276-2283, 2003.

[80] T. Elsmann, T. Habisreuther, A. Graf, M. Rothhardt, and H. Bartelt, "Inscription of first-order sapphire Bragg gratings using 400 nm femtosecond laser radiation," *Opt Express,* vol. 21, no. 4, pp. 4591-7, Feb 25 2013.

[81] Z. L. Poole *et al.*, "Block copolymer assisted refractive index engineering of metal oxides for applications in optical sensing," in *Proc. SPIE 9161, Nanophotonic Materials XI,* 2014, vol. 9161, p. 91610P.

[82] A. Baylet, P. Marecot, D. Duprez, P. Castellazzi, G. Groppi, and P. Forzatti, "In situ Raman and in situ XRD analysis of PdO reduction and Pd degrees oxidation supported on gamma-Al_2O_3 catalyst under different atmospheres," *Phys Chem Chem Phys,* 10.1039/C0CP01331E vol. 13, no. 10, pp. 4607-13, Mar 14 2011.

[83] R. M. Walton, D. J. Dwyer, J. W. Schwank, and J. L. Gland, "Gas sensing based on surface oxidation/reduction of platinum-titania thin films II. The role of chemisorbed oxygen in film sensitization," *Applied Surface Science,* vol. 125, no. 2, pp. 199-207, 2// 1998.

[84] D. J. Won, C. H. Wang, H. K. Jang, and D. J. Choi, "Effects of thermally induced anatase-to-rutile phase transition in MOCVD-grown TiO_2 films on structural and optical properties," (in English), *Applied Physics a-Materials Science & Processing,* vol. 73, no. 5, pp. 595-600, Nov 2001.

[85] C. Perrotton *et al.*, "A reliable, sensitive and fast optical fiber hydrogen sensor based on surface plasmon resonance," *Opt Express,* vol. 21, no. 1, pp. 382-90, Jan 14 2013.

[86] Q. Yan, S. Tao, and H. Toghiani, "Optical fiber evanescent wave absorption spectrometry of nanocrystalline tin oxide thin films for selective hydrogen sensing in high temperature gas samples," *Talanta,* vol. 77, no. 3, pp. 953-961, 1/15/ 2009.

[87] W. Eickhoff and R. Ulrich, "Optical frequency domain reflectometry in single‐mode fiber," *Applied Physics Letters,* vol. 39, no. 9, pp. 693-695, 1981.

[88] M. E. Froggatt, D. K. Gifford, S. T. Kreger, M. S. Wolfe, and B. J. Soller, "Distributed Strain and Temperature Discrimination in Unaltered Polarization Maintaining Fiber," in *Optical Fiber Sensors*, Cancun, 2006, p. ThC5: Optical Society of America.

[89] J. Jin, H. Zhang, J. Liu, and Y. Li, "Distributed Temperature Sensing Based on Rayleigh Scattering in Irradiated Optical Fiber," *IEEE Sensors Journal,* vol. 16, no. 24, pp. 8928-8935, 2016.

[90] S. T. Kreger, A. K. Sang, D. K. Gifford, and M. E. Froggatt, "Distributed strain and temperature sensing in plastic optical fiber using Rayleigh scatter," *Proceedings of SPIE - The International Society for Optical Engineering,* vol. 7316, no. 5, pp. 73160A-73160A-8, 2009.

[91] M. Buric, P. Ohodnicki, A. Yan, S. Huang, and K. P. Chen, "Distributed fiber-optic sensing in a high-temperature solid-oxide fuel cell," in *SPIE Optical Engineering + Applications*, 2016, vol. 9977, p. 997708.

[92] C. W. Smelser, S. J. Mihailov, and D. Grobnic, "Formation of Type I-IR and Type II-IR gratings with an ultrafast IR laser and a phase mask," *Optics Express,* vol. 13, no. 14, pp. 5377-5386, 2005/07/11 2005.

[93] Y. Xu *et al.*, "Optical fiber random grating-based multiparameter sensor," *Optics Letters,* vol. 40, no. 23, pp. 5514-5517, 2015/12/01 2015.

[94] E. Bricchi and P. G. Kazansky, "Extraordinary stability of anisotropic femtosecond direct-written structures embedded in silica glass," *Applied physics letters,* vol. 88, no. 11, p. 111119, 2006.

[95] S. Richter, M. Heinrich, S. Döring, A. Tünnermann, S. Nolte, and U. Peschel, "Nanogratings in fused silica: Formation, control, and applications," *Journal of Laser Applications,* vol. 24, no. 4, p. 042008, 2012.

[96] J. Zhang, M. Gecevičius, M. Beresna, and P. G. Kazansky, "Seemingly Unlimited Lifetime Data Storage in Nanostructured Glass," *Physical Review Letters,* vol. 112, no. 3, p. 033901, 01/23/ 2014.

[97] F. Liang, R. Vallée, and S. L. Chin, "Mechanism of nanograting formation on the surface of fused silica," *Optics Express,* vol. 20, no. 4, pp. 4389-4396, 2012/02/13 2012.

[98] M. Beresna, M. Gecevičius, P. G. Kazansky, T. Taylor, and A. V. Kavokin, "Exciton mediated self-organization in glass driven by ultrashort light pulses," *Applied Physics Letters,* vol. 101, no. 5, p. 053120, 2012.

[99] Y. Liao *et al.*, "High-fidelity visualization of formation of volume nanogratings in porous glass by femtosecond laser irradiation," *Optica,* vol. 2, no. 4, pp. 329-334, 2015/04/20 2015.

[100] C. Hnatovsky, D. Grobnic, D. Coulas, M. Barnes, and S. J. Mihailov, "Self-organized nanostructure formation during femtosecond-laser inscription of fiber Bragg gratings," *Optics Letters,* vol. 42, no. 3, pp. 399-402, 2017/02/01 2017.

[101] Y. Dai, A. Patel, J. Song, M. Beresna, and P. G. Kazansky, "Void-nanograting transition by ultrashort laser pulse irradiation in silica glass," *Optics Express,* vol. 24, no. 17, pp. 19344-19353, 2016/08/22 2016.

[102] P. G. Kazansky *et al.*, "Anomalous Anisotropic Light Scattering in Ge-Doped Silica Glass," *Physical Review Letters,* vol. 82, no. 10, pp. 2199-2202, 03/08/ 1999.

[103] M. Beresna and P. G. Kazansky, "Polarization diffraction grating produced by femtosecond laser nanostructuring in glass," *Optics Letters,* vol. 35, no. 10, pp. 1662-1664, 2010/05/15 2010.

[104] M. E. Froggatt, D. K. Gifford, S. Kreger, M. Wolfe, and B. J. Soller, "Characterization of Polarization-Maintaining Fiber Using High-Sensitivity Optical-Frequency-Domain Reflectometry," *Journal of Lightwave Technology,* vol. 24, no. 11, pp. 4149-4154, 2006/11/01 2006.

[105] P. Lu, D. Grobnic, and S. J. Mihailov, "Characterization of the birefringence in fiber Bragg gratings fabricated with an ultrafast-infrared laser," *Journal of lightwave technology,* vol. 25, no. 3, pp. 779-786, 2007.

[106] V. Boffa, D. H. A. Blank, and J. E. ten Elshof, "Hydrothermal stability of microporous silica and niobia–silica membranes," *Journal of Membrane Science,* vol. 319, no. 1–2, pp. 256-263, 7/1/ 2008.

[107] T. Wang, L.-Y. Shao, J. Canning, and K. Cook, "Temperature and strain characterization of regenerated gratings," *Optics Letters,* vol. 38, no. 3, pp. 247-249, 2013/02/01 2013.

[108] H. Yokokawa, H. Tu, B. Iwanschitz, and A. Mai, "Fundamental mechanisms limiting solid oxide fuel cell durability," *Journal of Power Sources,* vol. 182, no. 2, pp. 400-412, 8/1/ 2008.

[109] C. M. Dikwal, W. Bujalski, and K. Kendall, "The effect of temperature gradients on thermal cycling and isothermal ageing of micro-tubular solid oxide fuel cells," *Journal of Power Sources,* vol. 193, no. 1, pp. 241-248, 8/1/ 2009.

[110] O. Razbani, I. Wærnhus, and M. Assadi, "Experimental investigation of temperature distribution over a planar solid oxide fuel cell," *Applied energy,* vol. 105, pp. 155-160, 2013.

[111] Ö. Aydın, H. Nakajima, and T. Kitahara, "Reliability of the numerical SOFC models for estimating the spatial current and temperature variations," *International Journal of Hydrogen Energy,* vol. 41, no. 34, pp. 15311-15324, 9/14/ 2016.

[112] S. Bedogni, S. Campanari, P. Iora, L. Montelatici, and P. Silva, "Experimental analysis and modeling for a circular-planar type IT-SOFC," *Journal of Power Sources,* vol. 171, no. 2, pp. 617-625, 2007.

[113] V. Biju, Y. Makita, A. Sonoda, H. Yokoyama, Y. Baba, and M. Ishikawa, "Temperature-Sensitive Photoluminescence of CdSe Quantum Dot Clusters," *The Journal of Physical Chemistry B,* vol. 109, no. 29, pp. 13899-13905, 2005/07/01 2005.

[114] D. Valerini, A. Cretí, M. Lomascolo, L. Manna, R. Cingolani, and M. Anni, "Temperature dependence of the photoluminescence properties of colloidal CdSe/ZnS

core/shell quantum dots embedded in a polystyrene matrix," *Physical Review B,* vol. 71, no. 23, p. 235409, 06/13/ 2005.

[115] L. M. Maestro *et al.*, "CdSe quantum dots for two-photon fluorescence thermal imaging," *Nano letters,* vol. 10, no. 12, pp. 5109-5115, 2010.

[116] D. Pugh-Thomas, B. M. Walsh, and M. C. Gupta, "CdSe (ZnS) nanocomposite luminescent high temperature sensor," *Nanotechnology,* vol. 22, no. 18, p. 185503, 2011.

[117] G. de Bastida, F. J. Arregui, J. Goicoechea, and I. R. Matias, "Quantum dots-based optical fiber temperature sensors fabricated by layer-by-layer," *IEEE Sensors Journal,* vol. 6, no. 6, pp. 1378-1379, 2006.

[118] J. Bravo, J. Goicoechea, J. M. Corres, F. J. Arregui, and I. R. Matias, "Encapsulated quantum dot nanofilms inside hollow core optical fibers for temperature measurement," *IEEE Sensors Journal,* vol. 8, no. 7, pp. 1368-1374, 2008.

[119] B. Larrión, M. Hernáez, F. J. Arregui, J. Goicoechea, J. Bravo, and I. R. Matías, "Photonic crystal fiber temperature sensor based on quantum dot nanocoatings," *Journal of Sensors,* vol. 2009, 2009.

[120] H. C. Y. Yu, S. G. Leon-Saval, A. Argyros, and G. W. Barton, "Temperature effects on emission of quantum dots embedded in polymethylmethacrylate," *Applied Optics,* vol. 49, no. 15, pp. 2749-2752, 2010/05/20 2010.

[121] Y. Zhao, C. Riemersma, F. Pietra, R. Koole, C. de Mello Donegá, and A. Meijerink, "High-Temperature Luminescence Quenching of Colloidal Quantum Dots," *ACS Nano,* vol. 6, no. 10, pp. 9058-9067, 2012/10/23 2012.

[122] G. W. Walker, V. C. Sundar, C. M. Rudzinski, A. W. Wun, M. G. Bawendi, and D. G. Nocera, "Quantum-dot optical temperature probes," *Applied Physics Letters,* vol. 83, no. 17, pp. 3555-3557, 2003.

[123] P. Jorge, M. Mayeh, R. Benrashid, P. Caldas, J. Santos, and F. Farahi, "Quantum dots as self-referenced optical fibre temperature probes for luminescent chemical sensors," *Measurement Science and Technology,* vol. 17, no. 5, p. 1032, 2006.

[124] D. Lisbona and T. Snee, "A review of hazards associated with primary lithium and lithium-ion batteries," *Process Safety and Environmental Protection,* vol. 89, no. 6, pp. 434-442, 11// 2011.

[125] N. Sato, "Thermal behavior analysis of lithium-ion batteries for electric and hybrid vehicles," *Journal of power sources,* vol. 99, no. 1, pp. 70-77, 2001.

[126] M. S. K. Mutyala, J. Zhao, J. Li, H. Pan, C. Yuan, and X. Li, "In-situ temperature measurement in lithium ion battery by transferable flexible thin film thermocouples," *Journal of Power Sources,* vol. 260, pp. 43-49, 2014.

[127] C. Forgez, D. Vinh Do, G. Friedrich, M. Morcrette, and C. Delacourt, "Thermal modeling of a cylindrical LiFePO4/graphite lithium-ion battery," *Journal of Power Sources,* vol. 195, no. 9, pp. 2961-2968, 5/1/ 2010.

[128] R. Srinivasan, B. G. Carkhuff, M. H. Butler, and A. C. Baisden, "Instantaneous measurement of the internal temperature in lithium-ion rechargeable cells," *Electrochimica Acta,* vol. 56, no. 17, pp. 6198-6204, 2011/07/01/ 2011.